

9-22-2008

Surface Assembly and Intracellular Delivery of Biomolecule Conjugated Nanomaterials

Joshua M. Kogot
Florida State University

Follow this and additional works at: <http://diginole.lib.fsu.edu/etd>

Recommended Citation

Kogot, Joshua M., "Surface Assembly and Intracellular Delivery of Biomolecule Conjugated Nanomaterials" (2008). *Electronic Theses, Treatises and Dissertations*. Paper 2850.

This Dissertation - Open Access is brought to you for free and open access by the The Graduate School at DigiNole Commons. It has been accepted for inclusion in Electronic Theses, Treatises and Dissertations by an authorized administrator of DigiNole Commons. For more information, please contact lib-ir@fsu.edu.

FLORIDA STATE UNIVERSITY
COLLEGE OF ARTS AND SCIENCES

SURFACE ASSEMBLY AND INTRACELLULAR DELIVERY OF BIOMOLECULE
CONJUGATED NANOMATERIALS

By

JOSHUA MICHAEL KOGOT

A Dissertation submitted to the
Department of Chemistry and Biochemistry
in partial fulfillment of the
requirements for the degree of
Doctor of Philosophy

Degree Awarded:
Fall Semester, 2008

The members of the Committee approve the Dissertation of Joshua Michael Kogot defended on September 22, 2008.

Geoffrey Strouse
Professor Directing Dissertation

P. Bryant Chase
Outside Committee Member

Timothy Logan
Committee Member

Gregory Dudley
Committee Member

Brian Miller
Committee Member

The office of Graduate Studies has verified and approved the above named committee members.

ACKNOWLEDGEMENTS

First and foremost I would like to thank my advisor Geoff Strouse and my unofficial co-advisor Tim Logan for all the time and effort they have committed to make me the scientist I am today. I have learned so much from both of them, and I feel very fortunate to be directed by advisors from two different research fields and two unique teaching styles. Dr. Strouse has always made me try to do better and be better at what I do, never settling for less than what he knew I was capable of doing. Dr. Logan always made me think about the details and has really pushed me to stick to the facts and be critical of my own work above all else. I was lucky to have spent many hours with both of them sifting through data, developing the next great research project, and learning the right way to approach science. I thank them for everything, and I hope I was able to teach them something new along the way.

I would like to thank my committee members, Professors' Chase, Dudley, Logan, Miller and Strouse, for their time to review my dissertation and presence at my dissertation defense.

I would like to acknowledge all of my past and present colleagues (there are many of you) in the Strouse and Logan research groups for all of their help. I could not have done it without your help and enjoyed all of the interactions, discussions, and laughs along the way.

I would like to acknowledge Prof. Sam Grant and Jens Rosenberg for all their useful discussions, new ideas, and all of the lunch meetings to nail down our MR data. I would like to acknowledge Dr. Joan Hare for her help with CHO cell culturing and helping me to better understand cell biology a little. I would like to acknowledge Dr. Claudius Mundoma for his all of his time helping to train me and answer my instrument questions on all of the biophysical instruments in the PBF. I would like to acknowledge Margaret Seavy for always being willing to help me with my HPLC instrument and chromatogram interpretation questions.

TABLE OF CONTENTS

List of Tables.....	vi
List of Figures.....	vii
Abstract.....	x
1. INTRODUCTION.....	1
2. HIS ₆ PEPTIDE ATTACHMENT TO A 1.5 nm Au NANOPARTICLE SURFACE.....	8
2.1 Introduction.....	8
2.2 Methods and Results.....	9
2.3 Discussion and Model.....	20
3. MAINTAINING STRUCTURE AND FUNCTION OF A HISTIDINE-TAGGED PROTEIN ATTACHED TO A 1.5 nm Au NANOPARTICLE.....	23
3.1 Introduction.....	23
3.2 Materials and Methods.....	25
3.3 Results.....	28
3.4 Conclusions.....	38
4. DEVELOPMENT OF A BIMODAL MRI CONTRAST AGENT.....	41
4.1 Introduction.....	41
4.2 Materials and Methods.....	46
4.3 Results.....	50
4.4 Conclusions.....	55
4.5 Future Work.....	56
5. NANOMEDIATED DELIVERY OF DUAL GENE REGULATORS.....	57
5.1 Introduction.....	57
5.2 Materials and Methods.....	59

5.3 Results.....	61
5.4 Discussion.....	71
REFERENCES.....	72
BIOGRAPHICAL SKETCH.....	87

LIST OF TABLES

2.1	FT-IR peak assignments of His ₆ -peptide and His ₆ peptide with AuNP.....	14
2.2	FT-IR peak assignments of Cys-peptide and Cys-peptide with AuNP.....	16
2.3	FT-IR peak assignments of Ser-peptide and Ser-peptide with AuNP.....	17
3.1	FITC fluorescence recovery rates with FGF1 and FGF1-heparin.....	29
4.1	T1 and T2 relaxation rates for InP/ZnS-CAAKA-DOTA-Dy(III) cell layer experiments in agarose tissue mimic.....	52
4.2	T1, T2, T2 linked, and T2 star results for InP/ZnS-CAAKA-DOTA-Dy(III) cell dosing experiments	53
4.3	T1 and T2 relaxation rates for InP/ZnS-CAAKATat-DOTA-Dy(III) with and without cationic liposome transfecting agent.....	55

LIST OF FIGURES

1.1	Crystallographic model of 12 base pair duplex DNA and DsRed fluorescent protein.....	3
1.2	Microscope image of CHO cells and TEM of 1.5 nm AuNP.....	4
2.1	Fluorescence intensity plot of Au nanoparticle bound Cys, Ser, His ₆ peptides with measured in various guanidinium hydrochloride concentrations.....	11
2.2	Absorption spectra of Cys, Ser, and His ₆ peptides bound to a 1.5 nm AuNP.....	12
2.3	FT-IR spectra of His ₆ -peptide and His ₆ -peptide bound to AuNP.....	14
2.4	FT-IR spectra of Cys-peptide and Cys-peptide bound to AuNP.....	16
2.5	FT-IR spectra of Ser-peptide and Ser-peptide bound to AuNP.....	17
2.6	¹ H – ¹ H TOCSY spectra of His ₆ -peptide and His ₆ -peptide with AuNP.....	18
2.7	¹ H – ¹ H TOCSY spectra of Cys-peptide and Cys-peptide with AuNP.....	18
2.8	¹ H – ¹ H TOCSY spectra of Ser-peptide and Ser-peptide with AuNP	19
2.9	Model of the His ₆ -peptide interaction with the AuNP surface.....	21
3.1	Electrostatic surface model of FGF1 with three AuNP interaction sites.....	24
3.2	TEM of 1.5 nm AuNP and UV-Vis spectrum of AuCAAKA and AuCAAKA-FITC 26	
3.3	AuCAAKA-FITC Molecular Beacon analysis of FGF1 and FGF1-heparin.....	28
3.4	Far-UV CD spectra of FGF1 and FGF1-AuNP during time course experiment.....	30
3.5	¹ H – ¹⁵ N HSQC spectrum of FGF1 and FGF1-AuNP at 18 h.....	32
3.6	Expanded HSQC spectra for FGF1 and FGF1-AuNP at 0, 5, and 18 h.....	33
3.7	Δδ plots of FGF1 and FGF1-AuNP at 0, 5, and 18 h.....	35
3.8	Δδ plot of FGF1 and FGF1-heparin	36

3.9	$^1\text{H} - ^{15}\text{N}$ HSQC of large change region for FGF1-AuNP and FGF1-heparin-AuNP at 18 h with $\Delta\delta$ plot for all resonance changes in the sample.....	37
4.1	Model of possible biological surface ligands on nanomaterials.....	42
4.2	Endocytosis and macropinocytosis intracellular uptake mechanism.....	45
4.3	Molecular model of CAAKA-DOTA-Dy(III).....	46
4.4	CAAKA-DOTA-Dy(III) purification by RP-HPLC.....	47
4.5	Diagram of cell-layer in agarose tissue mimic for MR experiments	49
4.6	Live-cell imaging of CHO cells transfected with InP/ZnS-CAAKA-DOTA-Dy(III) using cationic liposome.....	51
4.7	MR image of T2 (negative contrast) with InP/ZnS-CAAKA-DOTA-Dy(III) in agarose tissue mimic	52
4.8	MR image and 3D Gradient Echo of InP/ZnS-CAAKA-DOTA-Dy(III) dosing experiment.....	53
4.9	MR image of InP/ZnS-CAAKATat-DOTA-Dy(III) in solution and in agarose without CHO cells.....	54
4.10	3D Gradient Echo image of InP/ZnS-CAAKATat-DOTA-Dy(III) with and without cationic liposome transfecting agent.....	54
5.1	Schematic model of IDNA and siRNA labeled 5.7 nm AuNP.....	61
5.2	2% TBE-Agarose gel showing distinct mobility for siRNA, siRNA / IDNA, and IDNA appended Au5.7 nm.....	62
5.3	Epifluorescence image of green, red, and green / red / DIC overlay images of eGFP knockdown and DsRed transient expression.....	63
5.4	Time-dependent knockdown of media-secreted eGFP protein fluorescence.....	65
5.5	Red and green channel fluorescence image showing AuNP located within the Lec-1 cells 36-hours after transfection.....	66
5.6	Molecular beacon analysis of AuNP-IDNA with AF594 and AuNP-dsDNA with AF488 for AuNP surface release and endosomal escape kinetics.....	69
5.7	DIC / epifluorescence overlay of endosome repackaging and transport during mitosis.....	70

LIST OF ABBREVIATIONS

AuNP	Gold Nanoparticle
CMV	cytomegalovirus
DIC	Differential Interference Contrast
DOTA	1,4,7,10-tetraazacyclododecane-1,4,7,10-tetraacetic acid
DTPA	Diethylene Triamine Pentaacetic acid
FT-IR	Fourier Transform Infrared Spectroscopy
HSQC	Heteronuclear Single Quantum Coherence
IDNA	linearized plasmid DNA
NP	Nanoparticle
PBS	Phosphate Buffered Saline
PL	Photoluminescence
QD	Quantum Dot
siRNA	short interfering RNA
TEM	Transmission Electron Microscopy
TOCSY	Total Correlation Spectroscopy

ABSTRACT

The scope of this dissertation is two-fold: assembly of histidine-tagged peptides and proteins directly to the surface of a 1.5 nm AuNP and the assembly and delivery of nano-medical materials for MR imaging and gene therapy. Chapter 1 is a general introduction and describes the reason I chose to pursue my graduate career at the interface of biochemistry and nanomaterials. The introduction chapter provides a historical background for both biochemistry and nanomaterials, and shows the parallels of these two fields. Although biochemistry has been more extensively studied in the past century, the opportunities and current applications make nanotechnology a very attractive field. The merger of biochemistry and nanomaterials in the last decade has opened new doors to medical imaging, medical devices, drug delivery, and has expanded our ability to probe fundamental biochemistry and biophysics questions once out of our reach.

Chapters 2 and 3 describe an attempt to elucidate and confirm the ability to bind hexahistidine-tagged (His₆) peptides and proteins directly to the surface of a AuNP. Until now, only Cys amino acids could be used to bind directly to a AuNP surface, otherwise elaborate surface modifications such as antibody-antigen interactions and AuNP surfaces modified with metal chelators such as NTA were necessary for controlled peptide / protein surface interactions. Using FT-IR, NMR, CD, and fluorescence spectroscopy, the direct, covalent attachment of His₆ peptides is confirmed and the directed attachment of a model protein (FGF1) is described. The His₆ – AuNP interaction is shown to occur through the Nε of the His side chain and is able to displace a Cys peptide for binding, suggesting that the binding interaction is tight due to the multi-chelator effect of the six His residues. Furthermore, studies with the FGF1 protein confirm that the AuNP binding does not perturb the structure / function of this protein and suggests that the His₆-tag can be a viable alternative to engineered Cys residues for future bio-nano applications with proteins.

In Chapter 4 I present my research with developing new, high field and bimodal contrast agents for MR and optical microscopy imaging. MRI has become a valuable,

non-invasive clinical diagnostic tool, and with the development of new contrast agents (CA), it is slowly becoming a technique with sensitivities rivaling radionuclei PET scans. The goal of this research was to develop a bimodal contrast agent using an InP/ZnS semiconductor quantum dot appended with a peptide and macrocyclic lanthanide chelator (DOTA). Besides developing a bimodal contrast agent, the goal was to use this material as high field (21.1T), which required the use of Dy(III) as the paramagnetic ion in the DOTA chelator. Bimodal contrast was achieved by transfecting CHO cells with the InP/ZnS-peptide-DOTA-Dy(III) and observing quantum dots optically via live cell imaging or by MR microscopy by suspending the CHO cells in an agarose tissue mimic. The bimodal contrast succeeded in both the fluorescence optical detection and the negative contrast detection by high field MR imaging.

Chapter 5 describes the ability to co-label a 5.7 nm AuNP with siRNA and linearized DNA for simultaneous dual gene regulation. The study was performed using two fluorescent proteins as optical signatures, eGFP (siRNA knockdown) and DsRed-express (delivered linear DNA). Using cationic liposome transfecting agents, the bimodal gene regulator is delivered to Lec-1 cells and CHO cells and shows efficient gene knockdown for eGFP up to 42 h after transfection but shows less efficiency for transient expression of the linearized gene, which was not detected until 36 h after transfection. An NSET molecular beacon study with dye-labeled linearized DNA and short dsDNA revealed that the short strand was able to release from the AuNP surface more efficiently and had more rapid and efficient endosomal escapes, which is known to be a rate limiting step in transient gene expression. The linearized DNA showed slower AuNP surface release and substantially less endosomal escape. The molecular beacon results confirm that the shorter siRNA strand can interfere with eGFP much more rapidly and efficiently given the rate of endosomal escape, whereas the low transient protein expression is not surprising given the low endosomal escape rate for the larger 2 kilobase, double-strand linearized plasmid DNA regulator.

CHAPTER 1

INTRODUCTION

Ancient Greek philosophers are often credited with the first atomistic description of our living world, beginning with Empedocles explanation of the four root elements, fire, air, water, and earth in 440 BC [1]. Shortly after Empedocles' doctrine in 400 BC, the four bodily fluids were described (blood, phlegm, yellow bile, and black bile), and deficiencies in any of these body fluids could explain the root of illnesses [1]. Although these early ideas have become irrelevant by today's scientific standards, this began the transformation from philosophical ideas to scientific thought and reasoning. Unlike 2000 years ago, scientists today rely on facts, reason, and the scientific method to explain our natural world.

The field of biochemistry, the study of the composition of matter in living organisms, was being developed since the 19th century, with many critical scientific discoveries occurring in the early-to-mid 1900's. Early work in biochemistry was done in the 18th and 19th centuries, including the isolation of albumins and fibrins and the classification of these macromolecules as proteins in 1838 by Mulder and Berzelius [2]. It wasn't until the 1950's that biochemistry really exploded, with the determination of the double helix structure of DNA in 1953 by Watson, Crick, Wilkins, and Franklin and in 1958 the first protein structure by X-ray crystallography of whale myoglobin [3, 4]. In addition to discovering the double-helix structure, Watson and Crick determined that DNA was the code of life since both strands of DNA could be replicated without impacting the original helix structure. The discovery of the double helix structure of DNA resulted in Watson, Crick, and Wilkins receiving the Nobel Prize in medicine in 1962 [4]. These initial findings by Watson, Crick, Franklin, and Wilkins have culminated with the completion of the human genome project in 2001, which details all the genes (DNA sequences) in humans [5].

Nanotechnology as a field is even younger than biochemistry; the term "nanotechnology" was first used by Norio Tanaguchi in 1974, but was intended to refer

to precise manufacturing in production technology to the 1 nm resolution.[6] Present-day nanotechnology typically refers to measuring, synthesizing, and manipulating those materials that measure less than 100 nm. Current nanotechnology resembles ideas first mentioned by Richard Feynman in his 1959 Nobel Prize speech in “There’s plenty of room at the bottom”, where he discusses miniaturized devices and the possibility of nanomaterials by the year 2000 [7]. Though the historical accounts of nanotechnology are far fewer than biochemistry, nanomaterials, especially colloidal gold and silver nanomaterials, have been identified in historical items including stained-glass windows, ceramics, and an ancient Roman goblet, the Lycurgus cup. The Lycurgus cup displays different colors depending on the direction of light, whether the light is transmitted (red color) or reflected on the outside of the cup (green color) [8-11]. It was in 1857 when the scientific community was first formally introduced to the unique and interesting spectroscopic properties of colloidal gold when Michael Faraday delivered his Bakerian Lecture on “Experimental Relations of Gold (and other Metals) to Light” [12, 13]. This could mark the birth of nanotechnology – except that no subsequent research in nanomaterials was performed until the latter half of the 20th century.

Nanotechnology has revolutionized medical imaging, medical treatment, cell biology and biochemistry research, defense applications, electronics, and it can be found in many consumer goods. Two important discoveries in nanotechnology in the last twenty-five years have transformed the field into what it has become today: the discovery of Buckminster fullerene (C₆₀) in 1985 [14], which began research with carbon nanotubes, and the synthesis and characterization of luminescent, semiconductor nanomaterials (quantum dots) in the early 1980’s by Brus, Grätzel, and Henglein, among others. [15-20]. Modern scientific research with nanomaterials includes carefully controlling the atoms, molecules, size, and physical properties of these materials, which are markedly different in the nano-size compared with the bulk counterpart. Bulk materials are any metal or semiconductors that are tangible items found in our everyday lives, including copper (in copper wire), iron oxide (rust), tin, or titanium. Some common bulk materials synthesized as nanomaterials are gold and silver (coinage metals), which are typically chemically inert, do not oxidize, and can there be used in biological systems without much concern. Semiconductor materials such as CdSe, InP, CdS, and

CdTe, are unique nanomaterials that exhibit size-dependent fluorescence properties, due to quantum confinement, and lend their unique spectroscopic properties to advances in biological and medical imaging and detection [21-26]. Potential medical applications with CdSe, CdS, and CdTe have been limited due to concerns about cadmium, selenium, and tellurium environmental and biological toxicity.

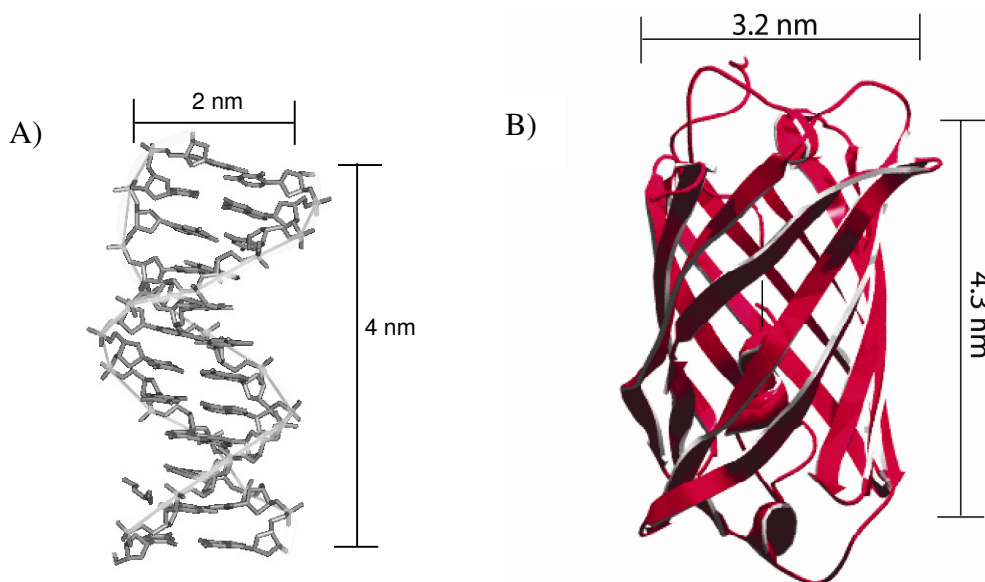


Figure 1.1: A) 12-base pair double strand DNA showing 2 nm helix width and approximate length of this DNA strand (PDB ID: 355d). B) Model of the red fluorescent protein (DsRed) from *Discosoma sp.* of reef corals (PDB ID: 2VAD).

Most biomolecules, including proteins, DNA, and RNA could easily be classified as nanomaterials. Duplex DNA and RNA are approximately 2 nm wide (Figure 1.1), although the length can vary substantially depending on the number of nucleotides in the sequence. For instance, in Figure 1.1 a model of a 12 base pair double-strand DNA molecule that has a width of 2 nm and a length of approximately 4 nm is shown. For a relative size comparison, also shown in Figure 1.1 is a crystallographic model of a DsRed protein. Proteins have much greater variability in length and width depending on the number of amino acids in the primary sequence and folding constraints. Most soluble protein monomer subunits will be less than 10 nm in diameter. Given the sub-microscopic size of most biological molecules, special techniques such as NMR and X-

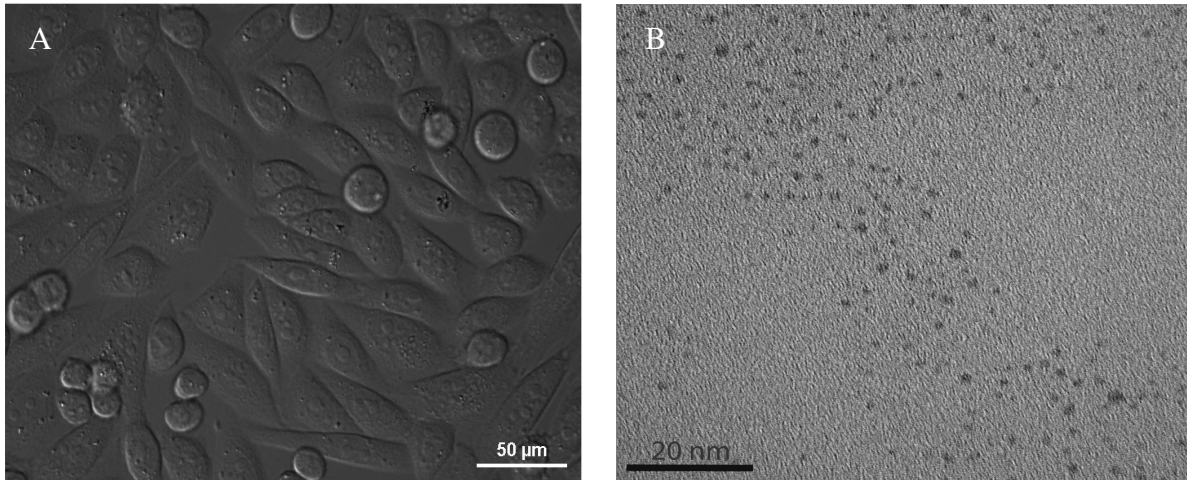


Figure 1.2: A) Brightfield Differential Interference Contrast (DIC) image of CHO cells at 40X magnification. B) Transmittance electron microscopy (TEM) image of 2.0 nm gold nanoparticles (average size) on a carbon mesh background.

Ray crystallography (an X-ray diffraction technique) are required to model the size and shape of proteins, RNA, and DNA, whereas nanomaterials can be visualized using an electron microscope using electron diffraction (Figure 1.2). Normal microscopy techniques used to visualize cells do not afford the resolution necessary to visualize nanomaterials. For instance, Figure 1.2 displays an image of a Chinese hamster ovary (CHO) cells at 40x magnification, which shows that these cells are approximately 10 μm wide on average. The TEM (transmission electron microscopy) in Figure 1.2 shows gold nanoparticles that are 1.5 nm wide on average (according to the scale of the image). In perspective, it would take 600 to 700 gold nanoparticles (1.5 nm wide) to span the width of these CHO cells.

Nanomaterials, like proteins, can exhibit great variability in size and shape. Nanomaterials are chemically synthesized with specific sizes (or shapes) depending on the exact applications they will be used, whereas proteins are not synthetic and are usually grown in organisms under controlled conditions. Nanomaterials and proteins can both be engineered to maximize or minimize specific properties. Protein engineering usually involves mutations in the amino acid sequence of the protein to elicit changes in structure or function. Many of the solution properties and biological application properties of nanomaterials are controlled through the use of ligands (any

molecule that can be attached to the surface and can be any chemical or biological molecule). Most nanomaterials are metals or semiconductors and cannot be dissolved in solution without ligands on the surface; if metals did dissolve in solutions without ligands we would all have to park our cars in a garage when it rains! These ligands can be specific for organic, aqueous, and /or biological solutions, and without the correct surface ligand the nanomaterial will not dissolve in solution just like oil and water do not mix.

Researchers are combining the unique features of nanomaterials to probe questions in biochemistry, biophysics, biology, and medicine. Presently, a major area of scientific research has become bio-nanotechnology. Bio-nanotechnology applies the unique properties of nanomaterials to probe biological problems, including medical imaging, biophysics problems, gene therapy, and biological sensing. There are currently a number of FDA-approved nanomaterials for human use including nanomaterials used in formulating improved sunscreens, cosmetics, and MRI contrast agents with many more nanomaterial based products likely to emerge in the near future. Many of these new bio-nano products require thorough research to assess the biological impact and any environmental safety concerns.

With the growing use of nanomaterials for biological applications, it has become necessary to continue to understand the full potential (or negative impact) that nanotechnology can have on biology and medicine. I was attracted to research in bio-nanotechnology for this reason and others. I believe that my fundamental understanding of biochemistry, especially protein structure and function would be invaluable to begin to understand the molecular interactions between nanometal surfaces and biomolecules. At the time of my decision to pursue graduate work in bio-nanotechnology, nanomaterials were already being delivered to cells and were being used to track structural changes in DNA and RNA using a modified FRET approach, where the nanomaterial acts as a fluorescence quencher (instead of using a small molecule quencher). The advantage to using nanomaterials for FRET, termed NSET (nanometal surface energy transfer) is that it is now possible to probe long distance interactions in real time with minimal sample. Minimal sample and real-time measurements over longer ranges was very appealing since many biochemistry

techniques require substantial amounts of purified sample (NMR, crystallography) and often only give a static description of the protein structure (crystallography).

Furthermore, nanomaterials also provide more robust and photostable materials for improved enzyme assays using a molecular beacon approach. The use of nanomaterials in biochemical analysis provides a more powerful method for real-time structural analysis, more sensitive bio-assays, and lends unique spectroscopic and magnetic properties to the new assays that haven't been dreamed of, yet.

The goal of my doctoral research was to further the field of bio-nanotechnology on two fronts: understanding the molecular impacts of peptides and proteins on the surface of a gold nanoparticle and to assemble and deliver peptides and nucleic acids for improved MRI imaging and gene therapy applications. Using carefully designed peptide sequences, I studied the molecular interactions of a His₆ peptide with the surface of a gold nanoparticle. In Chapter 2, I present the experimental results and binding model that demonstrate the feasibility of using His₆ peptides for gold nanoparticle binding. In Chapter 3 of this dissertation, I expand the His₆ peptide binding studies to determine whether a His₆ protein (acidic fibroblast growth factor, FGF1) is able to bind to the gold nanoparticle surface without negatively impacting the native structure and function of the protein. The result from this complete biophysical study suggests that FGF1 interacts with the gold nanoparticle (AuNP) through the His₆ tag and retains the structural integrity necessary for heparin binding function. In Chapter 4 and Chapter 5, I examine intracellular delivery of nanomaterials for two unique biomedical applications: bimodal MR imaging with fluorescent quantum dots and bimodal gene regulation with transient gene delivery and siRNA (short interfering RNA) gene knockdown. Chapter 4 is devoted to my research on the development of a novel bimodal MRI contrast material using InP/ZnS quantum dots with dysprosium-peptide conjugates on the nanomaterial surface. The quantum dot is used for fluorescence microscopy imaging of live cells while the dysprosium-peptide conjugate produces negative MRI contrast of the CHO cells in an agarose tissue mimic. Finally, Chapter 5 examines the cationic liposome mediated transfection of AuNPs dually labeled with siRNA and linearized gene fragment for simultaneous gene knockdown and transient protein expression in a single cell. This unique bio-nanomaterial displays the

capabilities of nanotechnology, since the large surface area per nanoparticle allows co-delivery of gene therapeutics to one location for enhanced gene control mechanisms.

I consider my doctoral research to be a mix of basic, fundamental science, especially with the His₆ peptide and protein research, as well as applied science for the bio-nanomedical research to develop a novel bimodal MR contrast agent and dual gene regulatory nanomaterial platform in vivo. The research presented in all chapters of this dissertation will make an important contribution to understanding the structural and functional effects of peptide and protein assembly on to gold nanoparticles, biomedical imaging capabilities, and novel nano-mediated, gene therapy delivery platforms. Future work and applications for this doctoral research will be discussed throughout the text.

Looking Ahead to the Future...

With my fundamental understanding of bio-nano applications and molecular interactions I believe I am in a great position to pursue the development of next generation applications and devices. The first thought that came to mind when I learned about the possibilities of nanomaterials in biochemistry and medicine was the ability to develop prosthetic neurons that had enhanced conduction ability and were sub-micron in size. Treatments for nervous system disorders or nerve and spinal cord injuries could benefit from these nano-neuronal implants. These ideas are not so far-fetched given the exponential increase in bio-nanotechnology research and fundamental understanding of protein and DNA interactions in vitro and in vivo. I envision that bio-nanotechnology will one day create pacemakers the size of a grain of sand that can be controlled and monitored on our cell phone. Nanotechnology may one-day result in the development Implantable drug delivery devices that can release drug doses using microwaves emitted from our own wrist watch – no more missed doses or overdoses. Bio-nanotechnology is revolutionizing our world and the best is yet to come!!

CHAPTER 2

HIS₆ PEPTIDE ATTACHMENT TO A 1.5 nm Au NANOPARTICLE SURFACE

2.1 Introduction

Nanoparticle surfaces functionalized with proteins or other biomolecules provide a mechanism for interfacing the unique properties of nanomaterials with biological samples. For instance, appending peptides or proteins to a nanomaterial surface can enhance cellular transport of these bio-nanomaterial conjugates, augment optical and / or magnetic cell imaging, and improve the sensitivity and throughput efficiency for bioassays [27-40]. The majority of these studies have conjugated proteins and peptides to the AuNP surface through the thiol group of native or introduced cysteine residues. However, the reliance on Cys residues for anchoring to the AuNP can be problematic for proteins containing a large number of intrinsic Cys residues (lack of specific site binding), and unstable proteins (Cys mutation may destabilize the protein). Introducing additional Cys residues may also reduce the folding yield of a protein due to inappropriate disulfide bond formation and the generation of misfolded states. This chapter investigates the feasibility of using the hexa-histidine (His₆) sequence as a method for attaching synthetic peptides directly to AuNPs. Spectroscopic evidence indicates that the His₆-tagged peptides bind to the AuNP surface via formation of multiple Au-imidazole interactions with the N ϵ .

The advantage of the His₆ coordination approach is that the methodology is applicable to protein attachment since recombinant protein expression systems routinely engineer a His₆ tag to enhance purification through immobilized metal affinity chromatography using nitrilotriacetate (NTA)-bound Ni(II) ions. There are several other advantages to this approach. First, if successful, this approach would significantly simplify the labeling chemistry; second, one would retain the high regio-specificity of the His-tag as an attachment vehicle; third, since the His-tag generally has minimal affect on protein structure and function, this approach might be less perturbative than

attachment through the thiol functionality of Cys residues; and fourth, the ubiquity of the His-tag in expression vectors simplifies design and generation of the appropriate gene constructs. Hexa-His binding was previously demonstrated to be an effective method for attaching His-tagged proteins to NTA-passivated gold surfaces and nanoparticles [41, 42]. Here, however, I focus on direct attachment of His-tagged peptides to small (< 2 nm) AuNPs without the requirement of a metal mediated NTA linkage chemistry.

A comparison of the binding of His-tagged peptides to Cys and Ser peptides of the same sequence enables an investigation of the interplay between coordination, hydrophobic effects, and electrostatic interactions on the peptide assembly process at the AuNP surface. The single peptide sequence has a constant amino acid sequence, XEDDKLVPRGSEWDW with variable attachment residues at the amino terminal “head group” (X= Cys, Ser, or His₆). The peptide likely exists as a random coil in solution and is unlikely to adopt a specific secondary structure upon complexation with the AuNP. There are several possible binding motifs for this peptide to bind to the AuNP, namely direct head group chelation to Au, interactions with terminal amine or carboxylate of the peptide, and electrostatic and / or van der Waal interactions with amino acid side chain groups (all residues in this peptide sequence have shown Au binding with the exception of valine and glutamic acid) [43-47]. The Cys-containing peptides are expected to bind via a Au-thiol linkage at the metal surface [45, 48-55], while the Ser has no expected molecular coordination through the head group [44, 45]. The His₆ linkage may either coordinate via the imidazole ring or may be dominated by the charge interactions. The Au-imidazole interaction is weaker than the Au-thiol interaction [44, 45], but the His₆ head group may have a higher effective affinity through multiple chelation events. Thus, the specific nature of the peptide - Au interaction will reflect a competition between peptide-specific properties (charged and hydrophobic groups) and the binding of the head group at the N-terminus.

2.2 Methods and Results

The 1.5 nm Au is prepared by literature methods either as the triphenylphosphine (TPP) or the bis(sulfonatophenyl)-triphenylphosphine (bSPP) passivated nanometals

[56]. AuNPs are transferred into the aqueous buffer at room temperature by one of two methods. One method is a direct exchange of the passivating ligand bSPP on Au by the peptide in phosphate-buffered saline buffer for 30 min (125 μ M in 20 mM phosphate buffer, pH 7.5, 50 mM Na phosphate; PBS) [56-62]. In a second approach, TPP-passivated AuNPs in CH_2Cl_2 are transferred into aqueous phase through a biphasic ligand exchange with peptides dissolved in PBS. In this case, reaction progress was monitored by absorption of the aqueous phase and was found to be essentially complete after 1 hour. Biphasic exchange at higher pH (8.5) resulted in more rapid ligand exchange (complete in < 10 min) for the His₆ and Cys head groups, but was not pursued due to possible complications arising from more facile disulfide bond formation at elevated pH. In both methods, the aqueous sample was purified by gel filtration (G-25 Sephadex) to remove residual peptide and to change the solvent to nanopure water following exchange.

The extent of binding of the three different peptides to the AuNP was assayed by tracking the fluorescence quenching of the single Trp residue in the peptide sequence upon interaction with the AuNP surface. This molecular-beacon type assay is based upon previously published nanosurface energy transfer (NSET) technology [63, 64]. The predicted quenching efficiency of the Trp by the AuNP at the expected separation distance is 50% based upon an NSET analysis if the peptide binds through the head group. In these experiments, the peptide was exchanged onto bSPP passivated AuNP using equimolar stoichiometry of the Au to the peptide and the total fluorescence at $\lambda_{\text{em}} = 360$ nm measured after 5 min. The total Trp fluorescence for the gold samples was compared to equimolar control samples of the peptides in the absence of gold providing a quenching magnitude (I/I_0).

The three peptides exhibited similar quenching magnitudes (47 ± 5 , 45 ± 3 , and 54 ± 2 percent for Cys, His₆, and Ser head groups, respectively) following ligand exchange (Figure 2.2). The quenching indicates that the peptide associates with the AuNP for all three head groups, but does not provide insights into the molecular aspects of the interaction, more specifically, whether association occurs via electrostatics, hydrophobicity, or chelation to the metal surface. The similar extent of quenching for the Cys, His₆, and Ser head groups was surprising, as only Cys and His were expected

to coordinate directly to the AuNP via a head group interaction. Assembly of all three head groups onto the AuNP suggests coordination via non-covalent interactions may also play a role in the peptide assembly onto the AuNP. The nature of the non-covalent peptide-AuNP interaction was further investigated by the addition of guanidinium hydrochloride (GuHCl) to the peptide-AuNP solution (Figure 2.2). Weak electrostatic interactions should easily be disrupted by GuHCl, resulting in dissociation of the peptide from the AuNP and re-appearance of tryptophan fluorescence. Interestingly, the three peptides exhibited identical responses to added GuHCl up to 2.5M addition in PBS, pH=7.5 (Figure 2.2) suggesting that electrostatics is not a major contributor to peptide assembly on the Au surface for any of the peptide sequences, and implicating that both head group and side chain interactions as being important in binding. This observation is not surprising, as the importance of side chain binding interactions for stabilization of proteins onto surfaces has been observed in Phage display and implicated as a critical component for surface fouling of semiconductors and metals [45].

The stoichiometry of peptide to AuNP was analyzed by optical absorption spectroscopy (Figure 2.2) from the A280 : A420 intensity ratio. The concentration calculation assumes that the intensity at $\lambda = 280$ nm arises from the peptide (Trp,W) plus AuNP, whereas intensity at $\lambda = 420$ nm was due to the AuNP alone [65]. This

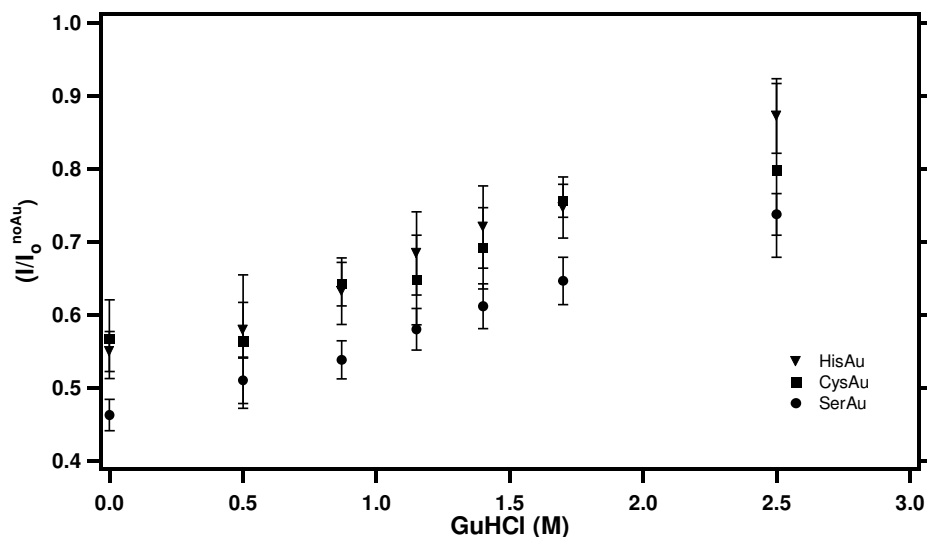


Figure 2.1: Fluorescence Molecular Beacon Assay for added GuHCl to a solution containing Au-Cys, Au-His, and Au-Ser. The fluorescence recovery at each point is corrected for the Trp fluorescence contribution of the free peptide at each GuHCl concentration.

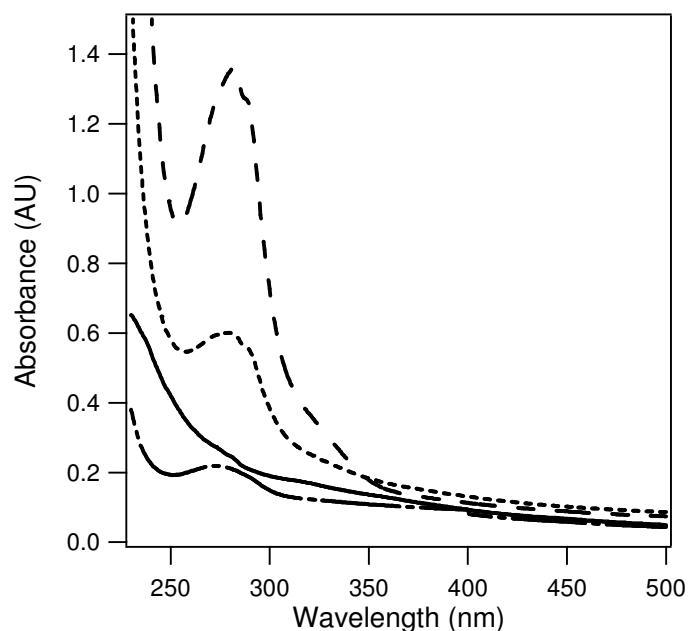


Figure 2.2: Absorption spectra in PBS buffer (pH=7.5) for 1.5 nm Au-bSPP (—), the Au-Cys peptide (----), the Au-His₆-peptide (····) and the Au-Ser peptide (- · - ·).

approach yielded binding stoichiometries of 38:1, 1:1, and 100:1 for the Cys, His₆, and Ser head groups, respectively. The range of values indicates that a combination of AuNP surface interactions are involved in binding the different sequences, with the specific stoichiometry reflecting the balance of a head group binding directly to the AuNP, other peptide-AuNP interactions, and possibly peptide-peptide interactions at the AuNP surface. The observation of 38 : 1 peptide : AuNP for the Cys head group is consistent with a report of 32 to 45 alkylthiols bound on a 1.5 nm AuNP surface [56]. This stoichiometry implies nearly complete occupancy of every possible binding site at the AuNP surface and suggests a high packing density for the rest of the peptide around the AuNP.

The unit stoichiometry of the hexa-His peptide sequence is surprisingly low and most likely reflects the larger molecular “footprint” associated with binding of one or more his residues at the AuNP surface. Alternatively, the low stoichiometry could reflect thermodynamic instability of Au-His₆ peptide interaction, but this interpretation is

considered less likely as the biphasic exchange was carried out under a 200:1 peptide to Au exchange ratio.

The 100 : 1 binding ratio for the Ser head group peptide is inconsistent with direct binding of the peptide through the hydroxyl head group. The observations for the Cys-Ser peptides compared with the His₆ peptide cannot reflect a simple head group interaction at the surface of the Au, and suggests a more extensive interaction between the amide groups of the peptide backbone and / or with the amino acid side chains. Furthermore, peptide aggregation at the AuNP surface must contribute to the high binding stoichiometry for Ser. The possibility of AuNP diameter increase contributing to the observation of the 100 : 1 ratio can be ruled out due to the absence of a surface plasmon, which is observed in AuNPs greater than 2.5 nm.

The molecular details of peptide binding to the AuNP were investigated from changes in the peptide infrared vibrational resonances upon binding to AuNP. Samples for FT-IR analysis were prepared as described above, lyophilized, and mixed with a 10-fold excess of KBr to form a pellet. Figure 2, shows diffuse reflectance FT-IR spectra for peptides with all three head groups. Complete spectra and tables of tentative assignments are given for the His₆-peptide (Figure 2.3, Table 2.1), the Cys-peptide (Figure 2.4, Table 2.2) and the Ser-peptide (Figure 2.5, Table 2.3). For ease of analysis, each peptide spectra is discussed as Region I (900 – 1100 cm⁻¹) for transitions arising from the imidazole side chain of the His residues, Region II (1100 – 1500 cm⁻¹) for the majority of the amino acid side chain vibrations, and Region III (> 1500 cm⁻¹) that includes vibrations arising from the polypeptide backbone, Amide I and Amide II.

The IR spectral data shows numerous changes in the head group region for His-peptide and Cys-peptide upon complexation to AuNP; no significant change can be deduced for the Ser-peptide due to the overlap with H₂O. The AuNP binding to the His₆-peptide is associated with the appearance of strong transitions at 1008 and 1038 cm⁻¹ (Figure 2.3). These bands can be assigned to new Nε-Au interactions by comparison to vibrational analysis of free histidine amino acids interacting with Au sols [66] through the Nε on the imidazole produced identical vibrational features and are

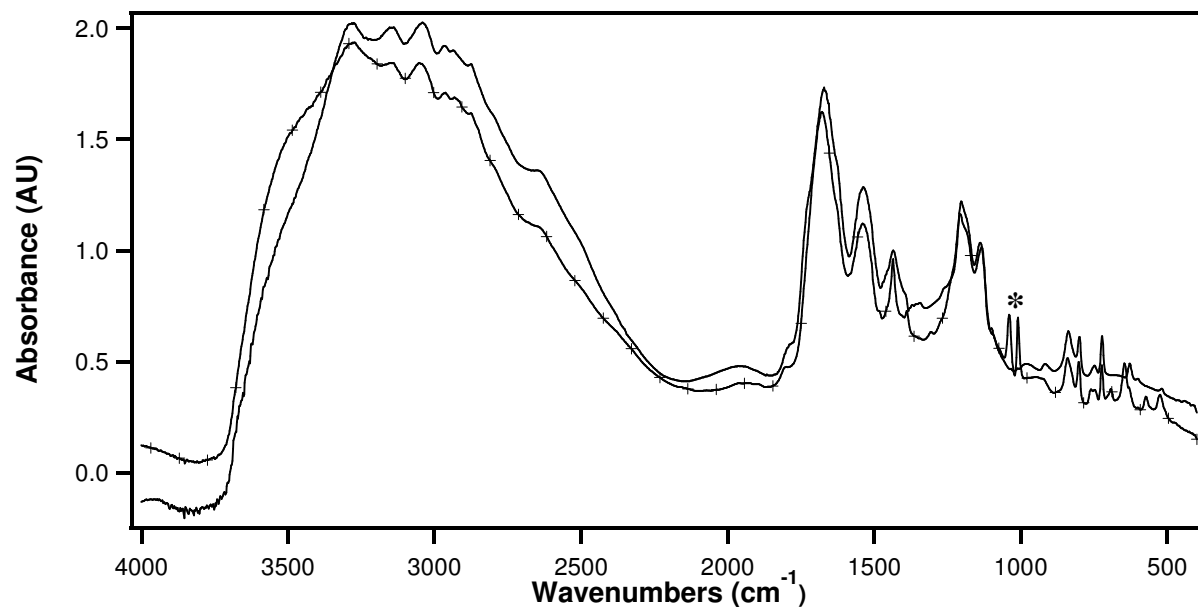


Figure 2.3: FT-IR spectra of His₆ peptide with AuNP (+) and without AuNP (—). The appearance of two new peaks (*) assigned to the N ϵ interaction of His with the AuNP.

Table 2.1: FT-IR peak assignments for His₆ peptide and His₆ peptide with AuNP

His (cm ⁻¹)	HisAu (cm ⁻¹)	Tentative Assignment	Reference
627		Amide IV, Amide VI	[67]
	646	Amide IV, Amide VI	[67]
	692	Amide IV, Amide VI	[67]
721	723	Amide IV, Amide VI	[67]
	756	Amide IV, Amide VI	[67]
800	802	Amide IV, Amide VI	[67]
837	839	$\delta r(\text{CH}_2)$	[68, 69]
917		$\delta r(\text{CH}_2)$: His C-H in plane bending	[68-70]
966		His CH ₃ rock, N ₃ C ₄ stretch, ring def. 1	[68-70]
	1008	His (C ϵ -N ϵ) Au interaction; ring def 2, C ₄ C ₅ st, CH ₃ rock	[66, 71]
	1039	His (C ϵ -N ϵ) Au interaction; CH ₃ rock (N δ) protonation	[66, 71]
1134	1130	$\nu(\text{C-O})$ Asp, Glu	[67-69]
1205	1207	$\gamma w\text{CH}_2$, $\nu(\text{CC})$ Trp,	[67-69]
1344		Trp	[67-69]
	1389	(CH ₃) in-plane bending	[67-69]
1435	1435	Trp $\delta(\text{NH})$, $\nu(\text{CC})$, $\delta(\text{CH})$; His-1 $\delta(\text{CH}_3)$, $\nu(\text{CN})$	[67-69]
1535	1535	Amide II	[70]
1622		Trp $\nu(\text{CC})$, $\nu(\text{C=C})$	[68, 72]
1670	1678	Amide I	[45]
1797	1807	Asp, Glu $\nu(\text{C=O})$	[68, 72]

consistent with vibrational modes present in FT-IR spectra of protonated methylimidazole [71]. The appearance of these bands in our spectra provides strong evidence of a direct interaction between the imidazole ring(s) and the AuNP surface. Evidence for a direct Cys-AuNP interaction is seen in the FT-IR spectra based on the loss of a Cys R-S-H vibration at 2550 cm^{-1} [73] upon addition of AuNP.

Amino acid side chain interactions with the Au surface results in changes in the IR spectra in Region II ($1100 - 1500\text{ cm}^{-1}$). There are no significant changes observed in this region for the Au-His₆ and Au-Ser systems, but addition of AuNP induces large changes in the FT-IR spectrum of the Cys-peptide. The Cys-peptide with AuNP results in the loss of vibrations associated with the glutamate and aspartate side chain carboxylates (1136 cm^{-1}), loss of a Trp vibration at 1344 cm^{-1} , and appearance of new bands at 1240 cm^{-1} , 1315 cm^{-1} , and 1400 cm^{-1} . In addition, a shift ($\Delta\nu = 6\text{ cm}^{-1}$) in the band assigned as the δNH and νCC vibration for tryptophan the backbone νCN vibration for proline is observed. These spectral differences may indicate changes in vibrational symmetry, hydrogen bonding, or screening of the dipole if perpendicular to the AuNP [73] upon complexation to AuNP.

The large changes in the Cys peptide indicate tight packing of the peptide onto the AuNP surface, as would be expected if each available three-point hollows on the AuNP surface is occupied by a Cys-peptide [74]. The absence of similar changes for the Ser-peptide suggests that this peptide is less tightly constrained upon complexation. These results suggest that Ser interactions are largely non-specific and utilize the backbone interactions predominately to stabilize the assembly at the NP surface, while His and Cys utilize the head group specific binding predominately. The changes in the side chains for Cys therefore are due to packing effects rather than binding interactions at the AuNP surface [74]. The frequency of the amide I band (Region III) is often used to infer secondary structure content, with bands shifted to frequencies lower than $\sim 1650\text{ cm}^{-1}$ indicating more extended structures while those shifting to higher frequency corresponding to helical or random structures. The frequency of the amide I (νCO) is 1678 cm^{-1} (His₆-Au), 1655 cm^{-1} (Cys-Au) and 1661 cm^{-1} (Ser-Au). The frequency of the His₆ peptide Amide I band may indicate more random backbone geometry, consistent with the low packing population of more extended structures.

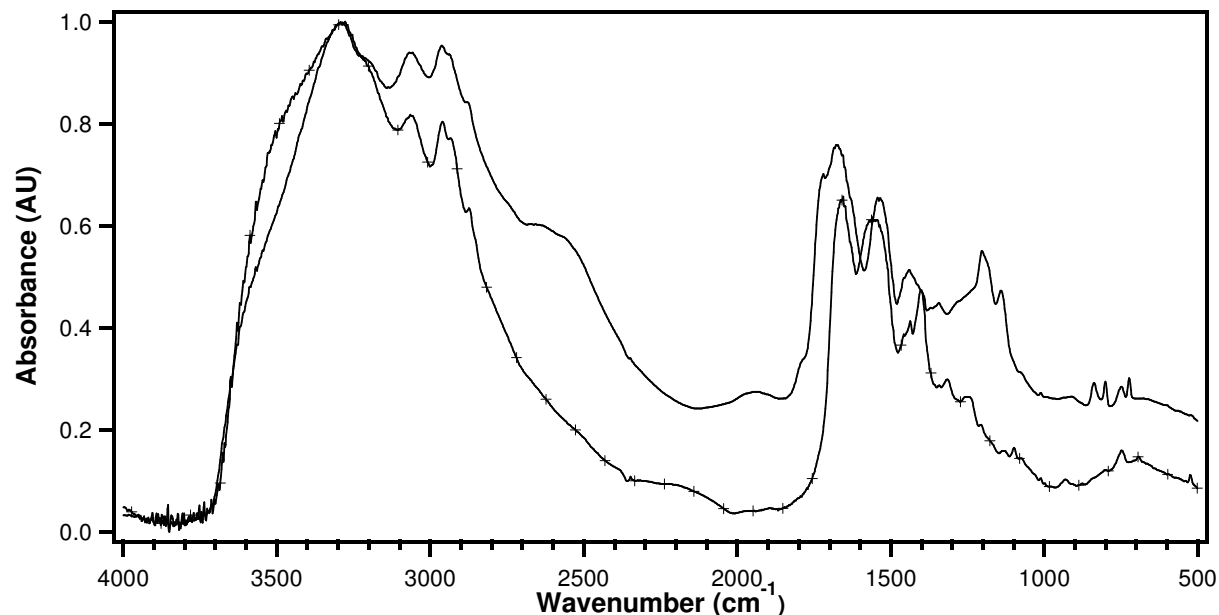


Figure 2.4: FT-IR spectra of Cys peptide with AuNP (+) and without AuNP (—).

Table 2.2: FT-IR peak assignments for Cys peptide and Cys peptide with AuNP

Cys (cm^{-1})	CysAu (cm^{-1})	Tentative Assignment	Reference
	692	Amide IV, Amide VI	[67]
746		Amide IV, Amide VI	[67]
	803	Amide IV, Amide VI	[67]
837	830	$\delta_r(\text{CH}_2)$	[68, 69]
910	931	$\delta_r(\text{CH}_2)$	[68, 69]
	1097	Trp	[68, 69]
1136		$\nu(\text{C-O})$ Asp, Glu	[68, 69]
1196	1187	Trp, Ser	[68, 69]
	1240	Trp	[68, 69]
	1315	$\delta(\text{CH})$	[68, 69]
1344		Trp	[68, 69]
	1400	Asp, Glu $\nu_s(\text{COO}^-)$	[68, 69]
1440	1434	Trp $\delta(\text{NH})$, $\nu(\text{CC})$, $\delta(\text{CH})$; Pro $\nu(\text{CN})$	[68, 69]
1533	1520	Amide II	[67]
1655	1655	Amide I	[67]
1729		Asp, Glu $\nu(\text{C=O})$	[68, 69]

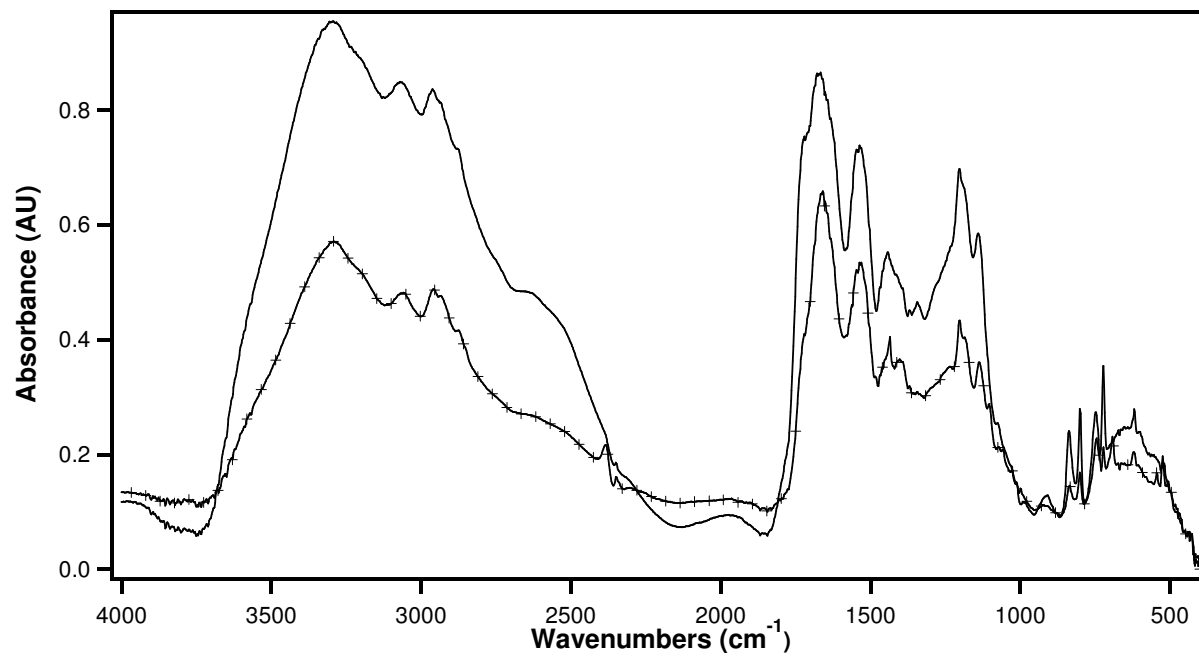


Figure 2.5: FT-IR spectra of Ser peptide with AuNP (+) and without AuNP (—).

Table 2.3: FT-IR peak assignments for Ser peptide and Ser peptide with AuNP

Ser (cm^{-1})	SerAu (cm^{-1})	Tentative Assignment	Reference
721	721	Amide IV, Amide VI	[67]
750	750	Amide IV, Amide VI	[67]
800	800	N-H bending, out of plane	[68, 69]
837	837	$\delta_r(\text{CH}_2)$	[68, 69]
910	910	$\delta_r(\text{CH}_2)$	[68, 69]
1136	1136	$\nu(\text{C-O})$ Asp, Glu	[68, 69]
1203	1203	Trp $\nu(\text{CC})$	[[68, 69]
1342	1342	Trp, Ser	[68, 69]
1445	1445	Trp $\delta(\text{NH})$, $\nu(\text{CC})$, $\delta(\text{CH})$; Pro $\nu(\text{CN})$	[68, 69]
1551	1529	Amide II	[67]
1661	1661	Amide I	[67]
1733	1733	Asp, Glu $\nu(\text{C=O})$	[68, 69]

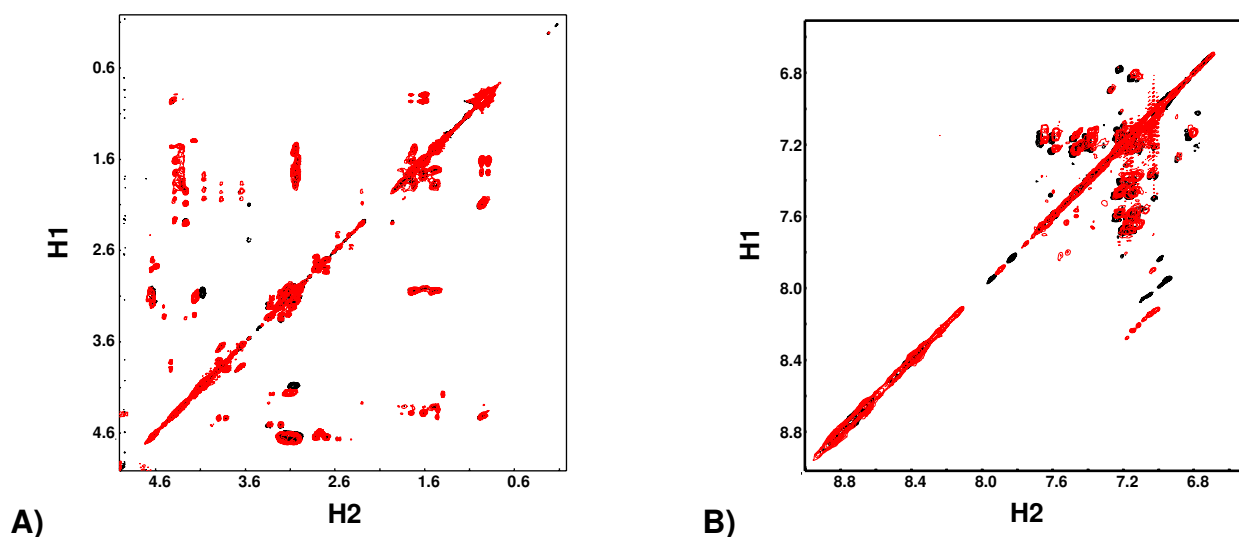


Figure 2.6: 2D-¹H-NMR TOCSY of the unbound His peptide (black) and His peptide bound to 1.5 nm Au (red). A) The NMR spectrum shows changes in the aromatic region following binding on the 1.5 nm Au, especially in the His residues, where a chemical shift in the C δ -C ϵ signal is observed, as well as a slower decay rate for the ϵ -H compared to the δ -H. B) The NMR spectrum shows the His peptide aliphatic side chains, which show little to no change between the two samples.

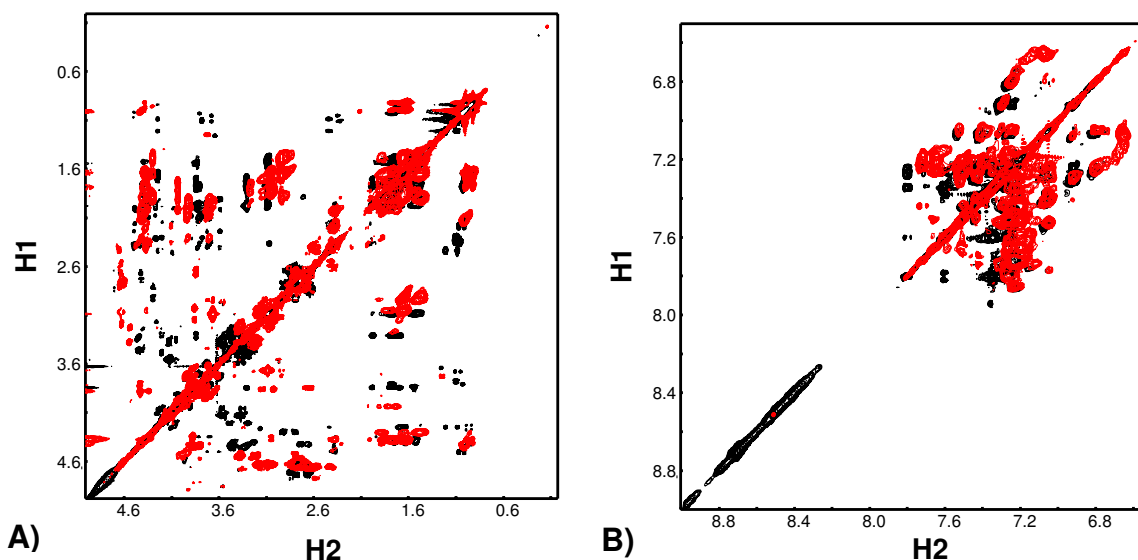


Figure 2.7: Cys-peptide alone (black) and Cys-peptide with AuNP(red) of A) Aliphatic and B) Aromatic Region. The aliphatic region (A) shows widespread changes in the peptide side chains with few changes in chemical shift frequency for protons in the aromatic region (B).

In contrast, the Cys and Ser head group peptides both show a high frequency shoulder on the Amide I band that disappears in the presence of AuNP, perhaps indicating a loss of random or helical structures and increased densities on the AuNP.

The amide II ($\nu_{\text{CN}}, \delta_{\text{NH}}$) vibrations for the Au peptides appear at 1535 cm^{-1} (His-Au), 1520 cm^{-1} (Cys-Au), and 1529 cm^{-1} (Ser-Au). There is little change in the amide II band in the His₆ peptide ($\Delta\nu = 6 \text{ cm}^{-1}$) whereas the Cys- and Ser-peptides showed larger changes ($\Delta\nu = 13 \text{ cm}^{-1}$ and $\Delta\nu = 20 \text{ cm}^{-1}$, respectively). The amide II band arises from a coupling between N-H bending and C-N stretching, but is less responsive to changes in protein secondary structure than the Amide I. Nevertheless, the small change in the His₆ Amide II band and the larger changes in the Cys and Ser Amide II bands indicate that AuNP binding has less impact on the backbone configuration in the His₆ peptide whereas AuNP binding results in larger changes in the Cys and Ser peptides.

Additional information on conformational changes associated with AuNP binding were obtained from NMR spectra. Figure 2.6 shows two regions of a ^1H - ^1H TOCSY spectrum of the His₆-peptide in the absence (black contours) and presence (red contours) of AuNP. Figure 2.6A compares the effect of binding on the aliphatic portion

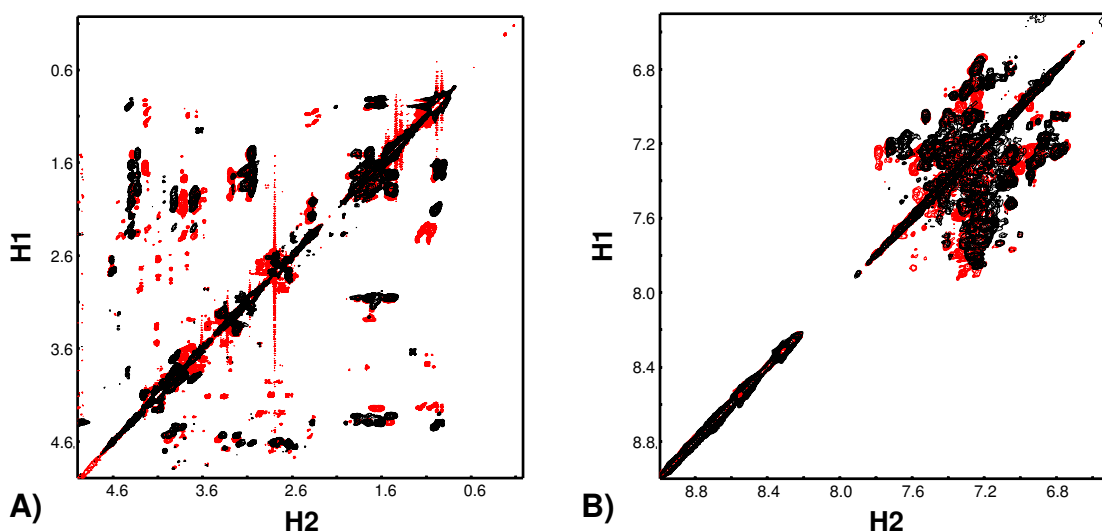


Figure 2.8: Ser-peptide alone (black) and Ser-peptide with AuNP (red) of A) Aliphatic and B) Aromatic Region. The aliphatic region (A) shows numerous shifts in the H α and H β protons of the amino acid side chains. No visible changes are noted in the aromatic region (B) with the addition of the AuNP to the Ser-peptide.

of the spectrum, which contains resonances from the amino acid side chains. In this experiment, coherence transfer is induced between coupled spins, providing a more detailed mapping of chemical shifts and potential chemical shift changes than a simple 1D NMR spectrum. In the His₆ experiment the binding to AuNP has minimal effect on the peptide resonances, except for a cross peak between the H α -H β protons of a His residue. The aromatic portion of the spectrum (Figure 2.6 B) shows correlations among the various Trp resonances as well as correlations between the CH ϵ and CH δ protons of the histidine side chains [46, 75-77]. There is minimal effect on the tryptophan resonances upon complexation to AuNP, but there is a pronounced shift in the resonance frequencies of the CH ϵ and CH δ resonances. The downfield shift in CH ϵ resonance ($\Delta\delta = \sim 0.2$ ppm) in the presence of AuNP is consistent with the deshielding expected if the imidazole ring is complexed to the gold. In vast contrast, a comparison of the aliphatic and aromatic portions of TOCSY spectra of the Cys (Figure 2.7) and Ser (Figure 2.8) peptides change substantially upon complexation with AuNP. These widespread spectral changes indicate changes in the magnetic environment of the amino acid side chains throughout the peptide, as might be seen in the more densely packed environments for these peptides bound to AuNP.

2.3 Discussion and Model

Collectively, these results indicate that the His₆ tail directly complexes to the surface of 1.5 nm AuNPs through side chain imidazole(s), making this a convenient binding functionality for attachment of peptides and proteins to gold nanoparticles. The binding stoichiometry indicates a single His₆-peptide per AuNP, and the NMR and FT-IR results support that binding occurs through the imidazole group on the histidine tag. The low stoichiometry and strong binding suggests a model where multiple chelating events occur, limiting the number of peptides on the surface (Figure 2.9). In contrast, our results suggest a very different bound state for the Cys and Ser peptides. The Cys head group appears to bind at (nearly) every available coordination site through the thiol

group, but the corresponding high packing density orders (or otherwise alters) the peptide conformations. Finally, the Ser head group was chosen as a chemical functionality that was not expected to bind tightly to the AuNP, yet significant binding is observed. Somewhat unexpected, though, was the extensive association between the Ser-peptide and the AuNP. One possibility is that the Ser peptide may form aggregates in solution, with the entire aggregate adsorbing onto the AuNP, but this simple picture is not consistent with the numerous changes in the NMR spectrum, nor is it consistent with the binding strengths reported in the GuHCl experiment. At this point, it is assumed that the Ser-peptide is aggregated onto the AuNP, primarily through backbone interactions, but further experiments are required to develop a clear molecular picture of the bound form of this head group-peptide combination.

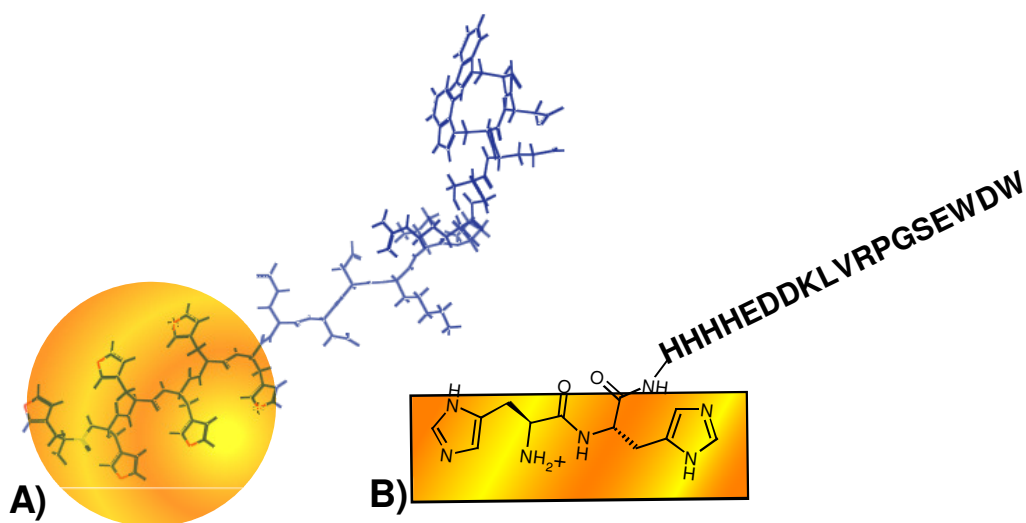


Figure 2.9: Projected packing of the A) His₆ peptide (depicted as beta sheet conformation for modeling purposes) on the AuNP and B) the likely molecular interactions of the His₆ side chains through the NE's (two of the six bound side chains shown for clarity).

In summary, this chapter shows that a hexa-his sequence results in high affinity binding of peptides to AuNP, with high regio-specificity. This result has important implications in biotechnology where the ubiquity of the his₆-tag for recombinant protein expression suggests that this method of attachment could eliminate the need for elaborate surface modifications using solvent-accessible metal chelators, such as NTA, and have a significant impact on efforts to use the AuNP to deliver proteins. Additional

studies, focusing on the binding of His₆-tag proteins to the AuNP are discussed in Chapter 3 of this dissertation.

CHAPTER 3

MAINTAINING STRUCTURE AND FUNCTION OF A RECOMBINANT HISTIDINE-TAGGED PROTEIN ATTACHED TO A 1.5 nm Au NANOPARTICLE

3.1 Introduction

Nanomaterials can be readily interfaced with biological polymers (proteins, DNA, RNA) to act as markers of biological activity, functional interactions, perform as molecular beacons, or be used for delivery of biological materials [22, 27, 38, 47, 78-80]. Appending native proteins onto gold nanoparticle (AuNP) surfaces is hindered by the propensity for protein denaturation at the protein-AuNP interface, as well as the limited repertoire for site-specific attachment of recombinant proteins to the AuNP surfaces [81-86]. Protein denaturation at the nanocrystal surface is a result of unfavorable electrostatic and hydrophobic interactions that effect the protein secondary structure and render the protein inactive. Negative impact on protein structure is a result of the large number of charged ligands on the nanocrystal surface that are necessary for aqueous solubility. Using effectively neutral ligands (pegylated or zwitterionic) ameliorates electrostatic interactions deleterious to the native protein structure and function [87, 88]. Controlling site-specific assembly is also beneficial because the comparable size of nanocrystals and proteins can perturb protein function by blocking protein active sites.

The impact on protein structure and function is dependent on the location of the protein attachment point relative to the active sites on the protein of interest [87, 89, 90]. Site-specific labeling would allow the minimization of these non-specific interactions that can effectively block active sites on the protein thereby maintaining native protein structure and function. While protein denaturation at the AuNP surface can be understood in terms of electrostatic interactions, which can be overcome by appropriate surface charge of the AuNP, the ability to site-specifically label a recombinant protein is complicated, as the mutation of the native protein can lead to misfolding and a loss of function. [49, 51, 80, 85, 86, 91]. Maintaining the structural integrity and functionality of

a protein when appended to the surface of a nanometal is critical if these systems are to be used in bio-medical technologies.

The assembly of proteins onto a AuNP reflects the sum of interactions arising from the backbone or side chains of individual amino acids to the AuNP surface, as well as secondary interactions which enhance stability via van der Waals packing forces, H-bonding, and electrostatics. Herein, the dynamic changes that occur during the assembly of FGF1 (acidic fibroblast growth factor) onto a 1.5 nm AuNP surface through a N-terminal His₆-tag are investigated using molecular beacon binding kinetics, circular dichroism (CD), and NMR. Using these biophysical techniques we will elucidate the overall effect on protein structure and function upon direct AuNP binding.

FGF1 (Human acidic fibroblast growth factor), a protein with mitogenic (cell

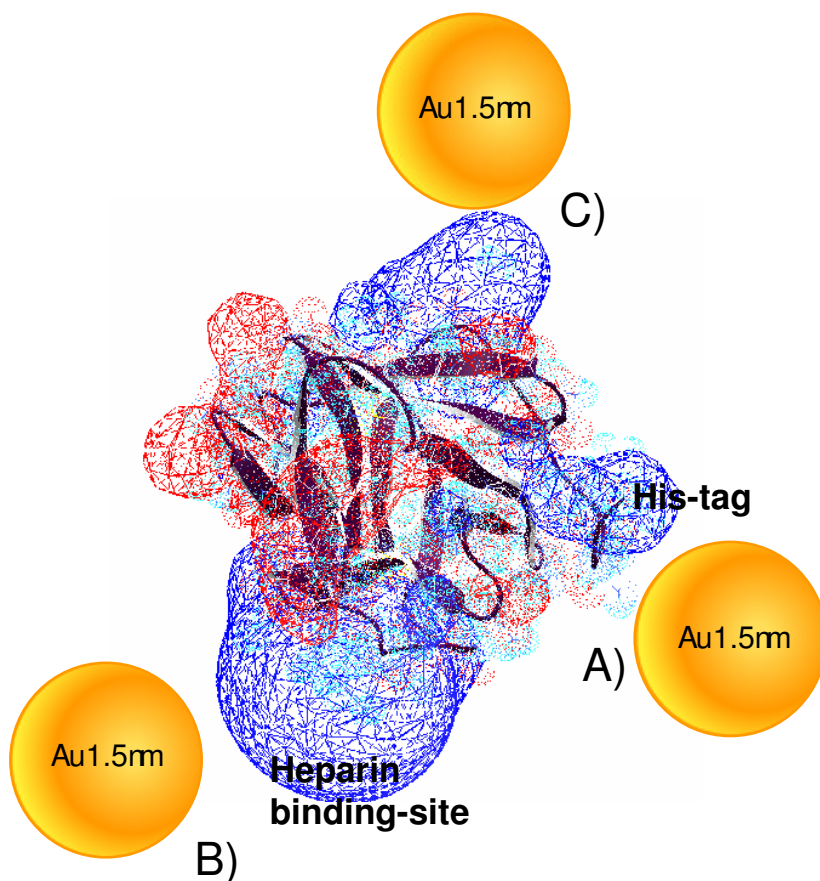


Figure 3.1: Electrostatic surface potential of FGF1 protein (red = negative charge and blue = positive charge) showing a three possible AuNP interaction sites A) His-tag, B) heparin binding site, and C) C-terminal given the high charge density on the protein surface in these regions.

division) and potent angiogenic (wound healing) properties, has emerged as a candidate for revascularization strategies of cardiac muscle following ischemic events [92-94]. FGF1 requires at least an octasaccharide heparin for FGF receptor (FGFR) activation, but can accommodate oligosaccharides of varying sizes in the positively charged heparin binding pocket [95]. This FGF1 protein, whose function is strongly perturbed by electrostatic and structural interactions, is an ideal candidate to probe the use of a His-tag specific labeling strategy for AuNP attachment. In this study we probe the FGF1 (sym6 $\delta\delta$) mutant, which exhibits increased thermodynamic stability and has a substantially lower heparin affinity [96]. Maintaining the bound FGF1-heparin state in this hypoactive mutant assures that Au has no adverse effects on protein function in the presence of the AuNP.

The impact on the structure and function of FGF1 when assembled onto a peptide (CAAKA) passivated 1.5nm Au via hexa-His-tag is analyzed by correlating CD and 2-D ^1H , ^{15}N HSQC NMR spectroscopy. The zwitterionic CAAKA peptide is used to minimize electrostatic complications with the protein surface given the possibility of electrostatic interactions with the heparin binding pocket (Figure 3.1 B) and the C-terminal region (Figure 3.1 C) in addition to the His-tag region (Figure 3.1 A). The results indicate site-specific labeling can be achieved via the His-tag without interfering with protein function, thereby demonstrating that the His-tag commonly used in recombinant proteins can be routinely utilized for integrating recombinant proteins onto AuNP surfaces.

3.2 Materials and Methods

FGF protein (sym6 $\delta\delta$ of human FGF-1).

The amino-terminal His-tag [97] form of the sym6 $\delta\delta$ mutant of FGF-1 [96] (for simplicity, referred to as FGF1) was expressed and purified according to published procedures [97-99]. Briefly, to isolate the His₆ tagged protein from the cell, the cell lysate was centrifuged for 30mins at 20,000RPM. The resulting supernatant was loaded onto a His Prep FF 16/10 column (GE Biosciences) for nickel affinity purification,

followed by size exclusion chromatography (Superdex75 10/300 GL column; GE Biosciences). For 2D-NMR experiments, ^{15}N -FGF was grown in M9 media with $(^{15}\text{NH}_4)_2\text{SO}_4$. All expression and purification procedures for ^{15}N -FGF were identical to unlabeled FGF.

Preparation of Au-CAAKA and Au-CAAKA-FITC.

Au nanoparticles (1.5 nm AuNP) were synthesized initially as TPP-Au (1.5 nm) in toluene (TPP is triphenylphosphine) [100] and ligand exchanged with CAAKA to produce water soluble CAAKA-Au (1.5 nm) following standard literature methods. The attachment of CAAKA occurs through the N-terminus Cys (C). The size of the Au was confirmed by TEM (Figure 3.2 A), and UV-Vis, noting the absence of a plasmon resonance at 520 nm (Figure 3.2 B), consistent with a Au nanometal below 2 nm in size. For molecular beacon studies, CAAKA was labeled with fluorescein-isothiocyanate (Sigma) through the free-amine of Lys (K) according to manufacturer instructions and purified by HPLC (C18-RP) before being exchanged on the AuNP.

Molecular Beacon Characterization of FGF1 assembly onto AuNP surface.

Appending the FGF1 (or FGF1 – heparin) onto the AuNP is carried out in buffered conditions in 50 mM sodium phosphate, 10 mM $(\text{NH}_4)_2\text{SO}_4$, 100 mM NaCl,

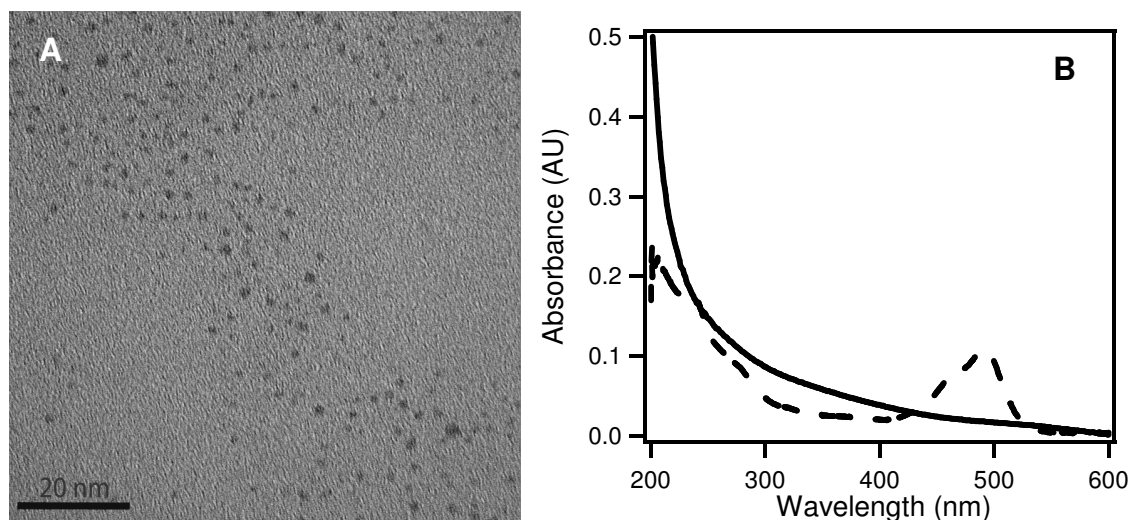


Figure 3.2: A) TEM of 1.5 nm AuNP and B) Absorbance spectroscopy of AuNP with CAAKA ligand (solid) and AuNP with CAAKA-FITC (dash), noting the FITC absorbance ($\lambda_{\text{max}} = 495 \text{ nm}$)

pH=7.5 (Buffer A) in a 1:1 protein to AuNP ratio. FGF1 and FGF1-heparin ligand exchange on the 1.5 nm AuNP was measured for 18 h at 7min intervals using a molecular beacon NSET approach [64] by tracking the de-quenching of the CAAKA-FITC after release from the AuNP. The fluorescence spectra were collected from 500-600 nm in triplicate on a Cary Eclipse (Varian) in a 100 μ l cell at 25°C in Buffer A using a 1cm pathlength and excitation wavelength of 450 nm. The rate of CAAKA-FITC release from the AuNP surface upon FGF1 and FGF1-heparin is tracked by the onset of FITC emission ($\lambda_{em} = 520$ nm) and plotted as a function of time in Figure 3.

Time Dependent Structural Changes in FGF1 by CD Spectroscopy.

Far-UV circular dichroism (CD) spectra were collected between 195-260 nm with 0.5 nm steps and 1 sec signal averaging on an AVIV 202 CD spectrometer at 25°C in Buffer A using a 1 cm pathlength. Each sample, including the buffer, was measured in triplicate and averaged before subtraction. Sample concentrations were typically 5 μ M FGF and/or 5 μ M Au-CAAKA in Buffer A. The CD spectra were fit using CDPro software [101].

2-D HSQC NMR Analysis of Protein Structural Perturbations.

2D- ^1H , ^{15}N HSQC experiments were performed on a uniformly labeled ^{15}N -FGF1 on a Varian Inova spectrometer operating at 11.74 T (Varian Inc., Palo Alto, CA). Protein sample concentrations were typically 200 μ M in 100 mM phosphate, 200 mM $(\text{NH}_4)_2\text{SO}_4$, 100 mM NaCl at pH=6.0 (Buffer B). HSQC spectra were collected over 8333 Hz (1500 Hz) and digitized by 1024 (220) complex points in the ^1H (^{15}N) dimensions in 16 scans per increment for a total data collection time of ~90 min. Data collection for each HSQC spectrum was initialized at 0, 5, and 18 h following addition of the AuNP-CAAKA. Data processing and peak assignment was performed using NMR-Pipe and analyzed using NMR-View. Changes in resonance position ($\Delta\delta$) upon addition of AuNP-CAAKA were quantified as $\Delta\delta = \sqrt{(\Delta H)^2 + (\Delta N^2 / 5)}$ [94].

3.3 Results

The mechanism of the assembly of FGF1 onto a AuNP surface (Figure 3.1) will dictate the functionality of the FGF1 bio-nano construct. The highly positive heparin binding domain may interact strongly with the AuNP, thus blocking the heparin site which is critical for FGF1 function. Alternatively, the His-tag may dominate the assembly placing

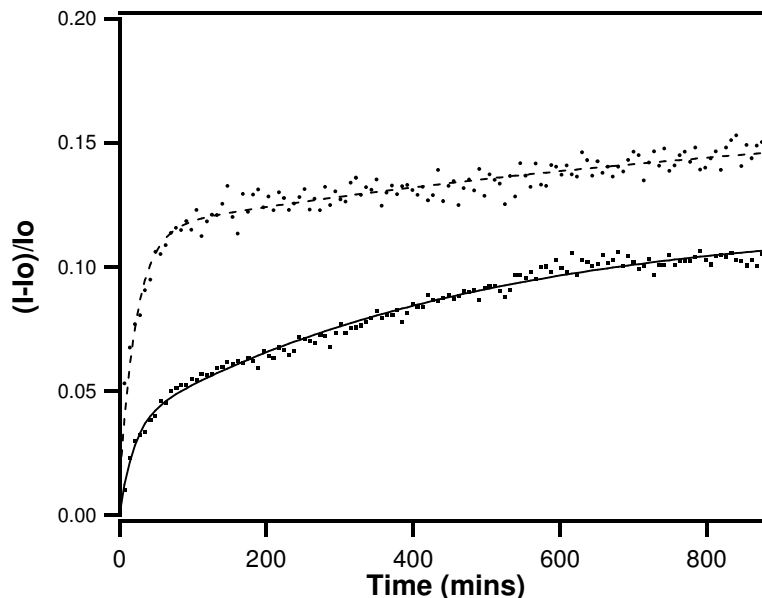


Figure 3.3: FGF1 and FGF1-heparin time course plot with AuCAAKA-FITC, Avg. FITC emission change (510-520nm, 450exc). Both FGF1 (solid) and FGF1-heparin (dash) show nearly identical binding rates, with the only difference being that the FGF1-heparin complex appears to displace more CAAKA-FITC from the surface.

the AuNP in the opposite side of the heparin binding pocket, which would be ideal for maintaining the protein function for this protein-AuNP conjugate. Such site selectivity for labeling would open the use of a wide range of recombinant proteins for potential bio-medical technologies.

The use of Au-CAAKA, which has a zwitterionic character, is expected to minimize conjugate formation due to reduced electrostatic interactions, therefore allowing the His₆-tag to form an encounter complex via N ϵ coordination of the imidazole groups as in the model peptide discussed in Chapter 2. The addition of FGF1 (or FGF1-heparin) to AuNP (1:1 mole ratio) that is passivated by a FITC labeled peptide

sequence (CAAKA-FITC) leads to rapid release of the CAAKA-FITC from the AuNP surface and the subsequent re- appearance of a FITC fluorescence signature at the FITC peak emission wavelength ($\lambda_{em} = 520$ nm). In Figure 3.3, the molecular beacon exhibits a bi-exponential response for FGF1 and for FGF1-heparin over the 15 h of the experiment. The total fluorescence intensity recovery over the full 15 h time course experiment is approximately 9% for FGF1, whereas the FGF1-Hep exhibits a greater FITC fluorescence recovery, 14% relative to free peptide.

	<i>Fast Phase</i>		<i>Slow Phase</i>	
	Rate (min ⁻¹)	Amplitude (%)	Rate (min ⁻¹)	Amplitude (%)
FGF1	0.0532 (0.0080)	23 (2.2)	0.0022 (0.0002)	77 (1.3)
FGF1-heparin	0.0446 (0.0036)	67 (2.6)	0.0009 (0.0005)	33 (1.1)

Table 3.1: FITC Fluorescence recovery upon addition of FGF1 or FGF1-heparin to AuNP-CAAKAFITC

The fluorescence curves were fitted to a series of functions with increasing exponentials. Fitting to a single exponential resulted in large χ^2 values, which were significantly reduced in a bi-exponential fit; fitting to a tri-exponential function did not significantly improve the fit according to the F-statistic. Table 1 shows the rates and amplitudes from a bi-exponential fit of both data sets. The initial rate of CAAKA-FITC release for FGF1-heparin and FGF1 are similar, although the amplitude is larger for FGF1-heparin addition than for FGF1. The largest changes occur in the first 180 mins (Total Change: 60% for FGF1 and 90% for FGF1-heparin). The appearance of bimodal dynamics implies the displacement of CAAKA-FITC from the AuNP surface is influenced by the different exchange sites on the AuNP surface or a two-step release process on the AuNP surface in time; the protein may effectively sample the AuNP surface and evolve to the lowest energy binding motif. The drastic alteration of the kinetic profile (increased short time dynamic response compared to FGF1) when FGF1-heparin is used suggests that FGF1-heparin has a larger footprint thereby displacing a greater number of ligands rapidly or the FGF1-heparin limits the number of possible

random interactions between protein and AuNP since the heparin binding pocket is already occupied (Figure 3.1).

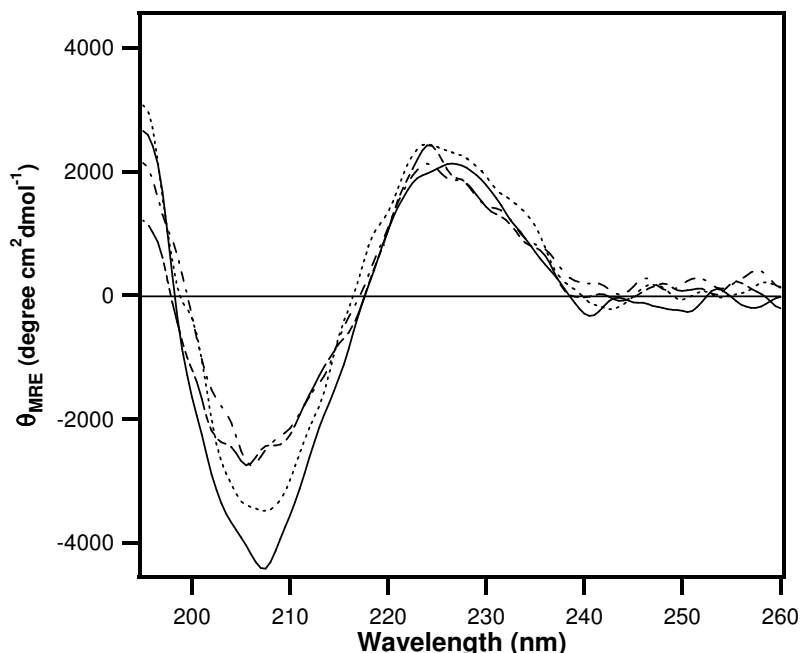


Figure 3.4: Far-UV CD of FGF1 (—) and changes at 15 min (····), 6h (----), and 24h (----) following the addition of AuCAAKA to the FGF1 solution.

Time Dependent Reconstruction of FGF1 on the AuNP surface.

The bimodal kinetics for loss of CAAKA-FITC from the AuNP surface strongly support a model where initial binding is followed by sampling of the AuNP surface by FGF1 to minimize the total energetics of the assembly. Evidence of structural evolution of FGF1 upon interaction with the AuNP surface can be tracked by analyzing the changes in the structural elements (β -sheet, β -turn, and random coil) of FGF1 protein interacting with the AuNP surface.

Based on crystal structures for FGF1 and its mutant sym6 $\delta\delta$, the primary structural elements consist of β -turns and β -sheets, with little to no α -helical character. In the FGF1 CD spectra, protein β -sheet character which normally exhibits a negative maximum at 216 nm is not observed, and therefore changes in the β -sheet secondary structure is interpreted by the changes in molar ellipticity (θ_{MRE}) at 207 nm, the negative

maximum, with a more detailed analysis of secondary structure elements using CDPro software.

In Figure 3.4, the CD spectra of FGF1 recorded at 0, 6, and 24 h shows time dependent changes. FGF1-heparin was not analyzed by CD spectroscopy. In the CD spectra the most significant time dependent changes occur at < 200 nm (β -sheet) and 207 nm following the mixing of the AuNP and FGF1. Initial Au addition (0 h) results in a 10% loss in the Molar Ellipticity (θ_{MRE}) at 207nm with further loss up to 6h. Changes in overall β -turn and β -sheet character for FGF1 upon binding to Au can be quantified by analyzing the θ_{MRE} for each sample using CDPro databases [101]. The overall change in FGF1 secondary structure in the presence of the AuNP is 40% θ_{MRE} at 207 nm, indicative of changes in the β -sheet character of the protein. No changes at 230 nm (random coil) are observed over the time regime of the study suggesting no random coil effects upon association with the AuNP. The CD data (using CDPro) implies an initial change in the β -sheet, followed by a slower change in β -turn. The changes in the CD spectra can be accounted for by a 10% gain in β -sheet character and a 7% loss in β -turn character for FGF1 following assembly onto the AuNP surface ($t = 24$ h). The CD results on FGF1 following coordination to the AuNP surface provides supporting evidence of structural evolution of the protein occurring over the experimental time regime as observed in the molecular beacon assay.

NMR Analysis of Protein Backbone.

HSQC 2-D ^1H , ^{15}N NMR provides a fingerprint of the protein backbone amides (less proline and the N-terminal residue) to understand changes in backbone chemical shift frequencies upon binding to the AuNP. The HSQC provides information about the backbone changes for individual residues, given the dispersity of each peak (minimal peak overlap) in the spectrum. Changes in both chemical shift and intensity can be observed depending on the environment of the backbone functional groups, and the potential contribution from changes in T_2 arising from restricted motional dynamics, which would be expected for a protein binding at a AuNP surface [56, 102].

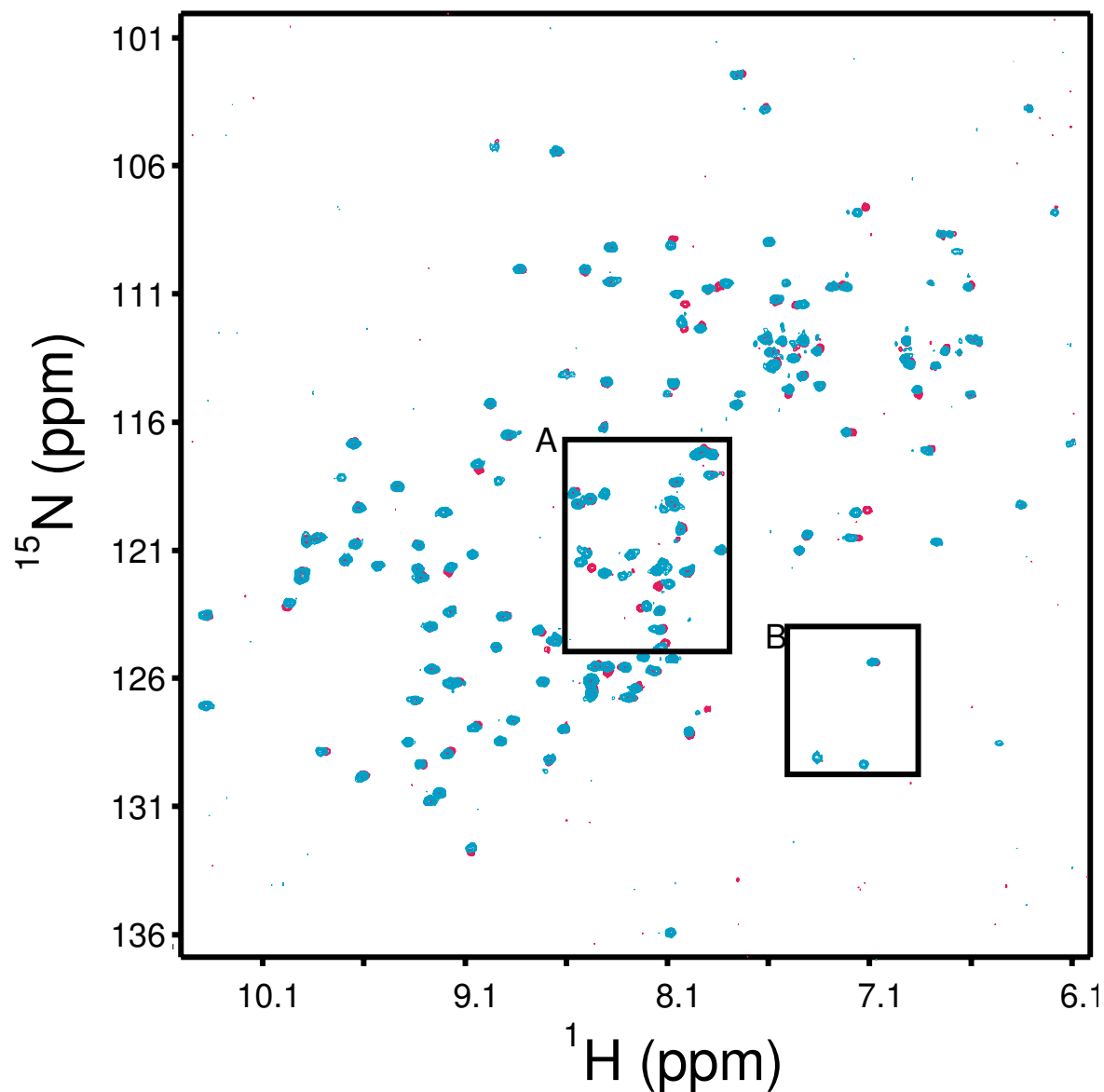


Figure 3.5: $^1\text{H} - ^{15}\text{N}$ HSQC NMR spectrum of FGF1 (cyan) and FGF1-AuNP (magenta) at 18 h. Two regions of interest are highlighted: A) a representative region of affected resonances showing intensity loss, frequency shifts, and no change, and B) the His-tag region.

The change in the FGF1 upon binding heparin (FGF1-heparin) is probed using HSQC. The HSQC spectra, as well as $\Delta\delta$ plot, and a model for binding interactions for FGF1 versus FGF1-Au is shown in Figure 3.5, 3.6 while a portion of the FGF1-Au, and the FGF1-heparin-Au is shown in Figure 3.9 A. The HSQC spectra are averaged over 90 min of collection time.

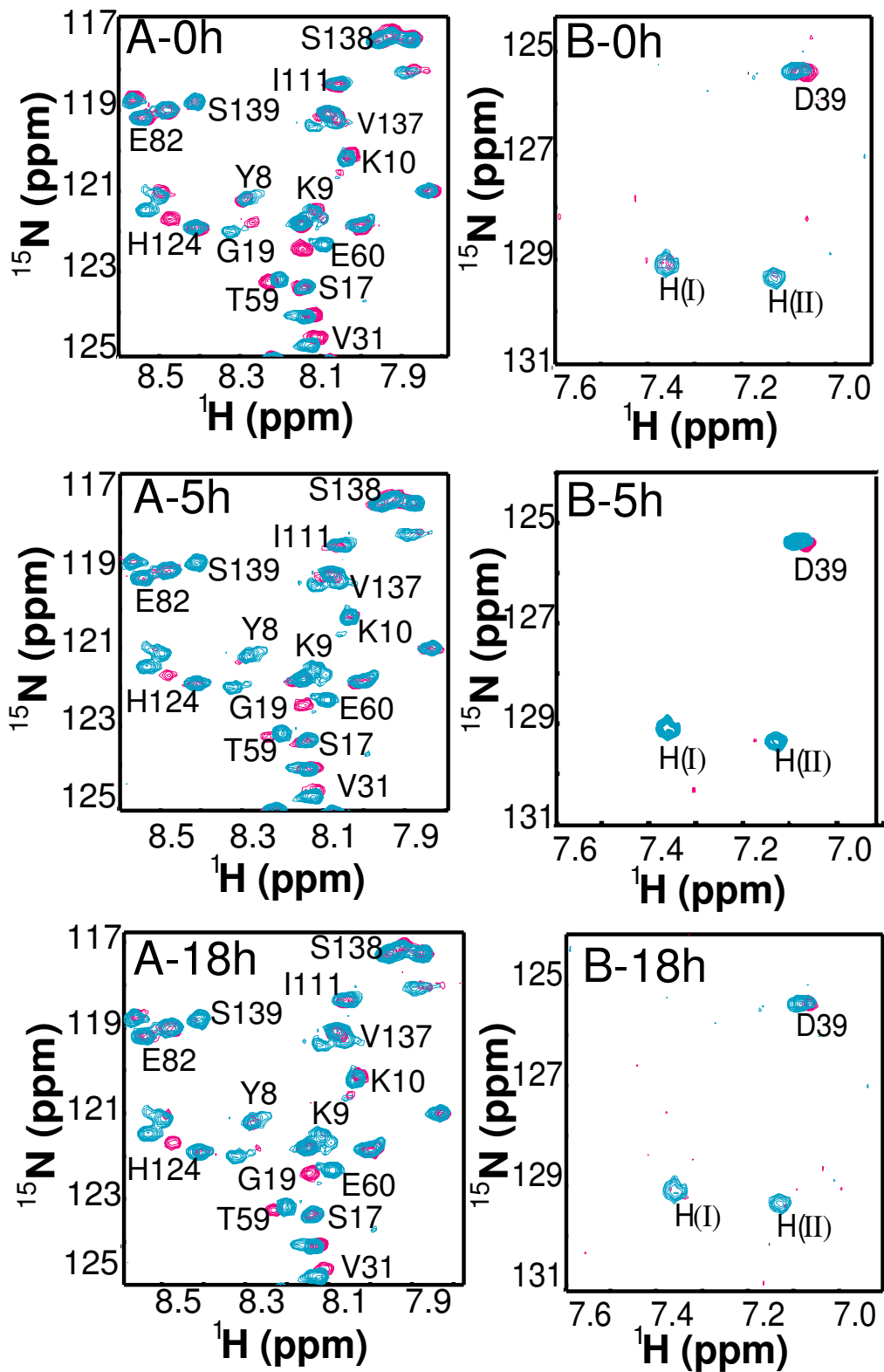


Figure 3.6: Expanded HSQC spectra for region A and region B at 0, 5, and 18 h after Au addition for FGF1 (cyan) and FGF1-AuNP (magenta).

Figure 3.5 compares the full spectrum for the HSQC of FGF1 alone (cyan) and the FGF1-Au (magenta) complex at 18 h. The time dependent changes of select regions are shown in Figure 3.6 (A and B at 0, 5, 18 h). Changes in the 2-D spectrum reveal the major changes in the NMR occur primarily for resonance in the 7.8 – 8.6 ppm ^1H / 117-125 ppm ^{15}N (Figure 3.6 A; 0, 5, 18 h), and for the range 7.1-7.5 ppm ^1H / 124-131 ppm ^{15}N (Figure 3.6 B; 0, 5, 18 h). The largest changes initially in the resonances assigned to the histidine tag and to resonances near the His tag on the surface of the protein. At longer times, there are peak losses or perturbations of surface loop residues, which are known to have intrinsic flexibility. The most significant changes occur for the histidine tail residues (designated His(I), His(II)), as well as the solvent exposed β -turn residues including Gly19, Gln43, Glu60, Glu81, and His124, and two C-terminal residues Val137 and Ser139. The changes in the His amino acids are reflected in the histidine backbone residues between 7.1 – 7.4 ppm (^1H). Immediately upon addition of the protein to the AuNP (Figure 3.6 B-0 h), the resonance at 7.12 ppm disappears completely while the second Histidine-tag resonance at 7.35 ppm shows reduced intensity. At time points greater than 5h, complete loss of both residues is observed in the experimental data (Figure 3.6 B-5h, B-18 h). The loss of the His-tag peaks in the NMR provides evidence of a FGF1-Au interaction or His-tag interaction with the FGF1 surface. The His-tag peak loss is expected since there is a change in the motional dynamics (change in T_2) when bound to the surface of the Au, indicative of a direct, covalent interaction. Similar peak loss associated with motional dynamics was reported for tri-alkyl phosphines bound to the surface of 1.5nm Au [102].

In Figure 3.6 B-0 h, E60, H124, and G19 show the largest chemical shift difference between native and bound form. Figure 3.6 B-5 h shows identical changes in the residues impacted at 0 h (Figure 3.6 B-0 h). In addition, the peak for residue S139 is lost in Figure 3.6 A-5 h. Figure 3.6 A-18 h shows no further changes for any of the residues in this backbone region.

A more quantitative method to examine the global changes in the FGF1 upon binding to the surface of the AuNP is to project the NMR data as a $\Delta\delta$ plot. The $\Delta\delta$ plot relates the magnitude of the chemical shift differences between the ^1H and ^{15}N resonances, as determined by the equation, $\Delta\delta = \sqrt{\Delta H^2 + (\Delta N^2 / 5)}$. In Figure 3.7, the

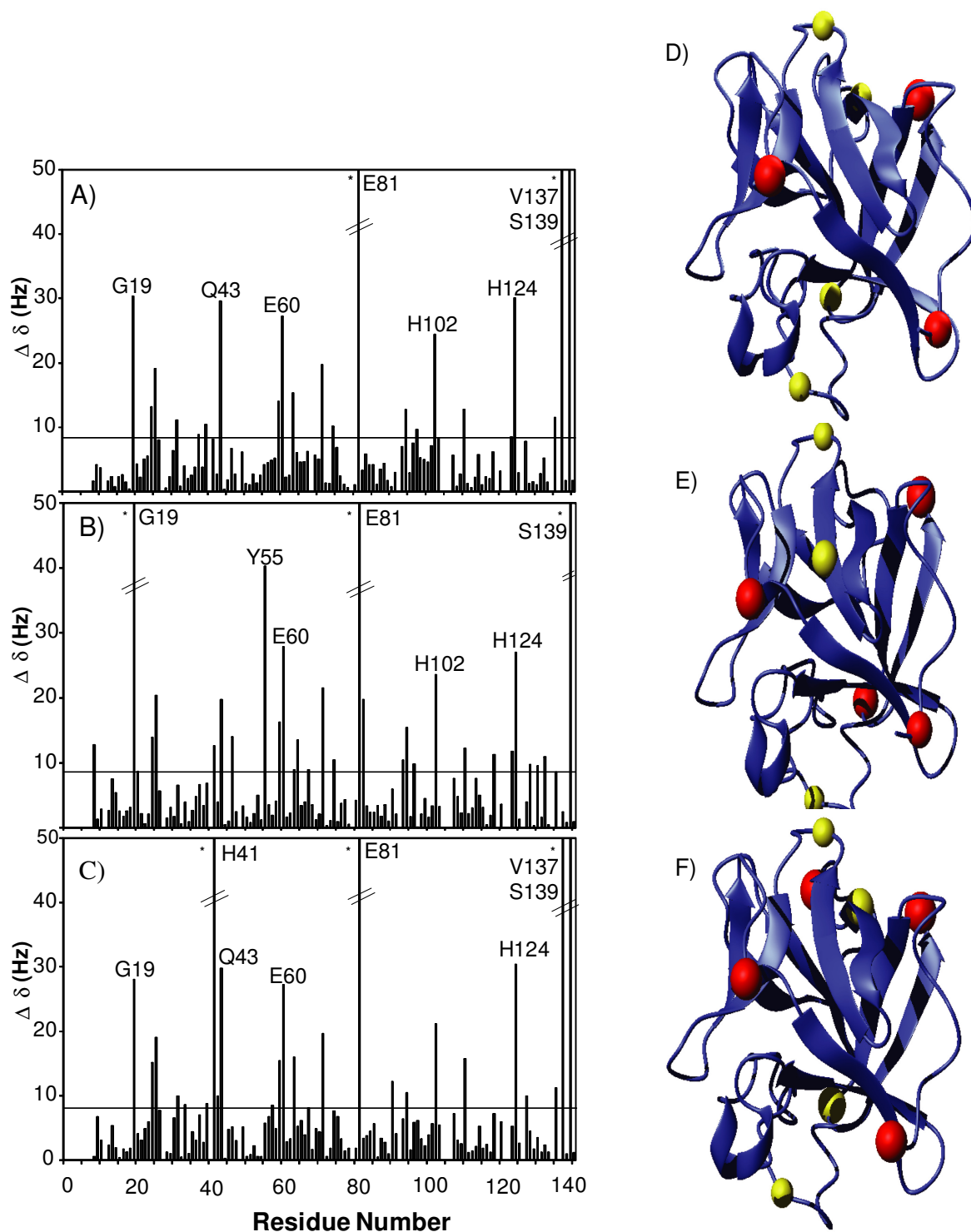


Figure 3.7: $\Delta\delta$ plots showing and corresponding FGF1 crystal structure (PDB ID: 1RG8 indicating changes in the FGF1 amide backbone chemical shift frequencies and complete peak losses (*) at A) 0 h, B) 5 h, and C) 18 h after AuNP addition. The solid black line indicates the digital resolution in the measurements (8.3 Hz). In the structural models of FGF1 at D) 0 h, E) 5 h, and F) 18 h, the large (red balls, >50 Hz) chemical shift / peak intensity loss and small (yellow balls, 25 – 50 Hz) are highlighted in the crystal structure.

$\Delta\delta$ plots for $t=0$ h (Figure 3.7 A), $t=5$ h (Figure 3.7 B), and $t=18$ h (Figure 3.7 C) are shown. Residues that show a $\Delta\delta \geq 25$ Hz. (digital resolution = 8.3 Hz.) are considered significant perturbations of the backbone. Using the $\Delta\delta$ plot, the amino acid residues that exhibit large changes (> 50 Hz) upon AuNP binding are labeled with red balls, while smaller changes (25 – 50 Hz.) are depicted with yellow balls. It is clear that the His residues are impacted immediately upon AuNP addition, while the C-terminal region exhibit significant time dependent changes over the entire experimental time regime. Importantly, the heparin binding pocket on the FGF1 remains largely unaffected by the AuNP binding, although the E81 residue (a surface residue in close spatial proximity to the His₆ region) is impacted over all time points. In addition, the AuNP binding significantly impacts the β -turn regions, with no impact noted for the β -sheet residues in the structure.

Although the perturbations are localized in the His-tag region and no significant perturbations are observed in the heparin binding pocket, the induced motional dynamic contributions in the protein may potentially impact the heparin binding affinity, a critical

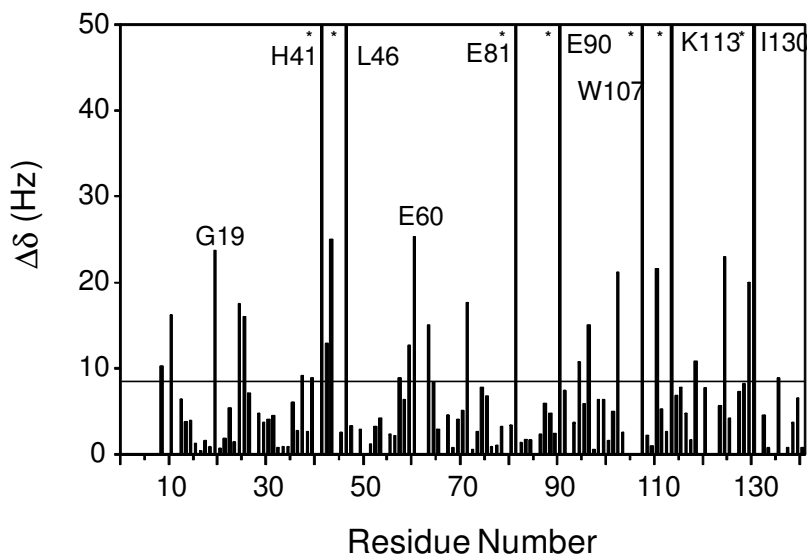


Figure 3.8: $\Delta\delta$ plot of FGF1 and FGF1-heparin at $t = 0$ h. The solid black line at 8.3 Hz indicates the digital resolution of the measurement. Residues that show the greatest resonance / intensity difference are labeled as shown.

component for FGF1 activity (NMR studies of FGF1 and heparin derivatives report

chemical shift changes for residues outside the heparin binding pocket) [94]. To assess the impact on the heparin binding pocket a pre-bound heparin-FGF1 complex was also analyzed by HSQC. Heparin was pre-incubated with the FGF1 before incubation to minimize extraneous electrostatic interactions.

FGF1-heparin NMR studies report that residues with largest chemical shift differences in FGF1-hexasaccharide complex are N18, H41, L73, H102, G112, G115, K118, G120, H124, Y135, and I130 with K118, G120, H124, and I130 showing the largest chemical shift.[94] A second NMR study by showed that S17, G20, H21, L74, E91, N92, K113, G110-G120, and R122-A129 were the most shifted residues upon formation of FGF-hexasaccharide [92]. This mutant from of FGF1 (sym6 $\delta\delta$) contains a number of deletions in the heparin binding pocket and has been shown to have a

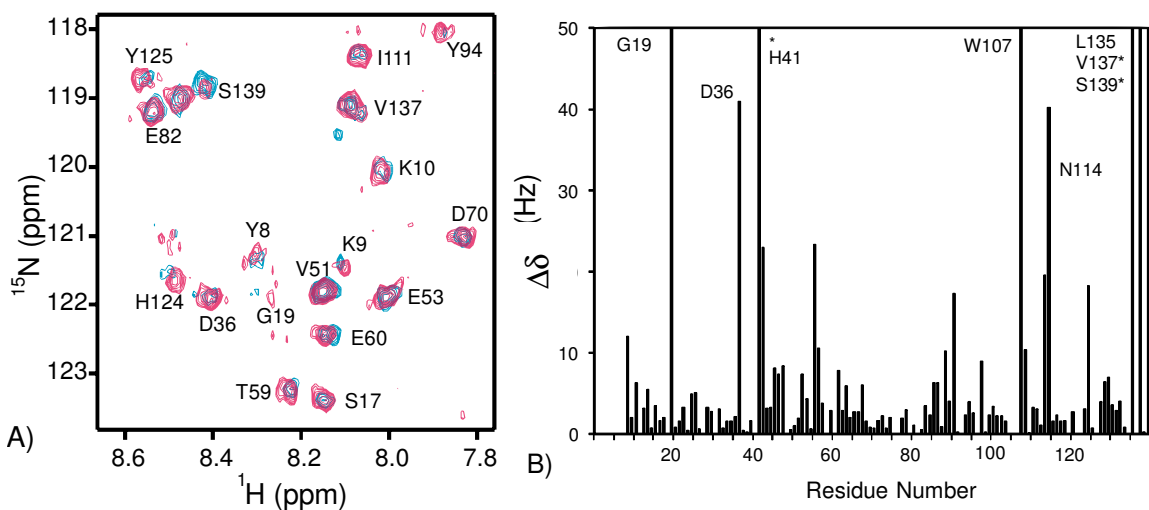


Figure 3.9: A) HSQC ($^1\text{H} - ^{15}\text{N}$) showing a representative region of observed changes at 18 h with FGF1-heparin (cyan) and FGF1-heparin-AuNP (magenta). Resonance assignments are listed near the corresponding peaks. B) $\Delta\delta$ of FGF1-heparin and FGF1-heparin-AuNP predicts showing resonance frequency shifts and absent peaks (*) for all peaks affected by the AuNP binding.

weaker binding affinity (higher K_d) than the wild-type FGF1 [103]. A better comparison of heparin function for this mutant is to examine the residues that are directly affected by heparin in a HSQC and $\Delta\delta$ plot of FGF1-FGF1-heparin (Figure 3.8). The residues in

FGF1 (sym6 $\delta\delta$) that are most affected by heparin are H41, L46, E81, E90, W107, K113, I130.

Figure 3.9 displays a selected area of the HSQC ^1H - ^{15}N NMR spectra for FGF1-Au, and FGF1-heparin-Au at 18h. Figure 3.8A displays an overlay of a representative region of the full HSQC of FGF1-heparin-Au (cyan), and FGF1-Au (magenta) at 18h. The residues that show complete loss of intensity are H(I), H41, V137, and S139, with G19, D36, W107, L135, and N114 showing large chemical shift differences as shown in Figure 3.9 B. Many of the residues effected by heparin binding initial at t=0 with FGF and again at 18 h in the presence of Au are identical in both experiments, H41, W107, and C-terminal residues.

One important note is that the absence of substantial differences in the $\Delta\delta$ between the FGF1-Au and FGF1-heparin-Au suggests that no major differences for heparin binding are noted with the Au. If the heparin were to release from the FGF1 upon binding to the AuNP, we would expect a large number of chemical shift differences to occur. Though not direct evidence, it is likely that the FGF1-heparin remains stable in time with AuNP present.

3.4 Conclusions

In Chapter 2, His₆ peptides were shown to bind directly to a AuNP through the N ϵ of the imidazole side chain of Histidine residues. The experimental data in Chapter 3 demonstrates that a recombinant His-tag FGF1 protein has been successfully attached to a 1.5 nm Au nanoparticle through direct binding of the His₆ tag to the Au surface. A covalent attachment to the AuNP is expected since the previous results for His₆ peptides have shown direct His binding to a AuNP through the N ϵ . The covalent attachment of His-tag proteins to Au nanoparticles results in minimal loss in secondary structure and no loss in function for the FGF1. The binding kinetics of FGF1-Au complex is slow, requiring almost 6 hours for complete stabilization of the protein-nano conjugate while the FGF1-Hep-AuNP achieves a stable assembly in 2 hours.

The loss of His-tag resonances in the presence of AuNP is explained by the enhanced relaxation caused by the Au atoms or by intermediate time-scale chemical

exchange. Alternatively, the loss of His-tag resonances may be due to kinetic exchange of the FGF1 at the AuNP surface. The resonance frequency changes seen in FGF1 indicate a change in the chemical / magnetic environment without changes in relaxation. These types of changes typically are interpreted to indicate structural change, although the exact change cannot be determined from the $\Delta\delta$ value.

Based on the experimental results for FGF1 and FGF1-heparin assembled onto the AuNP surface, the most likely binding motif is shown in Figure 3.1 A. The initial rapid release of the CAAKA-FITC (Figure 2) corresponds to the His-tag binding to readily accessible vertices and edges of the AuNP [57, 62], followed by slow displacement of CAAKA-FITC due to steric interactions with the FGF protein as it interacts with the Au surface. The FGF1-Hep complex may provide a more accessible His-tag, which results in a faster initial binding rate Table 3.1 and a diminished slow rate. This model for the differences in dynamics for assembly between FGF1 and FGF1-heparin supports an evolving AuNP surface interaction resulting in the bimodal CAAKA-FITC release dynamics.

It is unclear whether C-terminal (Figure 3.1 C) and β -turn chemical shifts through the extent of the experiment are caused by direct AuNP interaction with these residues or due to motional dynamic changes [94] with AuNP binding to the His-tag region. Given the time-dependent change in these residues, it is likely that these residues are impacted through protein surface interaction with the AuNP until the final, selective His₆-tag binding is complete. No evidence of interactions at the heparin site (Figure 3.1 B) are observed in the time dependent experiments. FGF1 assembly onto the AuNP surface shows no loss of the function (heparin binding) and minimal changes in secondary structure according to HSQC results and CD spectroscopy results.

The ability to bind Au nanoparticles to His-tag proteins opens another interfacial bridge between biology and nanoscience. This structure / function study of FGF1-AuNP binding provides evidence of stable, direct protein-Au conjugation without loss of normal function. This study enables further use of AuNP with recombinant His-tag proteins for intracellular delivery, biophysical studies, sensing, imaging, and other nano-biomedical applications.

CHAPTER 4

DEVELOPMENT OF A BIMODAL MR CONTRAST AGENT FOR HIGH FIELD MRI

4.1 Introduction

Magnetic resonance imaging (MRI) has emerged as powerful clinical tool for diagnostics and eliminates the need for non-invasive imaging in soft tissue [104, 105]. MRI relies on the density and magnetic fields of protons in a tissue sample, which have varying relaxivity differences (T1 and T2 effects) depending on the microenvironment of the water protons. MRI allows for the greatest spatial resolution of all other common techniques such as CT-scans and X-ray, but lacks the sensitivity of PET scans that rely on radionuclei for increased sensitivity [105]. To combat the decreased sensitivity, MRI contrast agents (CA) are being developed, which influence the relaxivity rates of water protons in contact with these chemical agents.

Two current areas of CA development include Lanthanide-ion (i.e., Gd^{3+} , Eu^{3+} , Dy^{3+}) doped low molecular chelators (DOTA, DTPA) and superparamagnetic iron oxide nanoparticles (SPIO). Lanthanide chelate contrast agents such as FDA-approved Gd-DTPA agents serve as positive CA, and are touted because these molecular materials are easily cleared from the body by normal pathological processes [106]. The positive CA are characterized by brighter sections in the MR image caused by shortening of both the longitudinal relaxation (T1) and transverse relaxation (T2), but because T1 is larger than T2 the T1 image brightening effect is observed [105]. Current nanomaterial based MR contrast agents include the FDA-approved SPIO Feridex (Advanced Magnetix, Inc.), which is used as a blood pool MR contrast agent. These superparamagnetic materials are categorized as negative contrast agents because of the darker MR images they produce, due to the shorter transverse relaxation (T2) time differences of the water protons exchanging energy with the superparamagnetic material [105].

With continued development of emissive quantum dots in biological applications,

bimodal contrast agents that utilize cadmium based quantum dots are being developed for MR contrast. Bimodal MR contrast agents that couple metal chelators and fluorescent quantum dots allow for simultaneous MRI and optical tracking methods in cells and soft tissue. Quantum dots provide a photostable alternative to organic dye molecules, and can be color-tuned according to the size of the material. Quantum dots have broad excitation wavelength, large Stoke shifts, and narrow emission lines when compared to commercially available dyes [22]. The surface of the quantum dot provides a large surface area that can be functionalized with a number of ligands (Figure 4.1) for cell delivery (cell penetrating peptides), imaging (antibody-antigen receptor binding – Fab), and drug delivery (siRNA, linearized plasmid, DNA aptamers), and can easily incorporate a number of different ligands on the same surface for increased functionality [31, 107-112]. Developing a safe, non-toxic bimodal contrast agent (CA) with a high-field responsive paramagnetic ion for improved imaging constitutes the major goal of this work.

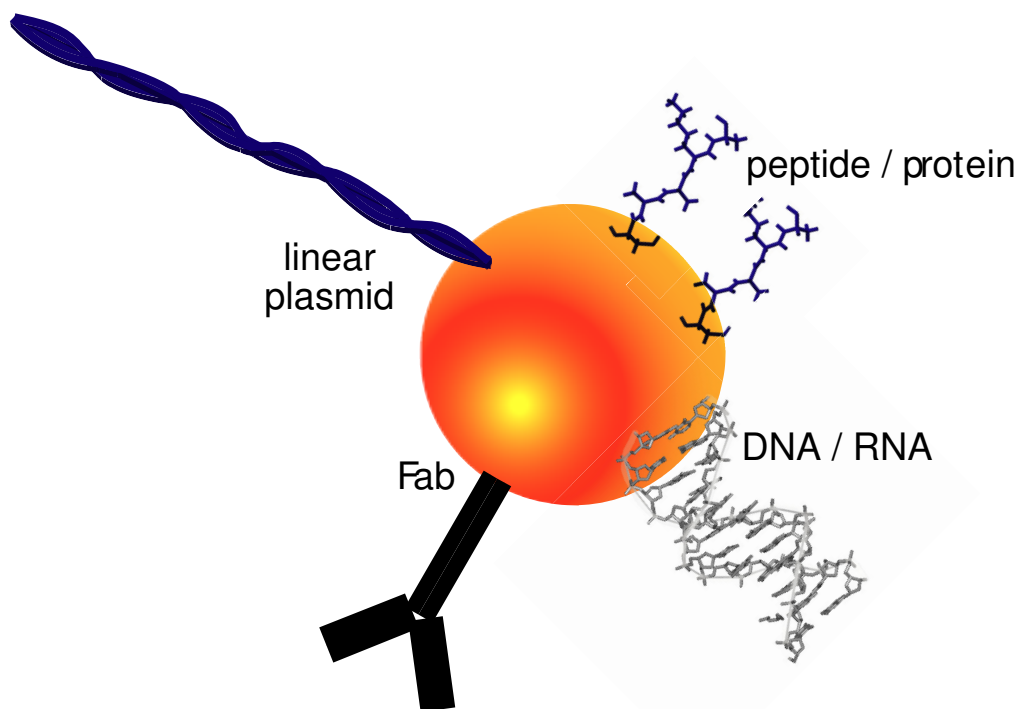


Figure 4.1: Model of possible ligand types that can be assembled on a quantum dot surface including linear plasmids, antibody fragments (Fab), short DNA or RNA strands, and peptides or proteins.

Quantum dots with paramagnetic surface ligands, usually appended with Gd-DTPA, [113-117] or direct nanocrystal doping with Mn^{2+} [118, 119] have been used successfully as CdSe-based biomodal CA. A major obstacle for biomodal contrast agents especially CdSe-based nanomaterials is biocompatibility (renal clearance), biological stability, and aqueous solubility [105]. Concerns about cadmium and selenium environmental and physiological toxicity [120] make InP based quantum dots a more bio- and environmentally compatible [121] material for bimodal contrast agent (CA) development. Although further nanotoxicology studies with InP quantum dots are warranted, much research has been done on InP bulk material that is routinely manufactured and used in semiconductor industries. Studies on bulk InP materials on laboratory animals has shown efficient fecal excretion of indium[122], but have noted pulmonary lesions from intratracheal administration at high doses and long-term exposure [123-125], and reproductive organ effects with severe, long-term exposure out to 2-years [126]. Of note, no subject deaths were reported for large dose or long duration exposure to InP in the aforementioned studies.

The choice of the semiconductor quantum dot, surface ligand charge, and hydrodynamic radius are vital for minimizing cell-disruptive responses and for complete clearance of quantum dots in live animals. Core-shell adducts of CdSe or CdS exhibit less toxic effects in intracellular [127-131] and live animal models [132] and is likely abrogated by the ZnS shell preventing penetration of O_2 to the core Cd^{2+} and decreased ROS formation caused by CdSe [133]. Maintaining a stable ligand shell in the reductive cellular environment is necessary to further attenuate toxicity of Cd-based nanomaterials[133]. Size, charge, and biodegradability of the quantum dot platform are critical to reduce immunogenic response (greatest with cationic particles), serum and cellular protein adsorption [134] (charge and hydrophobic interaction), and particle clearance (size and charge) [135]. Particle hydrodynamic radii ≤ 5.5 nm, zwitterionic surfaces, and biodegradable components, enhance renal clearance in a rat model of quantum dot fate and transport [136]. Quantum dots greater than 5 nm in size have exhibited lymph node retention [137] while maintaining fluorescent stability up to 2 years [132].

Intracellular delivery of the bimodal CA requires a pH stable macrocyclic lanthanide metal chelator with high metal affinity center. The lanthanide chelator 1,4,7,10-Tetraazacyclododecane-N,N',N'',N'''-tetraacetic acid (DOTA) coupled with Dy³⁺ ion provides a pH stable [138] improved CEST agent due to the exchangeable amide protons in proximity to the metal ion [139], compared to diethylene triamine pentaacetic acid (DTPA), which chelates through the acetate moieties. Dysprosium (Dy³⁺) is preferred to Gd³⁺ for high magnetic field contrast studies due to the slow water exchange rates and subsequent T2 effect [140, 141].

Many quantum dot and nanomaterial delivery mechanisms exist. For optimal intracellular particle delivery, a cell-penetrating peptide (cpp) and commercially available cationic liposomes are used for Chinese hamster ovary cell (CHO) transfections. A very common cpp is Tat (Transactivator of Transcription), which is derived from the Tat sequence of the HIV capsid protein. The use of Tat peptide (YGRKKRRQRRR) for gene delivery and cell transduction has increased due to its efficient cell translocation ability, and has been used for gene delivery and therapeutics [142-144] and nanoparticle delivery [28, 29, 31, 34-36, 145, 146]. Until recently it was believed that Tat peptide and commercial cationic liposomes, including Optifect and Lipofectamine2000 (Invitrogen), were both transfected by caveolin and clathrin-mediated endocytosis [147]. Tat peptide transduction was thought to be an energy independent pathway, but the transfection was determined to be temperature dependent with live cell experiments and not fixed cell experiments [142-144]. The endocytosis mechanism for Tat peptide has been determined to be macropinocytosis (Figure 4.2), or fluid phase endocytosis, which is an actin mediated pathway [142, 144, 147]. The macropinosomes are usually more a larger size, up to 5 μm in size, show more cytosol leaking than endosomes, and typically redistribute the contents to the cell surface [147].

Figure 4.2 shows the mechanism for cationic liposomes cell transfection that occurs through clathrin-mediated pathways. These liposomes are processed in the lysosome-endosomal pathway, forming early and late endosomes before fusing with lysosomes for degradation [147-151]. The two types of early endosomes that form are sorting

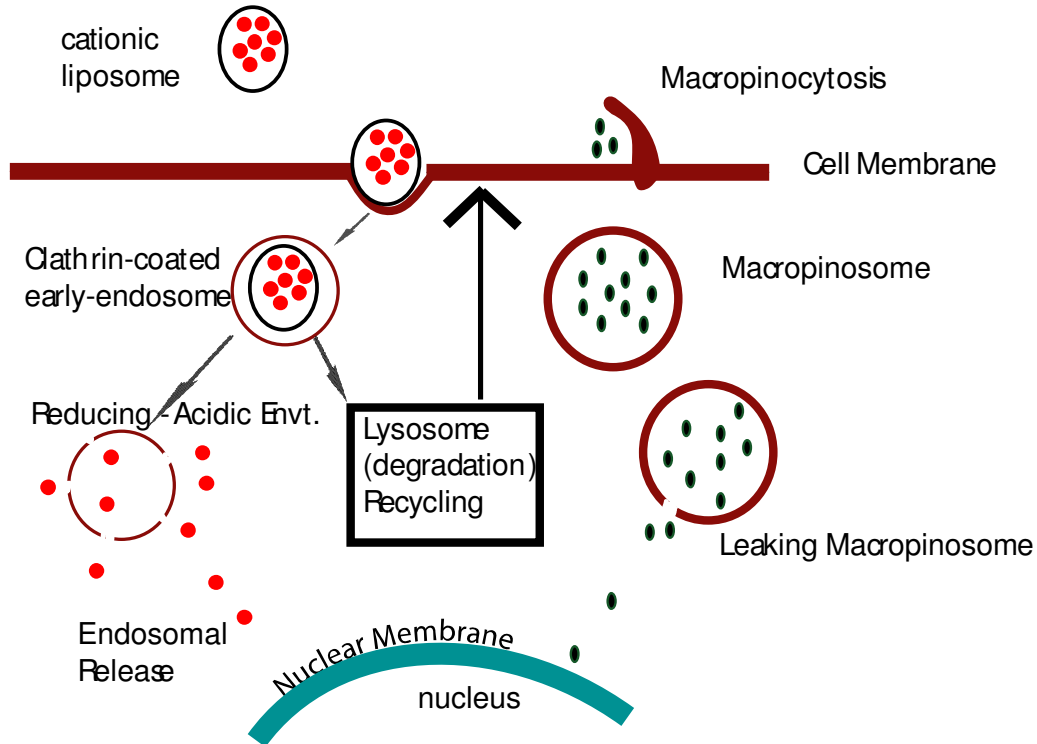


Figure 4.2: Mechanism of cationic liposome clathrin mediated endocytosis and macropinocytosis of Tat peptide for intracellular transfection. For clathrin-mediated endocytosis the cationic liposome fuses with the anionic cell membrane which initiates endocytosis. At this point, the early endosome can be processed through two paths: the package can be processed through the late endosome to the lysosome for degradation or the endosome can be disrupted and the cargo is released into the cytoplasm. In macropinocytosis with Tat peptide, the peptide interacts with the surface and is endocytosed using an actin mediated pathway. Macropinosomes are not processed in the endo-lysosomal pathway, and package release is mediated by macropinosome leaking.

endosomes or recycling endosomes that return the packaged material to the cell surface [149]. The most critical step for efficient cargo delivery is the early and late endosomal release prior to lysosome fusion, thereby permitting cytosol diffusion and nuclear membrane localization [147-151]. The cationic liposomes are thought to aid endosomal release because of the cationic surface interaction with the anionic clathrin lipid bilayer [149]. Finally, nuclear membrane and nuclear translocation (for gene delivery) become the limiting step. Cytosol diffusion to the nucleus has been shown to be dependent on DNA length, with short strands (~20 base pairs) able to circumvent molecular crowding issues in the cytosol and larger plasmid-sized DNA strands having much slower nuclear diffusion rates [149, 152]. The release of the CAAKA-DOTA-Dy

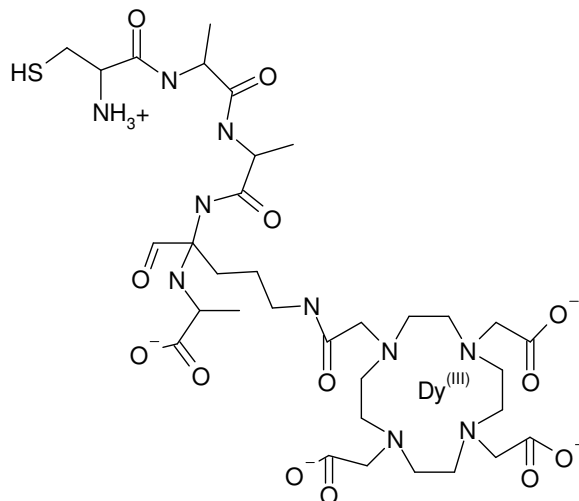


Figure 4.3: Molecular model representing CAAKA with DOTA-Dy appended through the N ϵ of the Lys side chain.

and CAAKATat-DOTA-Dy from the endosomes is necessary to improve T1 and T2 contrast because of the large pool of water available in the cytosol. Inefficient release would decrease the transverse relaxation effect expected from Dy³⁺ interactions as a chemical exchange saturation transfer effector on the cytosol water.

This study will show bimodal contrast in live CHO cells using the macrocyclic, metal chelator DOTA doped with Dy³⁺ ions appended to the surface of an InP/ZnS quantum dot using a peptide linker. Bimodal contrast of the live cells is successfully demonstrated with both InP/ZnS-CAAKA-DOTA-Dy and InP/ZnS-CAAKATat-DOTA-Dy by parallel imaging of cell samples optically by confocal microscopy and MR at 21.1T on a 900 MHz magnet.

4.2 Materials and Methods

CAAKA-DOTA-Dy or CAAKA-Tat-DOTA-Dy formation

The DOTA-Dy-CAAKA (Figure 4.3) and DOTA-Dy-CAAKATat (Tat = YGRKKRRQRRR) conjugates were prepared by the condensation reaction of the DOTA-Dy complex lysine (K) of CAAKA (Figure 4.3) or CAAKAYGRKKRRQRRR via a succinidyl ester. The DOTA-Dy complex is formed by mixing a 1:1 mole ratio of DyCl₃·xH₂O to DOTA (Strem) in MOPS buffer (pH=6.5) for 3 h at 80°C. The DOTA is

converted to the mono-succinimidyl ester by treatment of the Dy-DOTA complex by 1-ethyl-3-(3-dimethylaminopropyl) carbodiimide hydrochloride (EDC, 4:1 mole ratio relative to DOTA) for 10 mins. to convert one of the carboxylate functionalities to the o-acylisourea intermediate. Treatment with N-hydroxysulfosuccinimide (Sulfo-NHS) (1.2:1 mole ratio to EDC) for 1h produces the mono-functionalized succinimidyl ester of the DOTA-Dy complex. A 4:1 ratio of DOTA:EDC was used to ensure that only one carboxylate of the DOTA would be converted to a succinimidyl ester [153]. The CAAKA or CAAKAYGRKKRRRQRRR peptide was added in equimolar ratio (for single K labeling) to the original Dy-DOTA, mixed and incubated for 4h at room temperature, and the resultant complex was purified by HPLC (Jupiter-C18; Phenomenex) using a 5-20% linear gradient of 100% CH₃CN and lyophilized for later use (Figure 4.4).

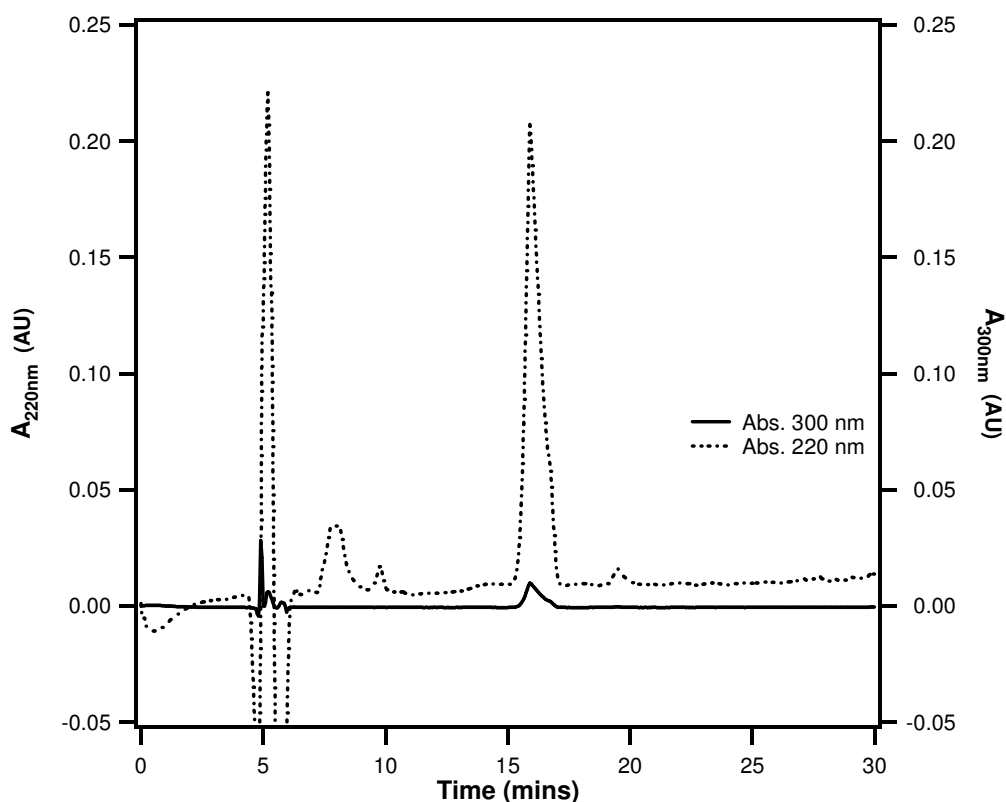


Figure 4.4: HPLC of CAAKA-DOTA-Dy that shows the unlabeled CAAKA (8.0 min.) starting material and the desired product CAAKA-DOTA-Dy (16 min.). The CAAKA-DOTA-Dy is identified by the weak absorbance at 300 nm, which is absent from the CAAKA peptide alone. The 300 nm absorbance is due to the Lanthanide macrocyclic complex (Dy-DOTA) absorbance.

InP-ZnS core-shell Nanocrystals

ZnS capped InP core-shell nanocrystals were prepared using a Microwave assisted lyothermal synthetic technique as described previously [154]. Briefly, stock solutions of In^{3+} in the form of indium palmitate (InPA) and P^{3-} in the form of TMS-phosphide in decane were combined in a 1:3 mole ratio in a microwave reactor. The nanocrystals were grown at 300W, 280°C for 15 mins. with “active cooling” applied in a modified CEM Discover system. The microwave generated InP nanocrystals are 3 nm in size and a passivated by palmitic acid. Formation of the core-shell is accomplished by shelling isolated InP by ZnS following lyothermal methods outlined in literature procedures. Briefly, the core-shell structure is prepared by dissolving the InP nanocrystals in a 1:2 (v/v) trioctylamine to dodecylamine solvent mixture heated to 250°C. The shell is formed by slow addition of a Zn:S solution generated by mixing $(\text{Me})_2\text{Zn}$, TMS-S in tetrabutylphospine. The core-shell ZnS/InP is isolated by treatment with toluene followed by MeOH precipitation.

CAAKA-DOTA-Dy and CAAKATat-DOTA-Dy passivated InP/ZnS

Formation of the CAAKA-DOTA-Dy (or CAAKATat-DOTA-Dy) passivated InP/ZnS is achieved by modification of a standard method [155]. Briefly, CAAKA-DOTA-Dy (1 mg) dissolved in 200 μL DMF (5 mg/mL peptide) was added to a solution composed of 2 mg sample of InP/ZnS dissolved in 2 mL CH_2Cl_2 :DMF (9:1, v/v). The sample was stirred for 1h and a solid pellet collected by centrifugation after washing with CH_2Cl_2 and DMF. The sample was dissolved in nanopure water and dialyzed (3000 MW cutoff) in 20 mM Phosphate buffer with 50 mM NaCl (PBS), pH=7 to remove residual solvent and peptide.

CHO cell transfection with InP/ZnS-CAAKA-DOTA-Dy

To achieve nanocrystal transfection, 50 μg of InP/Zns was incubated with 10 μL of Lipofectamine2000 transfecting agent (Invitrogen) for 20 mins prior to addition to the cell samples. CHO (Chinese Hamster Ovary-K1) cells grown in DMEM media supplemented with non-essential amino acids were plated in 10 cm^2 sample dish and transfected with the InP/ZnS-Lipofectamine at 90% confluence ($\sim 1.8 \times 10^6$ cells) following

the manufacturers suggested procedure. Samples were allowed to incubate for 24 h, washed with Tris-buffered saline (TBS), trypsinized with TrypLE (Invitrogen), and finally re-suspended in media. The MRI measurements were carried out on either a cell pellet or the CHO cells in agarose. Agarose samples were formed by mixing an equal volume of ~150,000 cells in media with a 2% Agarose sample (1% agarose final concn) and layered in a 10 mm borosilicated NMR tube with 1% agarose layers separating cell layers as shown in Figure 4.5. Setup of control samples (CAAKA-DOTA, CAAKA-DOTA-Dy, and InP/ZnS-CAAKA) was done using 50 μg of each sample as well as the identical protocol for cell transfection, isolation, and agarose suspension.

Dosing experiments with InP/ZnS-CAAKA-DOTA-Dy were performed following the same transfection, isolation, and agarose suspension protocol listed above except for varying amounts of InP/ZnS-CAAKA-DOTA-Dy was added to each separate cell sample dish: 0, 0.5, 5, 50, and 500 μg .

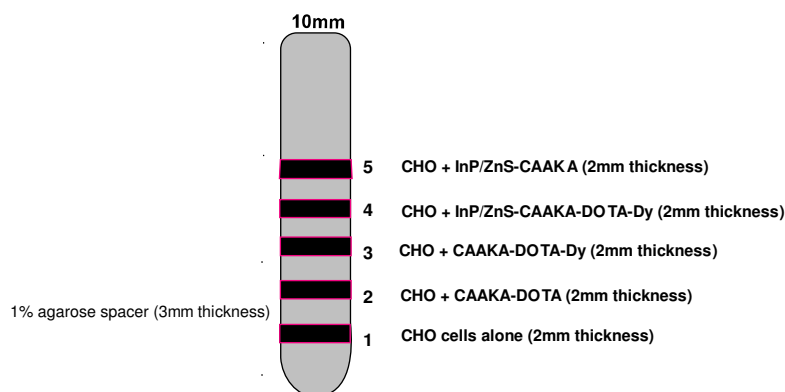


Figure 4.5: CHO cell layering setup in 10mm diameter borosilicate NMR tube for MR imaging. A 1% agarose gel is used for spacer layers between each 1% agarose layer containing CHO cells transfected with each unique sample.

InP/ZnS-CAAKATat-DOTA-Dy CHO cell transfection

For Tat-mediated cell transfection with InP/ZnS-CAAKATat-DOTA-Dy 50 μg of InP/Zns was added directly to 1.8×10^6 CHO cells (90% confluence) grown in DMEM media supplemented with non-essential amino acids were plated in 10 cm^2 sample.

Samples were allowed incubated for 24 h, washed with Tris-buffered saline (TBS), trypsinized with TrypLE, and finally re-suspended in media. The MRI measurements were carried out on either a cell pellet or the CHO cells in agarose. Agarose samples were formed by mixing an equal volume of ~150,000 cells in media with a 2% Agarose sample (1% agarose final concn).

MRI Imaging sample preparation with agarose tissue mimic

MR imaging was performed at 21.1 T ultra wide bore (UWB) vertical magnet constructed at the National High Magnetic Field Laboratory (NHMFL). A 10 mm Bruker RF birdcage resonant at 900 MHz was used for ^1H detection of the CHO cell – agarose layers. Slice thicknesses were 0.5 mm with 148 x 80 x 500 μm resolution in all samples. For the T1 measurements a 2D Spin Echo sequence was used in all measurements with an Echo Time (TE) of 7 ms and varying Repetition Times (TR) of 50, 150, 300, 750, 1500, 6000, and 15000 ms. The T2 measurements also used a 2D Spin Echo sequence with constant TR=5000 ms and variable TE times (10, 15, 20, 25, 35, 45, 65, 85, 100, 120 and 300 ms). Finally, T2* measurements used a 2D Gradient-Recalled Echo sequence with TR = 5000 ms and variable TE (3, 5, 7, 11, 13, 15, 17, 19, 21, 23, 33, 43, 63 and 83 ms).

4.3 Results

In Figure 4.3, a live cell image of the CHO cells 24 h post-transfection with Optifect and InP/ZnS-CAAKA-DOTA-Dy shows the fluorescent InP/ZnS quantum dot is within the cell membrane. The quantum dots are evenly distributed in most of the cells in the field of view and show some bright regions within the cell, which are likely endosomes. MR imaging of the InP/ZnS-CAAKA-DOTA-Dy in Figure 4.7 shows that the 4th layer (Figure 4.5) contains the InP/ZnS-CAAKA-DOTA-Dy and is the only layer that shows T2 contrast. There is no visible T2 contrast seen in any of the other control sample layers. The T2 value for each agarose-cell layer is given in Table 4.1. Layer 4 is the only layer that has a change in T2 value (76.6 msec) when compared with the agarose layer alone (104.3 msec). The T1 values remain unchanged for all the

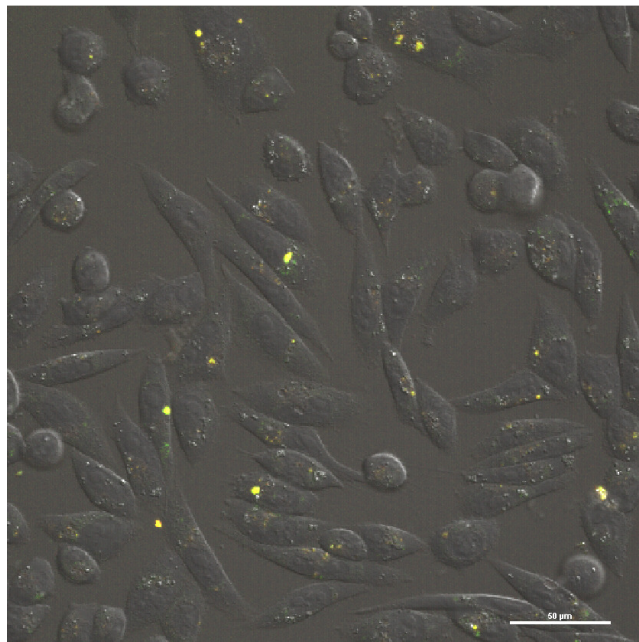


Figure 4.6: Brightfield DIC overlay with TRITC epifluorescence displaying the endocytosed InP/ZnS-CAAKA-DOTA-Dy in CHO cells.

samples. Figure 4.8 displays the difference in negative contrast (T2 effect) for varying doses of InP/ZnS-CAAKA-DOTA-Dy, while Table 4.2 reports the T1 and T2 values for each agarose-CHO layer in the dosing experiment. As expected, increasing the initial amount of InP/ZnS-CAAKA-DOTA-Dy delivered to the cell results in a substantially greater T2 value (Table 4.2) and more visible negative contrast (Figure 4.8). The maximum T2 value was achieved at 500 μg initial loading (52.1 msec), which is much lower than the 0 mg control sample (117.5 msec). A minor change in T1 time is noted, but visible positive contrast from the T1 difference was not noted for these samples.

In contrast to the InP/ZnS-CAAKA-DOTA-Dy, the InP/ZnS-CAAKATat-DOTA-Dy displays a noticeable T1 effect in solution (Figure 4.9) compared to InP/ZnS-CAAKA-DOTA-Dy. In Figure 4.8, a comparison of the CAAKATat-DOTA-Dy and InP/ZnS-CAAKATat-DOTA-Dy shows that appending the peptide-contrast agent conjugate to the surface of the InP/ZnS results in more visible T1 effect for both the agarose and solution sample under identical conditions. Addition of the the InP/ZnS-CAAKATat-DOTA-Dy to the CHO cells with and without Lipofectamine2000 transfecting agent results in no measurable difference in the T1 contrast between the samples and the controls (Figure

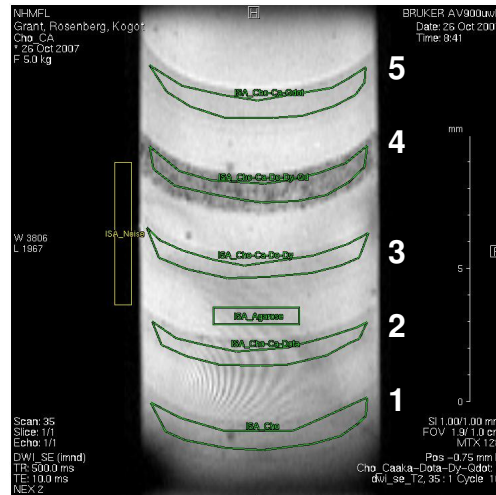


Figure 4.7: MR image of layers of CHO cells containing 1) CHO cells alone, 2) CHO cells + CAAKA-DOTA, 3) CHO cells + CAAKA-DOTA-Dy, 4) CHO cells + InP/ZnS-CAAKA-DOTA-Dy, and 5) CHO cells + InP/ZnS+CAAKA. The negative contrast seen in layer 4 indicates a T2 difference with the CHO cells transfected with InP/ZnS-CAAKA-DOTA-Dy. The cells are suspended in a 1% agarose gel to act as a tissue mimic. The space between each layer is also 1% agarose and is used for T2 measurements of agarose alone.

	T1 [msec]	T2 [msec]
5) CHO-CAAKA-Qdot	3036.0 ± 116.4	102.1 ± 14.2
4) CHO-CAAKA-DOTA-Dy-Qdot	2911.9 ± 121.2	76.6 ± 11.1
3) CHO-CAAKA-DOTA-Dy	2927.3 ± 141.1	101.3 ± 17.3
2) CHO-CAAKA-DOTA	3174.9 ± 224.1	108.2 ± 13.6
1) CHO	3627.9 ± 679.7	101.4 ± 17.8
Agarose	3012.1 ± 80.7	104.3 ± 8.2

Table 4.1: T1 and T2 measurements for samples in Figure 4. Minimal differences in T1 relaxation is observed across all samples. A difference in T2 is only noted for layer 4, InP/ZnS-CAAKA-DOTA-Dy.

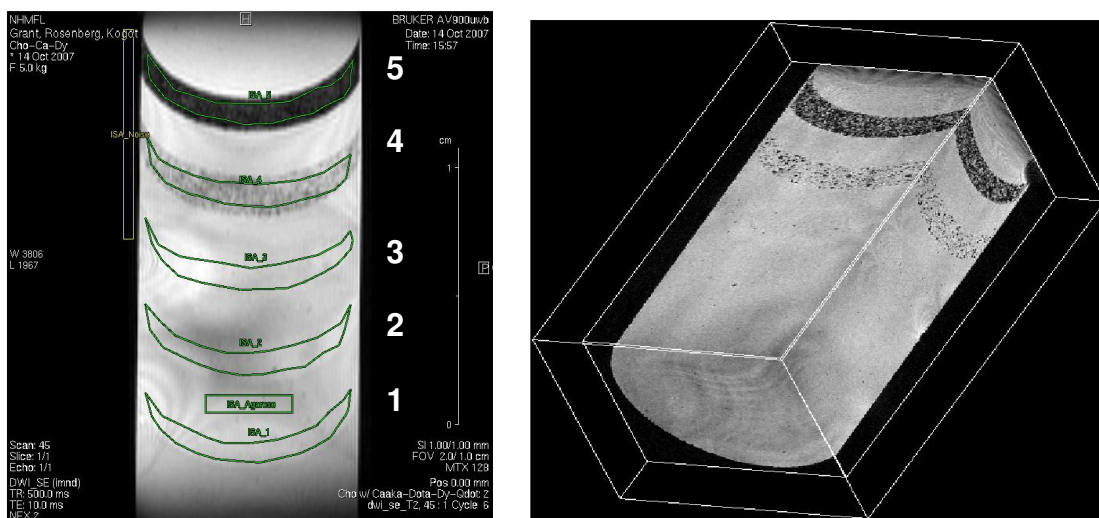


Figure 4.8: A) MR image and B) 3D Gradient Echo of InP/ZnS-CAAKA-DOTA-Dy transfected into CHO cells with Lipofectamine2000 using varying amounts of initial contrast agent at varying dose levels. 1) 0 µg, 2) 0.5 µg, 3) 5 µg, 4) 50 µg, and 5) 500 µg.

InP/ZnS-CAAKA-DOTA-Dy (µg)	T1 (msec)	T2 (msec)	T2 Linked	T2 Star
0	3373.8	117.5	116.1	37.9
0.5	3070.3	116.6	86.7	95.7
5	2965.6	107.0	110.1	64.6
50	2939.4	98.6	63.2	36.4
500	2924.8	52.1	21.4	7.2
Agarose	3207.1	102.1	105.2	71.0

Table 4.2: Calculated T1 and T2 values from dosing samples in Figure 4.6. There is little change in T1 with increasing dose, but T2 decreases with each increase in the total InP/ZnS-CAAKA-DOTA-Dy transfected in each cell sample.

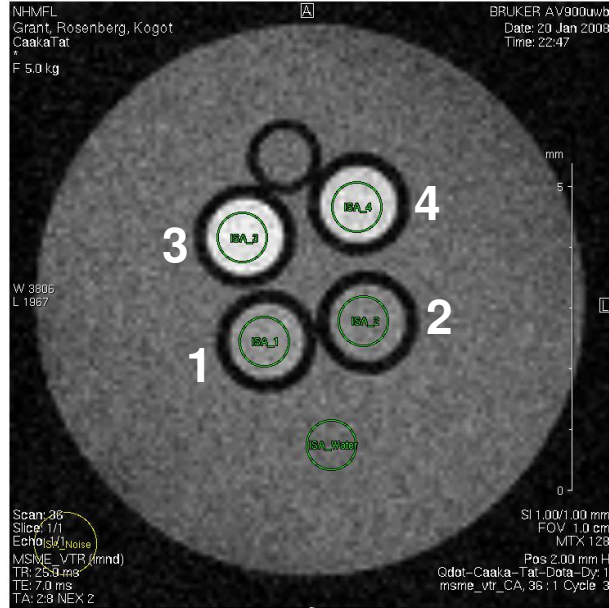


Figure 4.9: MR image at 900 MHz with 1) CAAKATat-Dota-Dy in H₂O, 2) CAAKATat-Dota-Dy in 1% Agarose, 3) InP/ZnS-CAAKATat-DOTA-Dy in H₂O, and 4) InP/ZnS-CAAKATat-DOTA-Dy in 1% Agarose. All samples are contained in a flame-sealed 1 mm (i.d.) borosilicate capillary tube and are surrounded by water to enhance the T1 difference between bulk water and water in exchange with the Dy-DOTA complex.

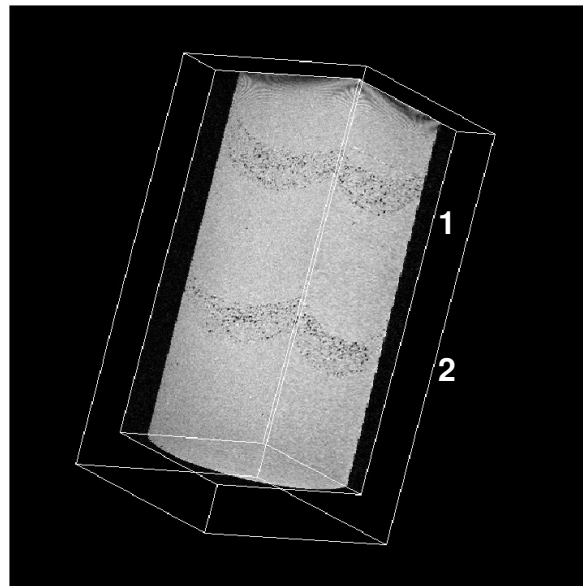


Figure 4.10: 3D Gradient Echo Image of InP/ZnS-CAAKATat-DOTA-Dy without Lipofectamine (1) and with Lipofectamine (2). No contrast difference is noted upon visual inspection.

Sample	T2 [ms]	T1 [ms]
InP/ZnS-CAAKATat-DOTA-Dy with Lipofectamine2000	<u>53.6</u>	2916.2
CHO cells alone	96.0	2882.1
InP/ZnS-CAAKATat-DOTA-Dy Alone	<u>52.6</u>	2909.9
Agarose	100.9	2946.3

Table 4.3: Tabulated results of InP/ZnS-CAAKATat-DOTA-Dy transfection with and without Lipofectamine2000 compared to CHO cells alone. The Lipofectamine2000 is not necessary for efficient transfection of the InP/ZnS-CAAKATat-DOTA-Dy material, and is most likely transfected solely with the Tat peptide on the surface.

4.10). A large T2 difference is noted with the InP/ZnS-CAAKATat-DOTA-Dy compared to the control (Table 4.3), although no difference in T2 was measured for the sample with and without transfecting agent.

4.4 Conclusion

The InP/ZnS-CAAKA-DOTA-Dy and InP/ZnS-CAAKATat-DOTA-Dy both perform well as bimodal contrast agents for obtaining MR and fluorescence microscopy measurements with CHO cell pellets and CHO cells suspended in an agarose tissue mimic. The observed T2 differences for the bimodal CA in cells when compared to control samples is most likely due to the large number of peptide-DOTA-Dy complexes (approximately 82 DOTA-Dy per InP by XRF) attached directly to the surface that is delivered as a large, localized CA package. The T2 improvement with the dosing experiment further corroborates a high, localized loading of the CA using the InP/ZnS surface as a scaffold. The conjugated sample performs well as a high field contrast agent, as is expected with a Dy³⁺ paramagnetic ion.

The InP/ZnS-CAAKATat-DOTA-Dy results indicate that T1 contrast with the Tat delivery may be possible. Furthermore, the Tat endocytosis by macropinocytosis was

not perturbed by appending the DOTA-Dy to the peptide. The minimal difference in measured T2 for the InP/ZnS-CAAKATat-DOTA-Dy transfection with and without Lipofectamine is not surprising. Most cationic liposomes are designed to condense DNA plasmids that have a poly-anionic phosphate backbone, so it is unlikely that the cationic liposome could interact with the poly-cationic Tat peptide surface. It is likely that both samples (with or without Lipofectamine) with InP/ZnS-CAAKATat-DOTA-Dy transfected the cell with identical mechanisms, likely macropinocytosis, which resulted in no measurable T2 difference in the samples. The use of InP/ZnS appended with CAAKA(Tat)-DOTA-Dy as a bimodal contrast agent is shown.

The InP offers a more biological and environmentally friendly alternative to traditional CdSe-based quantum dots. Efficient transfection of the contrast agent can be done with either a commercial cationic liposome transfecting agent or with appending the Tat peptide to the quantum dot surface. The Tat uptake mechanism does not seem to be perturbed with the appended DOTA-Dy to the Lys side chain in the peptide sequence, but further experiments comparing the uptake mechanisms of the material with or without DOTA-Dy are necessary for an accurate evaluation

4.4 Future Work

Future work with the bimodal contrast can be expanded in many directions. Work is currently underway to increase the “payload” or number of DOTA-Dy on the surface of the InP/ZnS. Improving the delivered payload can be accomplished by incorporating more Lys residues and subsequently more DOTA-Dy on to the Tat sequence. Currently, only one DOTA-Dy is appended to the Tat peptide sequence. A second goal is to increase the T1 contrast (positive contrast) with Tat by labeling the peptide sequence with DOTA-Dy through a C-terminal Lys, thereby hopefully increasing the rapid water exchange rate in the cytosol. Further tests with other trivalent Lanthanides, especially Eu and Tm, is critical.

CHAPTER 5

NANO-MEDIATED DELIVERY OF DUAL GENE REGULATORS

5.1 Introduction

Individuals afflicted with genetic disorders traceable to protein mutations (i.e. cystic fibrosis, sickle cell anemia) have the potential for improved well-being and longevity if the aberrant protein can be deliberately manipulated by controlled knockdown or transient expression of the proper protein. Gene therapeutics based on siRNA for knockdown and non-native gene introduction can systematically target a genetic mutation and provide expression of the non-mutated form. Introduction of non-native gene regulators into cells via transfection, whether it's a gene with promoter or short interfering RNA (siRNA), opens the potential for stimuli-induced transient gene expression and/or gene knockdown as an alternative medical technology in the form of a drug regimen. While delivery of gene regulators via viral pathways has been extensively reported, the use of stimuli-responsive nano-carriers offers a non-viral gene therapeutic delivery strategy [156] where issues of immunogenic response or protein over-expression due to gene insertion can be easily circumvented [157]. A recent development in the field has employed nanoscale materials below 5 nm in size (quantum dots and nano metals) as the scaffold for control over the dosage level, and duration of function of the gene therapeutic [136, 137, 158].

Recent studies in the field have focused on either gene delivery or siRNA knockdown within mammalian cells via a nano-scaffold gene therapeutic delivery, in particular surface modified nanoscale metals and semiconductor quantum dots [159-166]. These studies clearly demonstrate that while transfection is efficient, gene regulation is only moderately effective. The nanomaterial delivery platform is less efficient than achieved using a viral vector. However, a nanomaterial platform offers the opportunity to engineer a system that not only delivers a gene, but can also deliver

siRNA for knockdown of protein expression, and can couple peptide or proteins to control cellular uptake into targeted cells. The difference in gene regulator effectiveness for the nano-platform can be traced to apparent limitations arising from the release of the gene regulator from the nanomaterial surface [167, 168], slow endosomal/ lysosomal escape, or exocytosis via lysosomal pathways. This chapter aims to expand the state-of-the-art for nano-biomedical gene therapeutics by combining both transient expression and gene knockdown through the use of a 5.7 nm AuNP co-loaded with siRNA and a linearized gene capable of regulating fluorescent protein expression levels in a mammalian cell (Lec-1). The gene regulators are covalently attached to the AuNP surface to prevent dissociation prior to intra-cellular delivery. In addition, we probe the limiting steps for gene regulation are probed by the two independent gene regulatory functions of linearized DNA (lDNA) (the gene) and siRNA using an NSET molecular beacon approach [64, 169] for tracking.

Using a cationic liposome (Optifect; Invitrogen) on 30% confluent cells, the delivery of the nano-gene regulators and the gene regulatory function in-vitro is followed in-real time on live mammalian cells. In these studies, it is observed that native gene knockdown via siRNA interruption of gene translation of eGFP is nearly immediate (< 12h); however is short-lived with measurable increase in eGFP levels 36 h following transfection. In contrast, non-native protein expression (DsRed-express), which is initiated by transport of the delivered linearized gene to the nucleus, is observed to slowly turn-on requiring 36 h, yet continues to produce DsRed-express up to 10 days after the transfection period. Gene expression levels for eGFP return to control levels by 60 h, while for DsRed-express 14 days are required. The long duration for non-native gene expression in these cells (average doubling rate of 14h) implies that daughter cell populations contain the gene therapeutics by division of the endosomal packages during mitosis. In the NSET beacon analysis, the observation of the splitting of the gene regulators by daughter cells during mitosis is tracked by wide-field optical microscopy in time. In order to track the mechanism that limits the rate of gene regulatory function, the events associated with transfection, release from a AuNP surface, and escape from the endosome are followed using a nanometal surface energy transfer (NSET) beacon. These results strongly suggest that for liposomal mediated

transfection neither the transfection event nor release from the AuNP in the endosome limit the gene regulatory capability of the nanoscaffold. It appears that the escape from the endosome is the limiting step [32, 170] and more importantly is dependent on the length of the nucleic acid package, rather than the type of gene regulatory element. The result of these studies implies that bimodal gene regulation is achievable in mammalian cells, but endosomal escape must be induced in response to cellular stimuli to permit the timing of gene regulation to be definitively controlled.

5.2 Materials and Methods.

Bimodal gene regulation with siRNA and linearized DsRed-express gene

For bimodal gene regulation, a 33-base single-strand siRNA with 5'-monothiol (Midland) for eGFP knockdown [171] and linearized pCMV-DsRed-express plasmid (Clontech) were attached to the surface of bis(p-sulfonatophenyl)phenylphosphine (bSPP) passivated 5.7 nm AuNPs via standard ligand exchange protocols. The pCMV-DsRed-express circular plasmid was cut at restriction sites for AFLIII and NheI resulting linearized DNA with a blunt 5' terminal end (NheI) and a 3' 3-base pair overhang, which can be ligated using T4 ligase (New England Biolabs, Inc) to a short, thiol-terminated dsDNA sequence for coupling to the AuNP surface. The exchange of the bSPP surface passivant by siRNA and linearized plasmid was accomplished by sequential exchange through initial DsRed appendage, followed by siRNA loading. The reaction was allowed to equilibrate at +4 °C for 10d. Unreacted material is removed by ethanol precipitation followed by gel analysis on a 2% TBE-Agarose gel. The loading ratio of DsRed-express linearized plasmid and single-strand siRNA to DsRed is 100 : 1 mole ratio based on initial loading stoichiometry.

Simultaneous knockdown and transient protein expression.

Knockdown and transient protein expression cell experiments were performed in an eGFP stable transform of Lec1 (Chinese Hamster Ovary cell variant), with 50% secretion of eGFP. Molecular beacon release kinetic experiments were performed in

CHO-K1 cells. Both CHO cell variants were grown at 37°C in Dulbeccos Modified Eagle's Medium (DMEM) supplemented with 10% non-essential amino acids, 10% cosmic calf serum, 1% antibiotics / antimycotics, and 0.1% Gentamycin. Cell transfection was performed at 30% confluence ($\sim 0.5 \times 10^6$ cells) in a 6-well plate or 35mm live-cell imaging dish (Matteck Corp) using Optifect (Invitrogen) according to the manufacturers recommended procedure for siRNA delivery.

The cells were allowed to incubate in the transfecting media for 18 h, followed by media exchange to remove Optifect and non-transfected AuNP gene therapeutics from the growth media. GFP production in the media (secreted GFP) and in the cell (non-secreting line) was tracked by total eGFP fluorescence using a NanoDrop3300 (ThermoScientific) with blue LED excitation (480 nm) and 509 nm emission for eGFP in media prior to and following media exchange, while DsRed-express production is only monitored after media exchange by optical microscopy.

Intracellular molecular beacon assay for nucleic acid release kinetics.

For live-cell imaging of intracellular release kinetics, a 15bp dsDNA (5' – AF488(C6) CGTGTGAATTCGTGC – 3') and complement (5' – SH(C6) GCACGAATTCACACG – 3') (Midland) was used to simulate and track siRNA release. The terminal AF488 on the 15bp dsDNA should be 100% quenched when appended to the AuNP surface according to SET theory [64, 169]. The linearized plasmid is labeled with an AF594 dye appended to the ligated linker strand at the 15th base position, and exhibits 100% quenching at this distance according to SET theory.

The nucleic acid – AuNP sample was tested with Optifect (no cells), Optifect (CHO cells), and no Optifect to determine the intracellular release and diffusion of both the short 15bp dsDNA and linearized plasmid appended to the AuNP surface through the dye-labeled linker strand. Live-cell imaging was done on a Nikon TE2000 microscope with a Nikon C1Si spectral confocal detector outfitted with a transmitted light detector. For AF488 tracking, widefield epifluorescence with a FITC filter cube (excitation 475-490 nm) was employed and linearized plasmid release was monitored using a TRITC filter cube (excitation 545-565 nm). Cell imaging for the 15-mer dsDNA was performed at 1, 2, 4, 6, and 24 h post-transfection while the linearized plasmid cell

imaging was performed at 1, 2, 4, 6, 12, 24 h post-transfection. Each sample (Optifect, no Optifect, Optifect-no cells) was imaged for 15 mins and returned to the incubator until measuring the next time point.

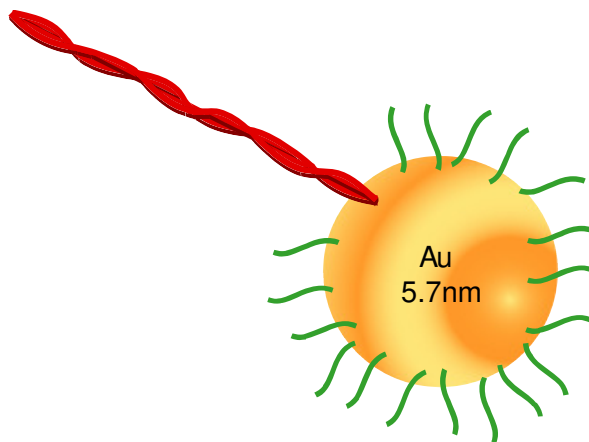


Figure 5.1: Dual labeled Au5.7 nm gene therapeutic scaffold with DsRed-express linearized DNA (red) and siRNA for eGFP knockdown (green)

5.3 Results

Engineering the AuNP gene therapeutic.

The introduction of bimodal gene regulatory elements is accomplished through the use of a 5.7nm AuNP co-labeled by a non-native gene for DsRed-express and short interfering RNA (siRNA) for knockdown of eGFP in a stable transform Lec-1 cell line (Figure 5.1). Co-labeling of a bSPP (bis(p-sulfonatophenyl)phenylphosphine) passivated 5.7 nm Au (AuNP) is accomplished by initially ligand exchanging the bSPP with the linearized gene (IDNA) for DsRed express with a 1.1:1 ratio of IDNA to AuNP that results in approximately *one* gene per AuNP. The IDNA consists of the c-DNA and the CMV promoter, as well as a short (20 bp) linker strand that has a 5' appended C₆-thiol tail for coupling to the AuNP surface. The siRNA is then back-filled onto the AuNP surface using a 50:1 siRNA to AuNP ratio to yield approximately a ~50:1 siRNA to IDNA ratio on the AuNP gene therapeutic based on the initial stoichiometry. The remaining sites have bSPP.

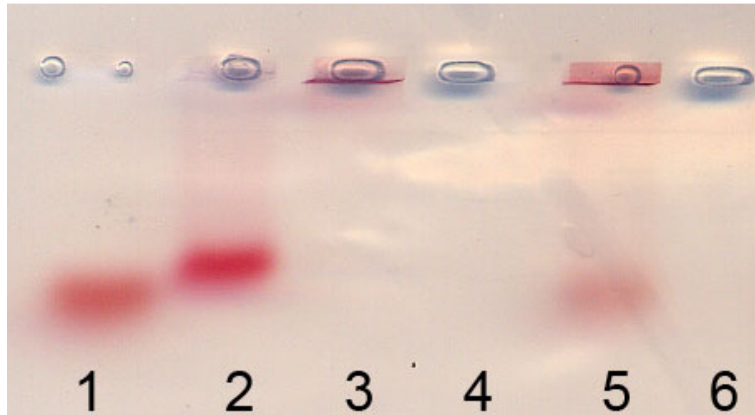


Figure 5.2: 2% agarose gel with lane 1) Au 5.7nm, 2) siRNA AuNP, 3) IDNA / siRNA AuNP, 4) blank, 5) IDNA / siRNA AuNP excess linker strand, and 6) blank.

Separation of the gene regulators assembled onto a 5.7 nm AuNP is shown in Figure 5.2. The red bands arise from the presence of the 5.7 nm AuNP surface Plasmon resonance, and not due to gel staining. In the 2% agarose gel, Lane 1 shows the (bSPP) capped 5.7 nm AuNP, Lane 2 shows the Au-siRNA assembly, Lane 3 is the IDNA / siRNA AuNP, and lane 5 is the Au-IDNA. It is clear by inspection of the gel that appending both the IDNA and siRNA onto the AuNP results in the assembly being retained in the well, while the siRNA labeled AuNP or free AuNP shows mobility towards the cathode. In lane 5, the plasmid labeled AuNP is retained in the well, but contributions from the bSPP Au is observed. No free bSPP Au is observed in Lane 2 or Lane 3, consistent with efficient ligand exchange. The slight mobility difference for the siRNA (single stranded, 33 bases) and the bSPP AuNP is not surprising, as the hydrodynamic radius is larger and has more mass due to the siRNA loading level. The lack of mobility of the IDNA / siRNA AuNP complex is not surprising due to the 1972 bp sequence length dominating the particle mobility.

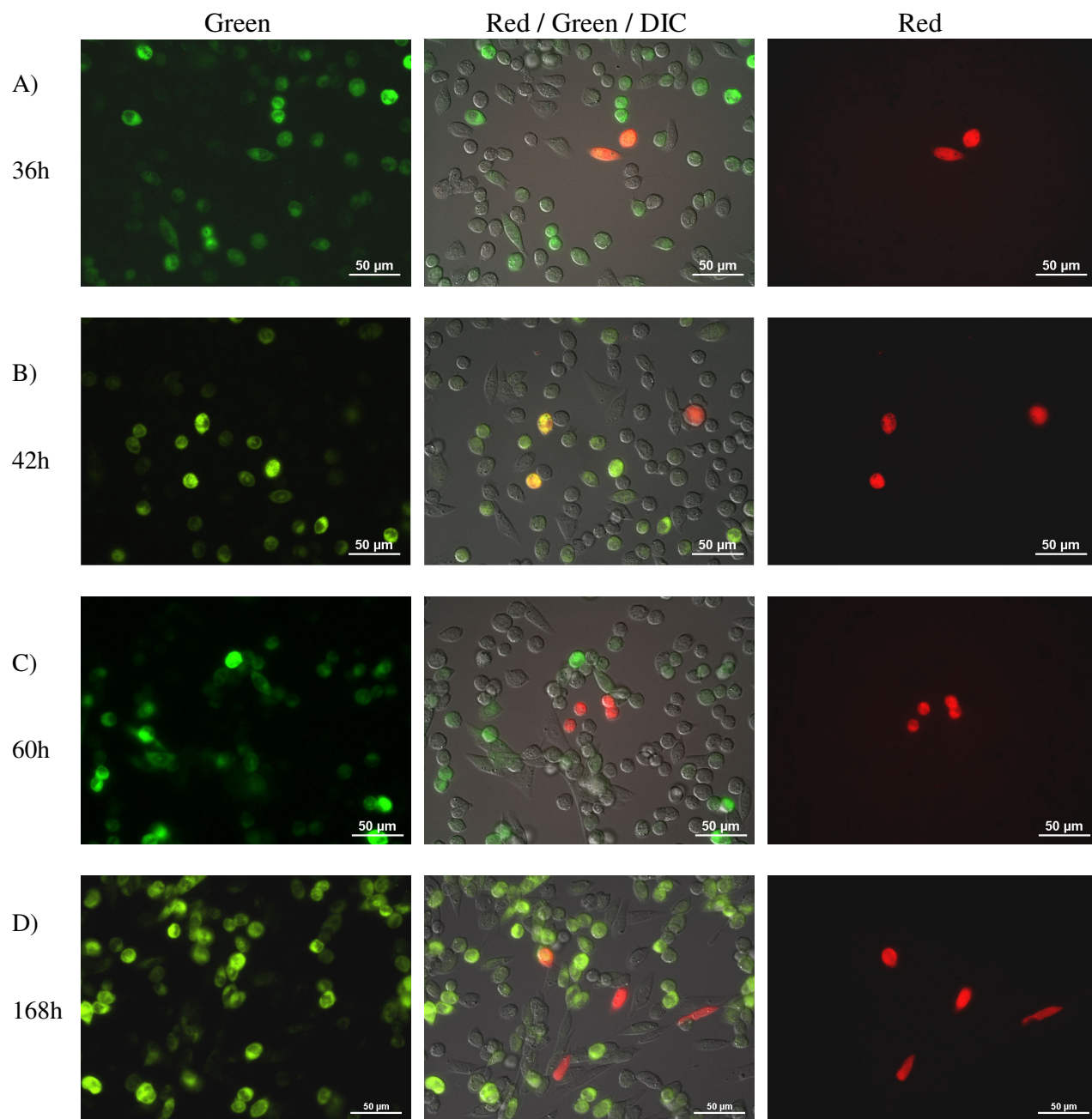


Figure 5.3: Widefield epifluorescence images of Green (FITC filter), Red/Green/DIC, and Red (TRITC filter) of Lec-1 cells transfected with Au5.7 nm at A) 36 h, B) 42 h, C) 60 h, and D) 168 h post-transfection.

Cellular Uptake and Gene Regulation in Lec-1 Mammalian Cells.

The transient expression of eGFP and DsRed fluorescent protein levels were monitored for 14 days using optical microscopy by splitting cells to 25% confluence every 48 h. Figure 5.3 shows the time-course optical microscopy images comparing the green channel (left side) and the red channel (right side) to the red/green/DIC (middle, where DIC is differential image contrast) of Optifect mediated transfection of eGFP producing Lec-1 cells by the IDNA / siRNA AuNP. Inspection of the green channel reveals that at the 36 h time point the lowest number of green cells are observed. eGFP intensity and thus protein levels in the cell do not show recovery until $t > 42$ h in the optical microscopy image. The reduction in green intensity (not to be confused with green cells, as eGFP is retained and has a finite lifetime) implies efficient early knockdown of eGFP expression in the IDNA / siRNA AuNP treated Lec-1 cells. Complete recovery of the eGFP fluorescence signature is observed at 168 h.

Inspection of the red channel (Figure 5.3) indicates few cells are expressing DsRed express in the first 36 h (2.2% of cells in image). A very slow increases in the DsRed intensity is observed in the optical images with 3.1% red fluorescent cells at 42 h (Figure 5.3 B), 3.5% at 60 h (Figure 5.3 C), 3.2% at 168 h (Figure 5.3 D), and 3% at 240 h (not shown). The near asymptotic value for DsRed express protein levels in the cell is indicative of daughter cell expression, as these cells are in log growth phase and are cut to 25% of cell count every 48 h. Consistent with the DsRed express expression in the Lec-1 cell line being a transient gene regulation, complete loss of observable red fluorescent cells occurs in the experiment after 336 h (14 d).

Dual delivery on the nano-scaffolded gene regulator is confirmed by analyzing the red and green cells that are overlaid in the DIC image. In the red /green /DIC overlay (Figure 5.3 middle images), the red cells appear orange in the overlay image indicating the red cells are also expressing eGFP fluorescence. Since the green intensity is variable due to knockdown, the image color saturation depends on the magnitude of eGFP or DsRed expression in the individual cells and the time slice.

To analyze the time-course of the gene regulation for eGFP knockdown, the eGFP knockdown was also measured by total media fluorescence for eGFP secreting Lec-1 cells, as shown in Figure 5.4. It is important to note that the mutated Lec-1 cell

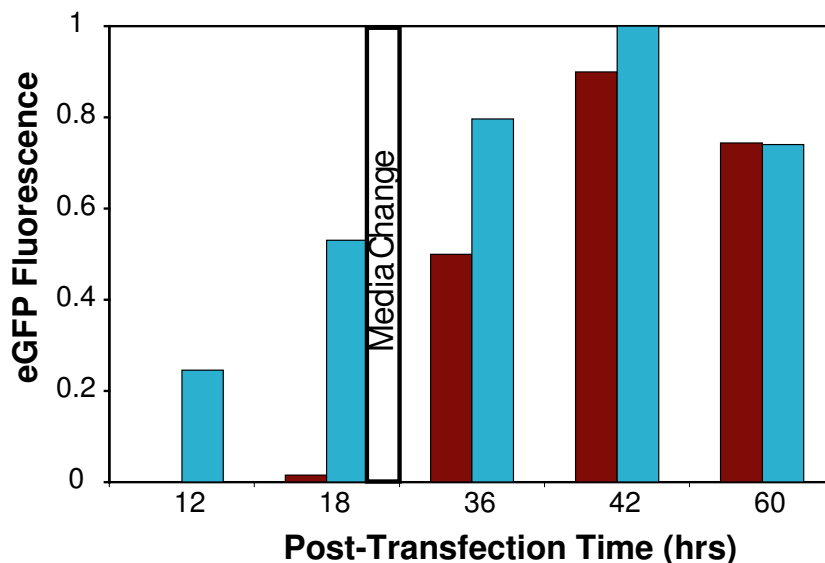


Figure 5.4: Time-dependent knockdown of eGFP fluorescence in eGFP producing Lec-1 cells with siRNA / linearized plasmid labeled AuNP.

line used in this study is chosen intentionally since 50% of the cells are secreting eGFP and 50% are non-secreting eGFP cell lines, thus allowing the optical images which can be skewed by exposure times to be correlated to a direct fluorescence intensity measurement. In Figure 5.4, the eGFP expression level relative to a control (non-transfected Lec-1 with media exchanged at 0 h and again at 18 h) that Lec-1 cells treated with IDNA / siRNA AuNP exhibit complete absence of eGFP fluorescence in the media up to 18 h, implying 100% knockdown efficiency of eGFP production, as well as 100% transfection levels. The high percentage of knockdown is surprising as the reported transfection efficiency for cationic liposomes is typically ~30-40% for oligonucleotides. Following the second media exchange at 18h, the media eGFP fluorescence begins to increase rapidly, indicating loss of knockdown activity, with complete recovery to native eGFP expression levels after 42 h. The drop in intensity at 60 h reflects over growth of the cells and subsequent cellular death as observed in the control sample.

The efficiency of transfection and thus the explanation for the observed high degree of eGFP knockdown in the Lec-1 cells can be monitored by analyzing the time-course optical microscopy images for the presence of the AuNP. The AuNP will appear

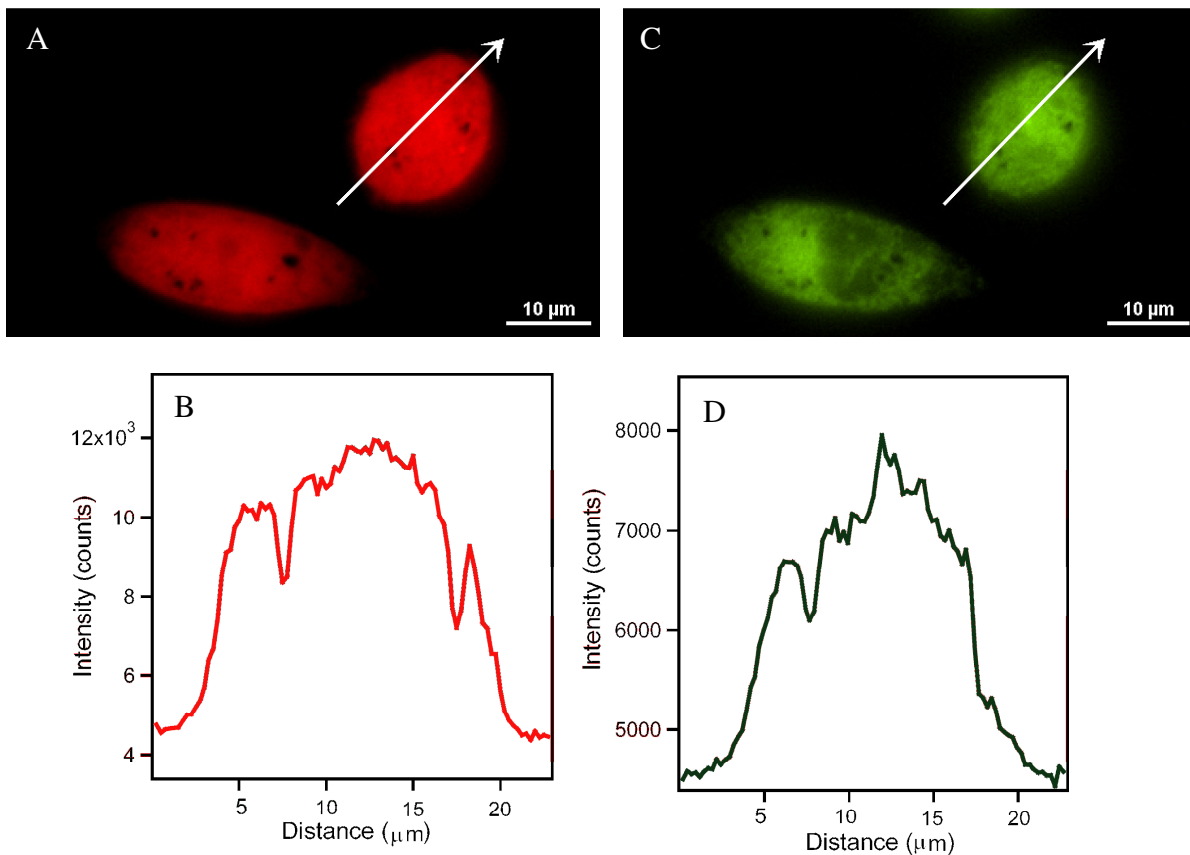


Figure 5.5: A) Cropped image of DsRed-express produced in C) Lec-1 cell with white arrow across the length of the cell to indicate the presence of dark spots (AuNP) shown in B) and D) as Intensity versus distance trajectory plot showing positive intensity counts for DsRed and eGFP and negative intensity for the AuNP.

as a dark spot in the image where the AuNP has aggregated within endosomes / lysosomes. In Figure 5.5, the fluorescence intensity across a red (DsRed expressing) and green (eGFP expressing) Lec-1 cell is shown along the trace line in the image (white arrow). The intensity plot versus trajectory (Figure 5.5 B, D) shows a loss of intensity at 30 and 70 μm occurring at the dark spot on the right side of the upper cell in the red channel (Figure 5.5 A).

Inspection of the green channel (Figure 5.5 B, D) confirms the intensity is a loss in the vicinity of the dark spot, confirming the red channel results. We believe the dark spots, which are observable in cells up to 60 h, arise from AuNP aggregation in the vesicles of the cell, implying transfection has occurred. Inspection of a larger image shows nearly all cells have a dark spot present in the cell implying efficient transfection consistent with the observation of 100% knockdown of eGFP following transfection. The

observation of a dark spot for a AuNP aggregate is not surprising since the AuNP surface plasmon resonance spans the region of the TRITC (545 – 565 nm) excitation source.

Limited DsRed Expression in Lec-1 cells.

The gene regulation by siRNA and LDNA occur on markedly different timescales and levels. In the optical images in Figure 5.3, DsRed-express levels is low, ~3% over all time points, but the duration of expression is remarkably long by comparison to the shorter timescale for action of the siRNA on eGFP expression levels. The poor gene regulation for IDNA versus siRNA may reflect a number of possibilities: (i) slow DsRed maturation, (ii) poor release of IDNA from the AuNP surface, (iii) the inability of the DNA to efficiently escape the endosome, (iv) lysosomal degradation of the IDNA, or (v) exocytosis of the AuNP gene therapeutic prior to gene release. Although DsRed express is slow to mature (reach maximum fluorescence intensity, $t_{100\%} = 33$ h) [172, 173], the slow turn-on of the DsRed express is not explained by protein maturation, as one would expect an exponential rise in DsRed intensity within 48 h if the mechanism for siRNA action and DsRed action are on similar experimental timescales. While gene transcription is slower than siRNA translation due to the physical location differences and where the regulator operates on the protein expression pathway, although the long timescales of the experiment >42 h, one predicts overlap of activity. A likely possibility for the low DsRed expression levels is recycling / degradation and exocytosis of the AuNP-IDNA package following release of the siRNA from the AuNP surface. However, the observation of the AuNP visible in the cell 36 h after transfection (Figures 5.3, 5.5) and up to 60 h implies exocytosis may not be a significant factor for the poor DsRed express production.

An alternate explanation that may contribute to the different time scales for gene regulation is the vast length scale differences between the gene therapeutics, or perhaps the single versus double strand morphology differences, which will impact the net charge between the IDNA and siRNA used in this study. Using a NSET molecular beacon, the rate of release and subsequent endosomal escape of the gene regulator can be tracked in real time by monitoring the appearance of AF594 for AF94 labeled

plasmid or AF488 for AF488 labeled short duplex DNA by monitoring the molecular dye fluorescence in live cell images. The NSET molecular beacon functions by proximity energy transfer quenching of the IDNA appended AF594 (or AF488 for 15bp DNA) through energy transfer to the AuNP. The AuNP is non-emissive, which allows the onset of AF594 emission to signal the release of the IDNA from the AuNP surface.

Figure 5.6 shows the time-course optical microscopy experiment on CHO cells for the 1972bp IDNA internally labeled at the 15th base position by A594 (A-D) and the 15-mer terminally labeled at the 5' end with AF 488 (E-H). Comparison of the 1972 base pair system to a shorter duplex (15-mer) allows the assessment of whether length of the plasmid or type of nucleic acid is a contributing factor to the poor level of DsRed express production. For the IDNA sequence, there is no visible dye emission at 1 h (Figure 5.6 A), while at 4 h (Figure 5.6 B) dye emission appears localized in the endosomes, indicating IDNA release from the AuNP surface. Diffuse emission from AF594 is observed at 12 h and the 24 h images (Figure 5.6 D) show emission outside of the endosome within the cytosol implying endosomal escape of the IDNA. However, the magnitude of intensity compared to the endosome intensity is quite small suggesting endosomal escape is inefficient for the IDNA sequence. Even at 24 h, the IDNA sample shows larger vesicles formed and the AF594 is predominately localized in these vesicles.

In Figure 5.6 (E-H) the 15 base pair duplex DNA labeled by a terminal AF488 shows very similar results; however, fluorescence is immediately observed within 1 h for the AF488 with diffusion into the cytosol observed within 2 h. The cytosolic : endosomal fraction for the 15bp sequence rapidly increases during the experimental time course. In contradiction to the IDNA results, the 24 h sample clearly shows most of the DNA diffused into the cytosol. It is notable that the rate of release from the AuNP surface and diffusion for the shorter DNA sequence appears to be significantly faster than the IDNA sample. The efficient endosomal escape for the 15-mer duplex compared to the IDNA may be the reason that DsRed production remains at merely 3% throughout the experiment. No dye emission was noted for non-transfected Optifect samples containing the identical AuNP- IDNA (AF594-labeled).

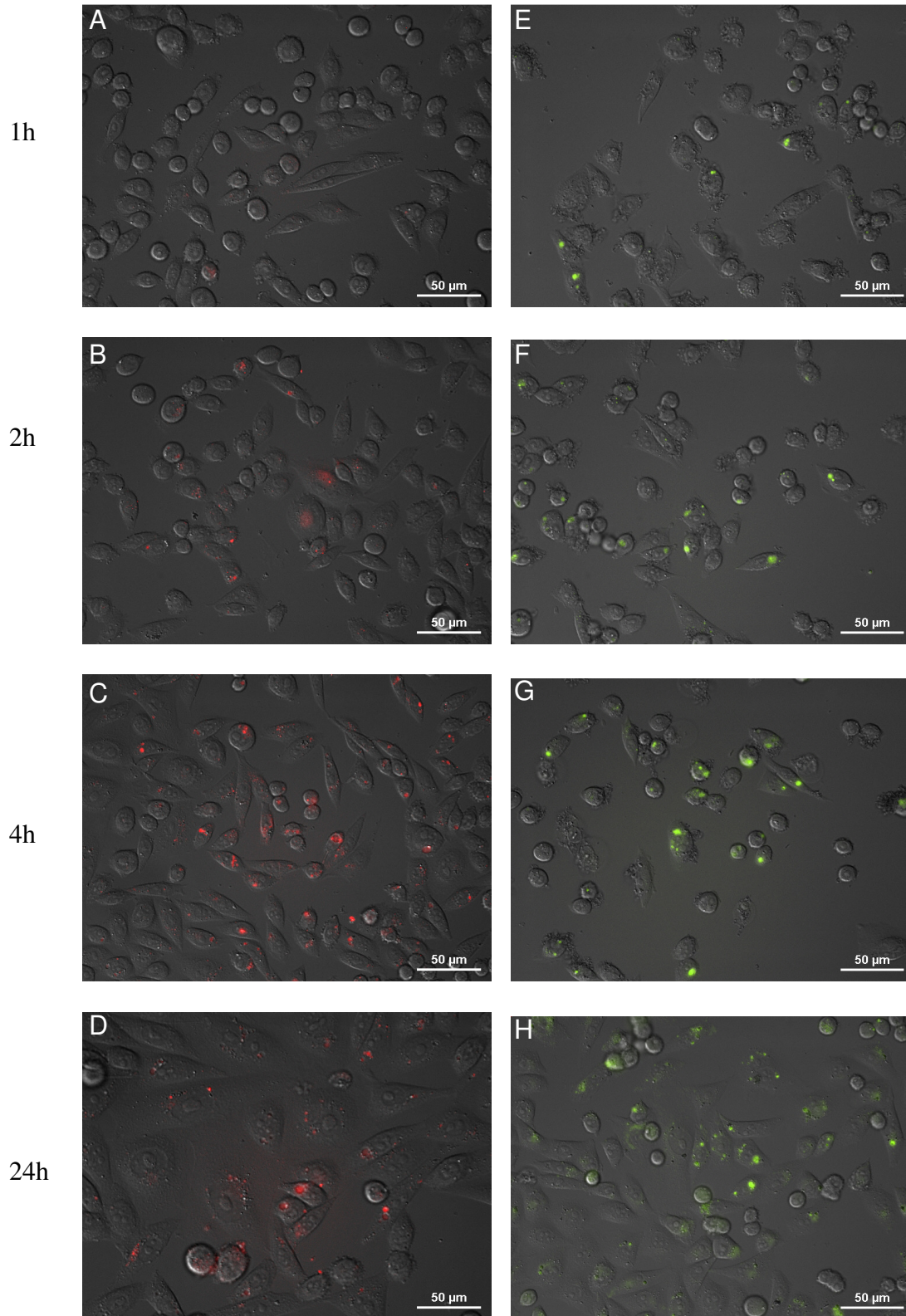


Figure 5.6: CHO cells incubated with AuNP-IDNA with AF594 (A-D) and the AuNP-15-mer with AF488 (E-H).

Redistribution and Repackaging of Endosomal Packages.

Figure 5.7 displays the redistribution of endosomal packages of AF488 dsDNA in a CHO cell during mitotic division. In this image the endosome packages show initial AuNP release (fluorescence-on) at 1 h (Figure 5.7 A), visible diffusion by 4 h (Figure 5.7 B), followed by mitosis and redistribution of the AF488 labeled 15bp-AF488 in the two daughter cells within 6 h (Figure 5.7 C). The 12 h image (Figure 5.7 D) shows loss of AF488 intensity in one daughter cell along with enhanced cytosol diffusion of the AF488 out of the endosome in the second daughter cell. The observation of endosomal redistribution during mitosis explains the sustained DsRed production out to 10 day post-transfection, even though the cells have been cut to 25% every 48h.

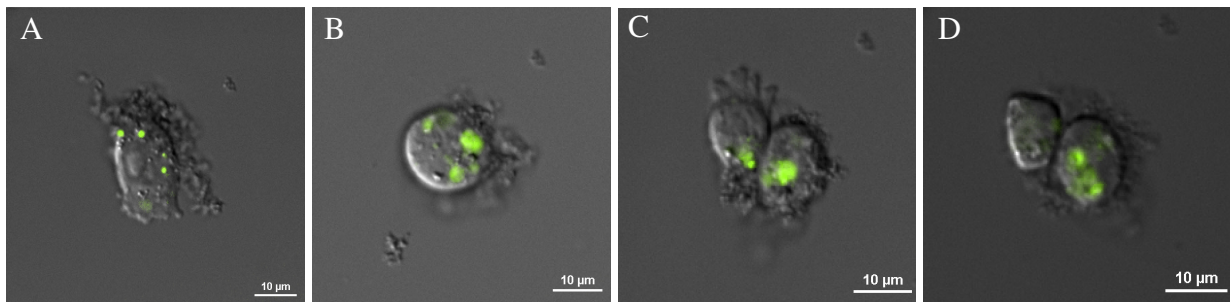


Figure 5.7: Widefield DIC – epifluorescence overlay (FITC) of CHO cell with Au-DNA(AF488) showing the transport of endosomes of unbound dsDNA-AF488 (fluorescence not quenched) during cell division at A) 1 h, B) 4 h, C) 6 h, D) 12 h.

constant in this region due to the presence of the AuNP. The observation of the fluorescent pit implies that packaging of the IDNA may be occurring in the endosome (or lysosome) and may be providing a pathway for exocytosis of the excess IDNA and AuNP from the cell. Due to the log growth phase of the Lec-1 cells, it is difficult to follow the fate of these packages after 48 h. Further investigations are underway to track the fate of the package at longer experimental times. In the control sample, no pitting was observed at any time point.

5.4 Discussion

The observation of dual gene regulation involving knockdown and controlled protein expression opens new frontiers for use of these nanometal gene therapeutics in nano-medicine. In the study, the rate of gene regulation for the independent knockdown (siRNA) and up-regulation (IDNA) is directly linked to the ability of the nucleic acid sequences to escape the endosome. The molecular beacon results imply that endosomal escape is the rate limiting step since many endosomes still contain AF594 fluorescence (linearized plasmid released from the AuNP surface) even after 12 h (Figure 5.3). No significant differences in release from the AuNP surface for the short and long DNA sequence is observed, with the endosomes revealing strong fluorescence within the first 2 h for both DNA lengths. The limited response of the linearized DNA appears to be traceable to the inability to diffuse from the endosome before being packaged in a lysosome. This supports the earlier suggestion that endosomal rupture [32, 170] and not the release of the therapeutic from the AuNP surface is critical for gene regulatory function. The slow endosomal escape and observed cytosol diffusion for the IDNA relative to the siRNA is consistent with the observation that diffusion scales linearly with DNA length, with a 65-fold linear decrease in diffusion rate between 21-6000 bp strands [174].

The use of the cationic liposome (Optifect) transfecting agent improves the number of transfected AuNP conjugates. A remarkable finding in this study is the high transfection efficiencies and 100% knockdown of the eGFP signatures in the CHO cells. The differences in knockdown efficiency in this study (50%) as compared to previous eGFP silencing reports utilizing antisense DNA and AuNP [159] (20%) is likely due to three factors: the total number of transfected nanoparticles with the cationic liposome agent is greater (nearly all cells show the presence of AuNPs), siRNA is shown to have longer duration and silencing efficiency when compared with antisense DNA [171], and differences in cell types used in the two knockdown studies can affect both the efficiency of transfection and gene regulatory function [175].

This non-viral gene-delivery strategy introduces a dual-labeled, nano-mediated platform for simultaneous delivery of gene therapeutics for on a single nanomaterial

surface. Further efforts include specific cell targeting, effect of varying nucleic acid stoichiometries, and linearized plasmid delivery of disease-related proteins as potential gene therapeutic candidates are underway.

REFERENCES

1. Leicester, H. M., *Development of Biochemical Concepts from Ancient to Modern Times*. 1974, Cambridge: Harvard University Press. 286.
2. Teich, M. and Needham, D. M., *A Documentary History of Biochemistry 1770 - 1940*. 1992, Rutherford: Fairleigh Dickinson University Press. 579.
3. Fruton, J. S., *Molecules and Life: Historical Essays on the Interplay of Chemistry and Biology*. 1972, New York: Wiley-Interscience. 579.
4. Watson, J. D., *The Double Helix: A Personal Account of the Discovery of the Structure of DNA*. 1968, New York: Atheneum Publishers. 143.
5. Venter, J. C., et al., *The sequence of the human genome*. *Science*, **2001**, *291*, 1304-1351.
6. On the basic concept of nanotechnology, proceedings of the international Conference of Production Engineering, 1974"
7. Feynam, R.P. American Physical Society Meeting, Pasadena, CA 1959.
8. Barber, D. J. and Freestone, I. C., *An Investigation of the Origin of the Color of the Lycurgus Cup by Analytical Transmission Electron-Microscopy*. *Archaeometry*, **1990**, *32*, 33-45.
9. Scott, G. D., *A Study of the Lycurgus-Cup*. *Journal of Glass Studies*, **1995**, *37*, 51-64.
10. Freestone, I., Meeks, N., Sax, M., and Higgitt, C., *The Lycurgus Cup - A Roman nanotechnology*. *Gold Bulletin*, **2007**, *40*, 270-277.
11. Hornyak, G. L., et al., *Effective medium theory characterization of Au/Ag nanoalloy porous alumina composites*. *Nanostructured Materials*, **1997**, *9*, 571-574.
12. Faraday, M., *Experimental Relations of Gold (and other Metals) to Light*. *Philos Trans R Soc Lond*, **1857**, *147*, 145-181.
13. Thompson, D., *Michael Faraday's recognition of ruby gold: the birth of modern nanotechnology*. *Gold Bulletin*, **2007**, *40*, 267-269.
14. Kroto, H. W., Heath, J. R., O'Brien, S. C., Curl, R. F., and Smalley, R. E., *C-60 - Buckminsterfullerene*. *Nature*, **1985**, *318*, 162-163.

15. Murray, C. B., Norris, D. J., and Bawendi, M. G., *Synthesis and Characterization of Nearly Monodisperse Cde (E = S, Se, Te) Semiconductor Nanocrystallites*. J Am Chem Soc, **1993**, *115*, 8706-8715.
16. Kalyanasundaram, K., Borgarello, E., Duonghong, D., and Gratzel, M., *Cleavage of Water by Visible-Light Irradiation of Colloidal Cds Solutions - Inhibition of Photocorrosion by Ruo2*. Angew Chem, Intl Ed, Eng, **1981**, *20*, 987-988.
17. Henglein, A., *Photochemistry of Colloidal Cadmium-Sulfide .2. Effects of Adsorbed Methyl Viologen and of Colloidal Platinum*. J Phys Chem, **1982**, *86*, 2291-2293.
18. Henglein, A., *Photo-Degradation and Fluorescence of Colloidal-Cadmium Sulfide in Aqueous-Solution*. Berichte Der Bunsen-Gesellschaft-Physical Chemistry Chemical Physics, **1982**, *86*, 301-305.
19. Rossetti, R. and Brus, L., *Electron-Hole Recombination Emission as a Probe of Surface-Chemistry in Aqueous Cds Colloids*. J Phys Chem, **1982**, *86*, 4470-4472.
20. Kuczynski, J. and Thomas, J. K., *Photochemistry at the Surface of Colloidal Cadmium-Sulfide*. Chem Phys Lett, **1982**, *88*, 445-447.
21. Ruan, G., Agrawal, A., Smith, A. M., Gao, X. H., and Nie, S. M., *Quantum dots as fluorescent labels for molecular and cellular imaging*. Reviews in Fluorescence 2006, **2006**, *3*, 181-+.
22. Medintz, I. L., Uyeda, H. T., Goldman, E. R., and Mattoussi, H., *Quantum dot bioconjugates for imaging, labelling and sensing*. Nat Mater, **2005**, *4*, 435-446.
23. Sapsford, K. E., Pons, T., Medintz, I. L., and Mattoussi, H., *Biosensing with luminescent semiconductor quantum dots*. Sensors, **2006**, *6*, 925-953.
24. Chan, W. C., et al., *Luminescent quantum dots for multiplexed biological detection and imaging*. Curr Opin Biotechnol, **2002**, *13*, 40-46.
25. Iga, A. M., Robertson, J. H., Winslet, M. C., and Seifalian, A. M., *Clinical potential of quantum dots*. J Biomed Biotechnol, **2007**, *2007*, 76087.
26. Sutherland, A. J., *Quantum dots as luminescent probes in biological systems*. Curr Opin Solid St M, **2002**, *6*, 365-370.
27. Gao, X. H., et al., *In vivo molecular and cellular imaging with quantum dots*. Curr. Opin. Biotechnol., **2005**, *16*, 63-72.
28. Kogan, M. J., et al., *Peptides and metallic nanoparticles for biomedical applications*. Nanomed, **2007**, *2*, 287-306.

29. Mccarthy, J. R., Kelly, K. A., Sun, E. Y., and Weissleder, R., *Targeted delivery of multifunctional magnetic nanoparticles*. *Nanomed*, **2007**, *2*, 153-167.
30. Zhao, M., Kircher, M. F., Josephson, L., and Weissleder, R., *Differential conjugation of tat peptide to superparamagnetic nanoparticles and its effect on cellular uptake*. *Bioconjug Chem*, **2002**, *13*, 840-844.
31. Delehanty, J. B., et al., *Self-assembled quantum dot-peptide bioconjugates for selective intracellular delivery*. *Bioconjug Chem*, **2006**, *17*, 920-927.
32. Ruan, G., Agrawal, A., Marcus, A. I., and Nie, S., *Imaging and tracking of tat peptide-conjugated quantum dots in living cells: new insights into nanoparticle uptake, intracellular transport, and vesicle shedding*. *J Am Chem Soc*, **2007**, *129*, 14759-14766.
33. Gupta, A. K. and Gupta, M., *Synthesis and surface engineering of iron oxide nanoparticles for biomedical applications*. *Biomaterials*, **2005**, *26*, 3995-4021.
34. Berry, C. C., *Intracellular delivery of nanoparticles via the HIV-1 tat peptide*. *Nanomed*, **2008**, *3*, 357-365.
35. Berry, C. C., De La Fuente, J. M., Mullin, M., Chu, S. W. L., and Curtis, A. S. G., *Nuclear localization of HIV-1 tat functionalized gold nanoparticles*. *IEEE Transactions on Nanobioscience*, **2007**, *6*, 262-269.
36. De La Fuente, J. M. and Berry, C. C., *Tat peptide as an efficient molecule to translocate gold nanoparticles into the cell nucleus*. *Bioconjug Chem*, **2005**, *16*, 1176-1180.
37. Thaxton, C. S., Georganopoulou, D. G., and Mirkin, C. A., *Gold nanoparticle probes for the detection of nucleic acid targets*. *Clinica Chimica Acta*, **2006**, *363*, 120-126.
38. Fritzsche, W. and Taton, T. A., *Metal nanoparticles as labels for heterogeneous, chip-based DNA detection*. *Nanotechnol*, **2003**, *14*, R63-R73.
39. Santra, S., Dutta, D., Walter, G. A., and Moudgil, B. M., *Fluorescent nanoparticle probes for cancer imaging*. *Technol Cancer Res Treat*, **2005**, *4*, 593-602.
40. Ito, A., Shinkai, M., Honda, H., and Kobayashi, T., *Medical application of functionalized magnetic nanoparticles*. *J Biosci Bioeng*, **2005**, *100*, 1-11.
41. Lim, Y. T., Lee, K. Y., Lee, K., and Chung, B. H., *Immobilization of histidine-tagged proteins by magnetic nanoparticles encapsulated with nitrilotriacetic acid (NTA)-phospholipids micelle*. *Biochem Biophys Res Commun*, **2006**, *344*, 926-930.

42. Hainfeld, J. F., Liu, W., Halsey, C. M., Freimuth, P., and Powell, R. D., *Ni-NTA-gold clusters target His-tagged proteins*. J Struct Biol, **1999**, *127*, 185-198.
43. Levy, R., *Peptide-capped gold nanoparticles: Towards artificial proteins*. Chembiochem, **2006**, *7*, 1141-1145.
44. Willett, R. L., Baldwin, K. W., West, K. W., and Pfeiffer, L. N., *Differential adhesion of amino acids to inorganic surfaces*. Proc Natl Acad Sci U S A, **2005**, *102*, 7817-7822.
45. Peelle, B. R., Krauland, E. M., Wittrup, K. D., and Belcher, A. M., *Design criteria for engineering inorganic material-specific peptides*. Langmuir, **2005**, *21*, 6929-6933.
46. Aryal, S., Bahadur, K. C. R., Bhattarai, N., Kim, C. K., and Kim, H. Y., *Study of electrolyte induced aggregation of gold nanoparticles capped by amino acids*. J Colloid Interf Sci, **2006**, *299*, 189-195.
47. Porta, F., et al., *Gold nanoparticles capped by peptides*. Mat Sci Eng B-Solid, **2007**, *140*, 187-194.
48. Aryal, S., et al., *Spectroscopic identification of S-Au interaction in cysteine capped gold nanoparticles*. Spectrochim Acta Part A Mol Biom Spec, **2006**, *63*, 160-163.
49. Hu, Y., Das, A., Hecht, M. H., and Scoles, G., *Nanografting de novo proteins onto gold surfaces*. Langmuir, **2005**, *21*, 9103-9109.
50. Smith, J. C., et al., *Nanopatterning the chemospecific immobilization of cowpea mosaic virus capsid*. Nano Lett, **2003**, *3*, 883-886.
51. Blum, A. S., et al., *An engineered virus as a scaffold for three-dimensional self-assembly on the nanoscale*. Small, **2005**, *1*, 702-706.
52. Ackerson, C. J., Jadzinsky, P. D., Jensen, G. J., and Kornberg, R. D., *Rigid, specific, and discrete gold nanoparticle/antibody conjugates*. J Am Chem Soc, **2006**, *128*, 2635-2640.
53. Kanno, S., Yanagida, Y., Haruyama, T., Kobatake, E., and Aizawa, M., *Assembling of engineered IgG-binding protein on gold surface for highly oriented antibody immobilization*. J Biotechnol, **2000**, *76*, 207-214.
54. Kuhnle, A., Linderoth, T. R., Schunack, M., and Besenbacher, F., *L-cysteine adsorption structures on Au(111) investigated by scanning tunneling microscopy under ultrahigh vacuum conditions*. Langmuir, **2006**, *22*, 2156-2160.

55. Xu, Q. M., et al., *New structure of L-cysteine self-assembled monolayer on Au(111): Studies by in situ scanning tunneling microscopy*. Langmuir, **2001**, *17*, 6203-6206.
56. Woehrle, G. H., Brown, L. O., and Hutchison, J. E., *Thiol-functionalized, 1.5-nm gold nanoparticles through ligand exchange reactions: Scope and mechanism of ligand exchange*. J Am Chem Soc, **2005**, *127*, 2172-2183.
57. Donkers, R. L., Song, Y., and Murray, R. W., *Substituent effects on the exchange dynamics of ligands on 1.6 nm diameter gold nanoparticles*. Langmuir, **2004**, *20*, 4703-4707.
58. Montalti, M., et al., *Kinetics of place-exchange reactions of thiols on gold nanoparticles*. Langmuir, **2003**, *19*, 5172-5174.
59. Zachary, M. and Chechik, V., *Hopping of thiolate ligands between Au nanoparticles revealed by EPR spectroscopy*. Angew Chem, Int Ed, **2007**, *46*, 3304-3307.
60. Ionita, P., Caragheorgheopol, A., Gilbert, B. C., and Chechik, V., *Mechanistic study of a place-exchange reaction of Au nanoparticles with spin-labeled disulfides*. Langmuir, **2004**, *20*, 11536-11544.
61. Guo, R., Song, Y., Wang, G. L., and Murray, R. W., *Does core size matter in the kinetics of ligand exchanges of monolayer-protected Au clusters?* J Am Chem Soc, **2005**, *127*, 2752-2757.
62. Hong, R., et al., *In situ observation of place exchange reactions of gold nanoparticles. Correlation of monolayer structure and stability*. Chemical Communications, **2006**, 2347-2349.
63. Jennings, T., Singh, M. P., and Strouse, G. F., *Fluorescent Lifetime Quenching near d=1.5 nm Gold Nanoparticles: Probing NSET Validity*. J Am Chem Soc, **2006**.
64. Yun, C. S., et al., *Nanometal surface energy transfer in optical rulers, breaking the FRET barrier*. J. Am. Chem. Soc., **2005**, *127*, 3115-3119.
65. Assuming $\epsilon_{Au}=155,000/M*cm$ at 420nm and $\epsilon_{Au}=300,000/M*cm$ at 280nm, with $\epsilon_W = 12,000/M*cm$ at 280nm.
66. Lim, J. K., Kim, Y., Lee, S. Y., and Joo, S. W., *Spectroscopic analysis of L-histidine adsorbed on gold and silver nanoparticle surfaces investigated by surface-enhanced Raman scattering*. Spectrochim Acta Part A Mol Biom Spec, **2008**, *69*, 286-289.
67. Jung, C., *Insight into protein structure and protein-ligand recognition by Fourier transform infrared spectroscopy*. J Mol Recognit, **2000**, *13*, 325-351.

68. Barth, A., *The infrared absorption of amino acid side chains*. Prog Biophys Mol Biol, **2000**, 74, 141-173.
69. Barth, A., *Infrared spectroscopy of proteins*. Biochim Biophys Acta, Bioenerg, **2007**, 1767, 1073-1101.
70. Wolpert, M. and Hellwig, P., *Infrared spectra and molar absorption coefficients of the 20 alpha amino acids in aqueous solutions in the spectral range from 1800 to 500 cm⁻¹*. Spectrochim Acta Part A Mol Biom Spec, **2006**, 64, 987-1001.
71. Hasegawa, K., Ono, T., and Noguchi, T., *Vibrational spectra and ab initio DFT calculations of 4-methylimidazole and its different protonation forms: Infrared and raman markers of the protonation state of a histidine side chain*. J Phys Chem B, **2000**, 104, 4253-4265.
72. Mesu, J. G., Visser, T., Soulimani, F., and Weckhuysen, B. M., *Infrared and Raman spectroscopic study of pH-induced structural changes of L-histidine in aqueous environment*. Vib Spectrosc, **2005**, 39, 114-125.
73. Shi, J., Hong, B., Parikh, A. N., Collins, R. W., and Allara, D. L., *Optical Characterization of Electronic-Transitions Arising from the Au/S Interface of Self-Assembled N-Alkanethiolate Monolayers*. Chem Phys Lett, **1995**, 246, 90-94.
74. Mandal, H. S. and Kraatz, H. B., *Effect of the surface curvature on the secondary structure of peptides adsorbed on nanoparticles*. J Am Chem Soc, **2007**, 129, 6356-6357.
75. Hasan, M., Bethell, D., and Brust, M., *The fate of sulfur-bound hydrogen on formation of self-assembled thiol monolayers on gold: H-1 NMR spectroscopic evidence from solutions of gold clusters*. J Am Chem Soc, **2002**, 124, 1132-1133.
76. Kohlmann, O., et al., *NMR diffusion, relaxation, and spectroscopic studies of water soluble, monolayer-protected gold nanoclusters*. J Phys Chem B, **2001**, 105, 8801-8809.
77. Badia, A., et al., *Structure and chain dynamics of alkanethiol-capped gold colloids*. Langmuir, **1996**, 12, 1262-1269.
78. You, C. C., De, M., and Rotello, V. M., *Monolayer-protected nanoparticle-protein interactions*. Curr Opin Chem Biol, **2005**, 9, 639-646.
79. Chan, W. C. W., et al., *Luminescent quantum dots for multiplexed biological detection and imaging*. Curr. Opin. Biotechnol., **2002**, 13, 40-46.
80. Chah, S., Hammond, M. R., and Zare, R. N., *Gold nanoparticles as a colorimetric sensor for protein conformational changes*. Chemistry & Biology, **2005**, 12, 323-328.

81. Bayraktar, H., You, C. C., Rotello, V. M., and Knapp, M. J., *Facial control of nanoparticle binding to cytochrome c*. J Am Chem Soc, **2007**, *129*, 2732-+.
82. Ao, L. M., Gao, F., Pan, B.F., Cui, D.X., and Gu, H.C., *Interaction between Gold Nanoparticles and Bovine Serum Albumin or Sheep Antirabbit Immunoglobulin G*. Chinese Journal of Chemistry, **2006**, *24*, 253-256.
83. Aubin, M. E., Morales, D. G., and Hamad-Schifferli, K., *Labeling ribonuclease S with a 3 nm Au nanoparticle by two-step assembly*. Nano Lett, **2005**, *5*, 519-522.
84. Brewer, S. H., Glomm, W. R., Johnson, M. C., Knag, M. K., and Franzen, S., *Probing BSA binding to citrate-coated gold nanoparticles and surfaces*. Langmuir, **2005**, *21*, 9303-9307.
85. Staii, C., Wood, D. W., and Scoles, G., *Verification of biochemical activity for proteins nanografted on gold surfaces*. J Am Chem Soc, **2008**, *130*, 640-646.
86. Calabretta, M. K., Matthews, K. S., and Colvin, V. L., *DNA binding to protein-gold nanocrystal conjugates*. Bioconjug. Chem., **2006**, *17*, 1156-1161.
87. Aubin-Tam, M. E. and Hamad-Schifferli, K., *Gold nanoparticle-cytochrome C complexes: the effect of nanoparticle ligand charge on protein structure*. Langmuir, **2005**, *21*, 12080-12084.
88. Otsuka, H., Nagasaki, Y., and Kataoka, K., *PEGylated nanoparticles for biological and pharmaceutical applications*. Adv Drug Deliv Rev, **2003**, *55*, 403-419.
89. Teichroeb, J. H., Forrest, J. A., Ngai, V., and Jones, L. W., *Anomalous thermal denaturing of proteins adsorbed to nanoparticles*. European Physical Journal E, **2006**, *21*, 19-24.
90. You, C. C., De, M., Han, G., and Rotello, V. M., *Tunable inhibition and denaturation of alpha-chymotrypsin with amino acid-functionalized gold nanoparticles*. J. Am. Chem. Soc., **2005**, *127*, 12873-12881.
91. Soto, C. M., et al., *Separation and recovery of intact gold-virus complex by agarose electrophoresis and electroelution: Application to the purification of cowpea mosaic virus and colloidal gold complex*. Electrophoresis, **2004**, *25*, 2901-2906.
92. Ogura, K., et al., *Solution structure of human acidic fibroblast growth factor and interaction with heparin-derived hexasaccharide*. J Biomol NMR, **1999**, *13*, 11-24.
93. Blaber, S. I., Culajay, J. F., Khurana, A., and Blaber, M., *Reversible thermal denaturation of human FGF-1 induced by low concentrations of guanidine hydrochloride*. Biophys J, **1999**, *77*, 470-477.

94. Canales, A., et al., *Solution NMR structure of a human FGF-1 monomer, activated by a hexasaccharide heparin-analogue*. FEBS J, **2006**, 273, 4716-4727.
95. Ostrovsky, O., et al., *Differential effects of heparin saccharides on the formation of specific fibroblast growth factor (FGF) and FGF receptor complexes*. J. Biol. Chem., **2002**, 277, 2444-2453.
96. Brych, S. R., Kim, J. W., Logan, T. M., and Blaber, M., *Accommodation of a highly symmetric core within a symmetric protein superfold*. Prot Sci, **2003**, 12, 2704-2718.
97. Brych, S. R., Blaber, S. I., Logan, T. M., and Blaber, M., *Structure and stability effects of mutations designed to increase the primary sequence symmetry within the core region of a beta-trefoil*. Prot Sci, **2001**, 10, 2587-2599.
98. Blaber, M., Disalvo, J., and Thomas, K. A., *X-ray crystal structure of human acidic fibroblast growth factor*. Biochemistry, **1996**, 35, 2086-2094.
99. Blaber, S. I., Culajay, J. F., Khurana, A., and Blaber, M., *Reversible thermal denaturation of human FGF-1 induced by low concentrations of guanidine hydrochloride*. Biophys J, **1999**, 77, 470-477.
100. Weare, W. W., Reed, S. M., Warner, M. G., and Hutchison, J. E., *Improved synthesis of small (d(CORE) approximate to 1.5 nm) phosphine-stabilized gold nanoparticles*. J Am Chem Soc, **2000**, 122, 12890-12891.
101. Sreerama, N. and Woody, R. W., *Estimation of protein secondary structure from circular dichroism spectra: comparison of CONTIN, SELCON, and CDSSTR methods with an expanded reference set*. Anal Biochem, **2000**, 287, 252-260.
102. Petroski, J., Chou, M. H., and Creutz, C., *Rapid phosphine exchange on 1.5-nm gold nanoparticles*. Inorg Chem, **2004**, 43, 1597-1599.
103. Brych, S. R., et al., *Symmetric primary and tertiary structure mutations within a symmetric superfold: A solution, not a constraint, to achieve a foldable polypeptide*. J Mol Biol, **2004**, 344, 769-780.
104. Aime, S., et al., *High sensitivity lanthanide(III) based probes for MR-medical imaging*. Coord Chem Rev, **2006**, 250, 1562-1579.
105. Bottrill, M., Nicholas, L. K., and Long, N. J., *Lanthanides in magnetic resonance imaging*. Chem Soc Rev, **2006**, 35, 557-571.
106. Bjornerud, A. and Johansson, L., *The utility of superparamagnetic contrast agents in MRI: theoretical consideration and applications in the cardiovascular system*. NMR Biomed, **2004**, 17, 465-477.

107. Parak, W. J., Pellegrino, T., and Plank, C., *Labelling of cells with quantum dots*. *Nanotechnol*, **2005**, *16*, R9-R25.
108. West, J. L. and Halas, N. J., *Engineered nanomaterials for biophotonics applications: Improving sensing, imaging, and therapeutics*. *Ann Rev Biomed Eng*, **2003**, *5*, 285-292.
109. Portney, N. G. and Ozkan, M., *Nano-oncology: drug delivery, imaging, and sensing*. *Anal Bioanal Chem*, **2006**, *384*, 620-630.
110. Manabe, N., et al., *Quantum dot as a drug tracer in vivo*. *IEEE Transactions on Nanobioscience*, **2006**, *5*, 263-267.
111. Conti, M., et al., *Anticancer drug delivery with nanoparticles*. *In Vivo*, **2006**, *20*, 697-701.
112. Medintz, I. L., Mattoussi, H., and Clapp, A. R., *Potential clinical applications of quantum dots*. *Int J Nanomed*, **2008**, *3*, 151-167.
113. Mulder, W. J. M., et al., *Molecular imaging of macrophages in atherosclerotic plaques using bimodal PEG-micelles*. *Magn Reson Med*, **2007**, *58*, 1164-1170.
114. Tan, W. B. and Zhang, Y., *Multifunctional quantum-dot-based magnetic chitosan nanobeads*. *Adv Mater*, **2005**, *17*, 2375-+.
115. Prinzen, L., et al., *Optical and magnetic resonance imaging of cell death and platelet activation using annexin a5-functionalized quantum dots*. *Nano Lett*, **2007**, *7*, 93-100.
116. Mulder, W. J., et al., *Quantum dots with a paramagnetic coating as a bimodal molecular imaging probe*. *Nano Lett*, **2006**, *6*, 1-6.
117. Tan, W. B. and Zhang, Y., *Multi-functional chitosan nanoparticles encapsulating quantum dots and Gd-DTPA as imaging probes for bio-applications*. *J Nanosci Nanotechnol*, **2007**, *7*, 2389-2393.
118. Santra, S., et al., *Rapid and effective labeling of brain tissue using TAT-conjugated CdS: Mn/ZnS quantum dots*. *Chem Comm*, **2005**, 3144-3146.
119. Jiang, L., et al., *Novel chitosan derivative nanoparticles enhance the immunogenicity of a DNA vaccine encoding hepatitis B virus core antigen in mice*. *J Gene Med*, **2007**, *9*, 253-264.
120. Xie, R., Battaglia, D., and Peng, X., *Colloidal InP nanocrystals as efficient emitters covering blue to near-infrared*. *J Am Chem Soc*, **2007**, *129*, 15432-+.

121. Bharali, D. J., Lucey, D. W., Jayakumar, H., Pudavar, H. E., and Prasad, P. N., *Folate-receptor-mediated delivery of InP quantum dots for bioimaging using confocal and two-photon microscopy*. J Am Chem Soc, **2005**, *127*, 11364-11371.
122. Flora, S. J. S., *Possible health hazards associated with the use of toxic metals in semiconductor industries*. J Occup Health, **2000**, *42*, 105-110.
123. Yamazaki, K., et al., *Long term pulmonary toxicity of indium arsenide and indium phosphide instilled intratracheally in hamsters*. J Occup Health, **2000**, *42*, 169-178.
124. Oda, K., *Toxicity of a low level of indium phosphide (InP) in rats after intratracheal instillation*. Ind Health, **1997**, *35*, 61-68.
125. Uemura, T., et al., *Effects of intratracheally administered indium phosphide on male Fischer 344 rats*. J Occup Health, **1997**, *39*, 205-210.
126. Omura, M., et al., *Changes in the testicular damage caused by indium arsenide and indium phosphide in hamsters during two years after intratracheal instillations*. J Occup Health, **2000**, *42*, 196-204.
127. Chan, W. H. and Shiao, N. H., *Cytotoxic effect of CdSe quantum dots on mouse embryonic development*. Acta Pharmacol Sin, **2008**, *29*, 259-266.
128. Choi, A. O., Brown, S. E., Szyf, M., and Maysinger, D., *Quantum dot-induced epigenetic and genotoxic changes in human breast cancer cells*. J Mol Med, **2008**, *86*, 291-302.
129. Bai, S.-S., et al., *Comparative study of genotoxicity in mice exposed to cadmium sulfide quantum dots and normal cadmium sulfide*. Asian Journal of Ecotoxicology, **2008**, *3*, 59-64.
130. Chang, E., Thekkek, N., Yu, W. W., Colvin, V. L., and Drezek, R., *Evaluation of quantum dot cytotoxicity based on intracellular uptake*. Small, **2006**, *2*, 1412-1417.
131. Chan, W. H., Shiao, N. H., and Lu, P. Z., *CdSe quantum dots induce apoptosis in human neuroblastoma cells via mitochondrial-dependent pathways and inhibition of survival signals*. Toxicol Lett, **2006**, *167*, 191-200.
132. Ballou, B., *Quantum dot surfaces for use in vivo and in vitro*. Curr Top Dev Biol, **2005**, *70*, 103-+.
133. Tsay, J. M. and Michalet, X., *New light on quantum dot cytotoxicity*. Chemistry & Biology, **2005**, *12*, 1159-1161.
134. Lynch, I. and Dawson, K. A., *Protein-nanoparticle interactions*. Nano Today, **2008**, *3*, 40-47.

135. Dobrovolskaia, M. A. and Mcneil, S. E., *Immunological properties of engineered nanomaterials*. Nat Nanotechnol, **2007**, 2, 469-478.
136. Choi, H. S., et al., *Renal clearance of quantum dots*. Nat Biotechnol, **2007**, 25, 1165-1170.
137. Kim, S., et al., *Near-infrared fluorescent type II quantum dots for sentinel lymph node mapping*. Nat Biotechnol, **2004**, 22, 93-97.
138. Zhu, X. F. and Lever, S. Z., *Formation kinetics and stability studies on the lanthanide complexes of 1,4,7,10-tetra-azacyclododecane-N,N',N'',N''' tetraacetic acid by capillary electrophoresis*. Electrophoresis, **2002**, 23, 1348-1356.
139. Aime, S., et al., *Paramagnetic lanthanide(III) complexes as pH-sensitive chemical exchange saturation transfer (CEST) contrast agents for MRI applications*. Magn Reson Med, **2002**, 47, 639-648.
140. Vander Elst, L., et al., *Dy-DTPA derivatives as relaxation agents for very high field MRI: the beneficial effect of slow water exchange on the transverse relaxivities*. Magn Reson Med, **2002**, 47, 1121-1130.
141. Vander Elst, L., et al., *Dy-complexes as high field T2 contrast agents: influence of water exchange rates*. Acad Radiol, **2002**, 9 Suppl 2, S297-299.
142. Gump, J. M. and Dowdy, S. F., *TAT transduction: the molecular mechanism and therapeutic prospects*. Trends Mol Med, **2007**, 13, 443-448.
143. Jones, A. T., *Gateways and tools for drug delivery: Endocytic pathways and the cellular dynamics of cell penetrating peptides*. Int. J. Pharm., **2008**, 354, 34-38.
144. Nakase, I., Takeuchi, T., Tanaka, G., and Futaki, S., *Methodological and cellular aspects that govern the internalization mechanisms of arginine-rich cell-penetrating peptides*. Adv Drug Deliv Rev, **2008**, 60, 598-607.
145. Gupta, B., Levchenko, T. S., and Torchilin, V. P., *Intracellular delivery of large molecules and small particles by cell-penetrating proteins and peptides*. Adv Drug Deliv Rev, **2005**, 57, 637-651.
146. Zhou, M. and Ghosh, I., *Quantum dots and peptides: A bright future together*. Biopolymers, **2007**, 88, 325-339.
147. Khalil, I. A., Kogure, K., Akita, H., and Harashima, H., *Uptake pathways and subsequent intracellular trafficking in nonviral gene delivery*. Pharmacol Rev, **2006**, 58, 32-45.

148. Niculescu-Duvaz, D., Heyes, J., and Springer, C. J., *Structure-activity relationship in cationic lipid mediated gene transfection*. *Curr Med Chem*, **2003**, *10*, 1233-1261.
149. Wiethoff, C. M. and Middaugh, C. R., *Barriers to nonviral gene delivery*. *J Pharm Sci*, **2003**, *92*, 203-217.
150. Friend, D. S., Papahadjopoulos, D., and Debs, R. J., *Endocytosis and intracellular processing accompanying transfection mediated by cationic liposomes*. *Biochim Biophys Acta, Biomembr*, **1996**, *1278*, 41-50.
151. Karmali, P. P. and Chaudhuri, A., *Cationic Liposomes as non-viral carriers of gene medicines: Resolved issues, open questions, and future promises*. *Med Res Rev*, **2007**, *27*, 696-722.
152. Lechardeur, D., Verkman, A. S., and Lukacs, G. L., *Intracellular routing of plasmid DNA during non-viral gene transfer*. *Adv Drug Deliv Rev*, **2005**, *57*, 755-767.
153. Grabarek, Z. and Gergely, J., *Zero-length crosslinking procedure with the use of active esters*. *Anal Biochem*, **1990**, *185*, 131-135.
154. Gerbec, J. A., Magana, D., Washington, A., and Strouse, G. F., *Microwave-enhanced reaction rates for nanoparticle synthesis*. *J Am Chem Soc*, **2005**, *127*, 15791-15800.
155. Shi, H. B., Xia, T., Nel, A. E., and Yeh, J. I., *Part II: coordinated biosensors - development of enhanced nanobiosensors for biological and medical applications*. *Nanomed*, **2007**, *2*, 599-614.
156. Sokolova, V. and Epple, M., *Inorganic nanoparticles as carriers of nucleic acids into cells*. *Angewandte Chemie-International Edition*, **2008**, *47*, 1382-1395.
157. Dobrovolskaia, M. A. and Mcneil, S. E., *Immunological properties of engineered nanomaterials*. *Nat Nanotechnol*, **2007**, *2*, 469-478.
158. Jiang, W., Kim, B. Y. S., Rutka, J. T., and Chan, W. C. W., *Nanoparticle-mediated cellular response is size-dependent*. *Nat Nanotechnol*, **2008**, *3*, 145-150.
159. Rosi, N. L., et al., *Oligonucleotide-modified gold nanoparticles for intracellular gene regulation*. *Science*, **2006**, *312*, 1027-1030.
160. Li, D., et al., *Glutathione-mediated release of functional plasmid DNA from positively charged quantum dots*. *Biomaterials*, **2008**, *29*, 2776-2782.

161. Derfus, A. M., Chen, A. A., Min, D. H., Ruoslahti, E., and Bhatia, S. N., *Targeted quantum dot conjugates for siRNA delivery*. *Bioconjug Chem*, **2007**, *18*, 1391-1396.
162. Chen, A. A., Derfus, A. M., Khetani, S. R., and Bhatia, S. N., *Quantum dots to monitor RNAi delivery and improve gene silencing*. *Nucleic Acids Res*, **2005**, *33*, e190.
163. Prow, T., et al., *Construction, gene delivery, and expression of DNA tethered nanoparticles*. *Molecular Vision*, **2006**, *12*, 606-615.
164. Jiang, W., Kim, B. Y., Rutka, J. T., and Chan, W. C., *Advances and challenges of nanotechnology-based drug delivery systems*. *Expert Opin Drug Deliv*, **2007**, *4*, 621-633.
165. Han, G., et al., *Light-regulated release of DNA and its delivery to nuclei by means of photolabile gold nanoparticles*. *Angewandte Chemie-International Edition*, **2006**, *45*, 3165-3169.
166. Han, G., Martin, C. T., and Rotello, V. M., *Stability of gold nanoparticle-bound DNA toward biological, physical, and chemical agents*. *Chemical Biology & Drug Design*, **2006**, *67*, 78-82.
167. Han, G., et al., *Controlled recovery of the transcription of nanoparticle-bound DNA by intracellular concentrations of glutathione*. *Bioconjugate Chemistry*, **2005**, *16*, 1356-1359.
168. Li, D., et al., *Glutathione-mediated release of functional plasmid DNA from positively charged quantum dots*. *Biomaterials*, **2008**, *29*, 2776-2782.
169. Jennings, T. L., Singh, M. P., and Strouse, G. F., *Fluorescent lifetime quenching near $d = 1.5$ nm gold nanoparticles: probing NSET validity*. *J. Am. Chem. Soc.*, **2006**, *128*, 5462-5467.
170. Yezhelyev, M. V., Qi, L. F., O'regan, R. M., Nie, S., and Gao, X. H., *Proton-sponge coated quantum dots for siRNA delivery and intracellular imaging*. *J Am Chem Soc*, **2008**, *130*, 9006-9012.
171. Bertrand, J. R., et al., *Comparison of antisense oligonucleotides and siRNAs in cell culture and in vivo*. *Biochem Biophys Res Commun*, **2002**, *296*, 1000-1004.
172. Jakobs, S., Subramaniam, V., Schonle, A., Jovin, T. M., and Hell, S. W., *EFGP and DsRed expressing cultures of Escherichia coli imaged by confocal, two-photon and fluorescence lifetime microscopy*. *FEBS Lett*, **2000**, *479*, 131-135.
173. Verkhusha, V. V., Akovbian, N. A., Efremenko, E. N., Varfolomeyev, S. D., and Vrzheschch, P. V., *Kinetic analysis of maturation and denaturation of DsRed, a coral-derived red fluorescent protein*. *Biochemistry (Mosc)*, **2001**, *66*, 1342-1351.

174. Lukacs, G. L., et al., *Size-dependent DNA mobility in cytoplasm and nucleus*. J Biol Chem, **2000**, 275, 1625-1629.
175. Giljohann, D. A., et al., *Oligonucleotide loading determines cellular uptake of DNA-modified gold nanoparticles*. Nano Letters, **2007**, 7, 3818-3821.

BIOGRAPHICAL SKETCH

Joshua Michael Kogot was born July 5, 1979 in Pittsburgh, PA to Sherry and Kenneth Kogot. Josh attended Burrell High School, Lower Burrell, PA from 1993 to 1997, graduating in the top 10% of his high school class. In the Fall of 1998 Josh enrolled at the University of Pittsburgh to pursue undergraduate work in Psychology and Chemistry. During his undergraduate career, Josh was employed as a summer intern in 2000 and 2001 at PPG Industries, Inc., Allison Park, PA, working as an analytical intern in 2000 and a polymer synthesis intern in 2001. Josh did undergraduate research in chemistry with Prof. Tara Meyer developing synthetic biomaterial polymers using repeating amino acid polymer subunits and psychology research with Dr. Jennifer Steel working on attributional style differences in sexually abused children, as well as 30 hours of clinical assistance with Dr. Steel in the liver disease clinic at the University of Pittsburgh Medical Center (UPMC).

Following graduation from the University of Pittsburgh in 2002, Josh worked as a high school chemistry instructor at Cushing Academy in Ashburnham, MA. This position included teaching general and honors chemistry at this private high school institution. In August 2003, Josh enrolled at Florida State University in the Department of Chemistry and Biochemistry in the biochemistry graduate program and joined the laboratory of Prof. Michael Blaber. In Prof. Blaber's group, Josh worked on isolating and identifying serine protease inhibitors for human kallikrein 6. In August 2005, Josh joined Prof. Geoff Strouse's research group and began working in the field of bio-nanotechnology under the guidance of both Prof. Strouse and Prof. Tim Logan.

During his work in the Strouse research group, Josh has worked at two research fronts, assembling His peptides and proteins on to gold nanoparticles, as well as assembling and delivering bio-nanomaterials for bimodal MRI contrast and gene therapeutics into mammalian cells. Josh has presented oral abstracts at local, regional, and national meetings: FAME (2006), SERMACS (2006), and MRS (2007). Josh is a current member of the American Association for the Advancement of Science (AAAS), the American Chemical Society (ACS), and the Materials Research Society (MRS).